2016

Characterization of molecule and particle transport through nanoscale conduits

BOSTON UNIVERSITY

COLLEGE OF ENGINEERING

Dissertation

CHARACTERIZATION OF MOLECULE AND PARTICLE TRANSPORT THROUGH NANOSCALE CONDUITS

by

MOHAMMAD AMIN ALIBAKHSHI

B.Sc., Iran University of Science and Technology, 2006
M.Sc., Iran University of Science and Technology, 2009

Submitted in partial fulfillment of the

requirements for the degree of

Doctor of Philosophy

2016

Approved by

First Reader

Chuanhua Duan, Ph.D.
Assistant Professor of Mechanical Engineering

Second Reader

Kamil L. Ekinci, Ph.D.
Professor of Mechanical Engineering

Third Reader

Joseph Scott Bunch, Ph.D.
Assistant Professor of Mechanical Engineering
Assistant Professor of Materials Science and Engineering
Assistant Professor of Physics

Fourth Reader

Irina V. Smolina, Ph.D.
Research Associate Professor of Biomedical Engineering

If you live properly, the *dreams will come* to *you.*

Randy Pausch

DEDICATION

To my wife, Maryam.

ACKNOWLEDGEMENTS

I would like to express my gratitude to my advisor Professor Chuanhua Duan for all he's done for me throughout the course of my PhD. What I've learnt, experienced, and was exposed to during my time at the NEFT lab opened up new horizons for me and has shaped my path to future. I'm thankful for his efforts to raise my research standards and improve my analytical thinking. I feel very lucky with him to have experienced the "research without borders" and latitude to explore multiple fields of research without being constrained to any boundaries. I'd like to extend my gratitude to Professor Robin O. Cleveland who advised my research for the first two years of my PhD, and selflessly supported me to find my best shot at research. I always appreciated how blessed one must be to sit in his classes, do research under his supervision, and most importantly learn the work ethics from him. I would like to deeply thank Professor Glynn Holt for his continued support during my PhD. I enjoyed sitting in his classes and also doing research with him and always found him a source of inspiration. I thank him for being on every important day of my PhD from my qualifying exam to holding the chair position in my PhD committee. I'm grateful to Professor Paul Barbone to whom I owe my career at BU. I was very privileged to have him as my academic advisor at my early time in the United States and discuss my thoughts and plans with him. I'm very thankful to Professor Kamil Ekinci for his special attentions and continued supports in advancing my research. I thank him for sharing his lab space with me for doing my experiments and also being on my PhD committee. I would like to thank Professor Scott Bunch for accepting my invitation to be on my committee and his technical comments and also Professor Smolina for her valuable

discussions of my experimental results on the nanopore sensing project as well as being on my PhD committee.

This work was not possible except by use of excellent services and facilities at Boston University Photonics center and in particular the Optoelectronic Processing Facility (OPF), the Precision Measurement Lab, the FTF lab (FIB/TEM), and also the BME Biointerface Technologies (BIT) facility, and the EPIC center at ME. In particular, I'd like to thank Mr. Paul Mak at OPF and Mr. Dave Campbell at EPIC for their helps throughout my years at BU.

I would like to thank members of the NEFT lab, Quan, Yinxiao, Andy and Binqi. We worked together, lived together, and learnt from each other. I'd like to thank my BU gang, Behzad, Ali, Sara, Sanaz, Vahideh, Samira and Vahid, and my old time friends Vahid Taghavi, Mohsen Maleki, and Mahdi Azarpeyvand without whom time stops. I've been and will forever be indebted to my parents whose prayers are my strength and their smiles my happiness. I thank my siblings and our growing family in Iran whom I dearly miss for supporting me from thousands of miles away with their energy. Finally, my biggest discovery during my graduate school was Maryam, my wife. I'm very lucky to have met her early in my PhD, and since then she has been a constant source of joy, happiness and comfort to me.

CHARACTERIZATION OF MOLECULE AND

PARTICLE TRANSPORT THROUGH NANOSCALE CONDUITS

MOHAMMAD AMIN ALIBAKHSHI

Boston University, College of Engineering, 2016

Major Professor: Chuanhua Duan, Ph.D., Assistant Professor of Mechanical Engineering

ABSTRACT

Nanofluidic devices have been of great interest due to their applications in variety of fields, including energy conversion and storage, water desalination, biological and chemical separations, and lab-on-a-chip devices. Although these applications cross the boundaries of many different disciplines, they all share the demand for understanding transport in nanoscale conduits. In this thesis, different elusive aspects of molecule and particle transport through nanofluidic conduits are investigated, including liquid and ion transport in nanochannels, diffusion- and reaction-governed enzyme transport in nanofluidic channels, and finally translocation of nanobeads through nanopores.

Liquid or solvent transport through nanoconfinements is an essential yet barely characterized component of any nanofluidic systems. In the first chapter, water transport through single hydrophilic nanochannels with heights down to 7 nm is experimentally investigated using a new measurement technique. This technique has been developed based on the capillary flow and a novel hybrid nanochannel design and is capable of characterizing flow in both single nanoconduits as well as nanoporous media. The presence of a 0.7 nm thick hydration layer on hydrophilic surfaces and its effect on increasing the hydraulic resistance of the nanochannels is verified. Next, ion transport in a new class of

nanofluidic rectifiers is theoretically and experimentally investigated. These so called nanofluidic diodes are nanochannels with asymmetric geometries which preferentially allow ion transport in one direction. A nondimensional number as a function of electrolyte concentration, nanochannel dimensions, and surface charge is derived that summarizes the rectification behavior of this system. In the fourth chapter, diffusion- and reaction-governed enzyme transport in nanofluidic channels is studied and the theoretical background necessary for understanding enzymatic activity in nanofluidic channels is presented. A simple analytical expression that describes different reaction kinetics is derived and confirmed against available experimental data of reaction of Trypsin with Poly-L-lysine. Finally, in the last chapter translocation of nanobeads through synthetic nanopores is experimentally investigated using resistive pulse sensing. The emphasis is placed on elucidating the effect of nanobead size on the translocation current and time. The key goals pursued in this study are multiplex detection of different nanobead sizes in a mixture of nanobeads as well as determining the concentration of each component. This problem other than its fundamental significance paves the way for developing new biosensing mechanisms for detection of biomolecules. This thesis further explores the molecule and particle transport in nanoscale conduits and serves for better characterization and development of nanofluidic devices for various applications.

Table of Contents

LIST OF TABLES

LIST OF FIGURES

CHAPTER 1: Introduction

Nanofluidics can be defined as the study and application of fluids/fluid transport under nanoscale confinement or around nanosized objects (Eijkel and Van Den Berg 2005; Schoch *et al.* 2008). Abundant examples of nanofluidic systems occur in nature at different size scales. At the molecular scale, all the biological organisms on their primary cellular level function in a nanofluidic environment regulated by infinitesimal ion channels. Excellent body filtration system of the kidney, lotus effect, i.e., self-cleaning exhibited by the leaves of the lotus flower and engineered superhydrophobic beetle wings are some nanofluidic related phenomena happening at different size scales in nature (Eijkel and Van Den Berg 2005). In the past two decades, however, the micro and nanofabrication and characterization techniques has allowed for capturing of nanofluidic phenomena and their application in variety of fields (Betancourt and Brannon-Peppas 2006). Nanofluidics not only has advanced different branches of Physics and Chemistry such as Electrokinetics, Colloids, Polymers, Separation science, and Tribology, but also has shown promise for advancement of Biology, Genetics, Physiology and Biophysics through single molecule study, determination of the DNA base sequences, study of ion channels, etc (Abgrall and Nguyen 2008; Bocquet and Charlaix 2010; Duan and Majumdar 2010; Edel and De Mello 2009; Eijkel and Van Den Berg 2005; Napoli *et al.* 2010; Schoch *et al.* 2008; Sparreboom *et al.* 2009). Nanofluidics phenomena occur in a regime where multiple physical length scales and phenomena become important, and hence it exhibits distinct behaviors that are not observed at larger scales. These length scales range from the size of small atoms to large biomolecules, slip length of water, the Debye screening length, and the persistence

length of a polymer, among others (Bocquet and Charlaix 2010). Moreover, at this scale minuscule surface charge density, van der Waals force, or solvation force, etc, can dictate the behavior of the system (Schoch *et al.* 2008) which provide us with the opportunity to address some of the major human concerns ranging from energy (Duan and Majumdar 2010; Sparreboom *et al.* 2009), to clean water (Lee *et al.* 2011) and medical diagnosis (Lee *et al.* 2010).

One of the most important concepts that has to be addressed about any nanoscale confined liquids, and probably the major way to harness potentials of such nanofluidic systems is through the study of transport phenomena (Schoch *et al.* 2008). Transport in the nanoconfined space is different from its micro and macroscopic counterparts due to dominance of the surface forces, as well as physical and chemical interactions of the species with the boundaries. Dominance of the surface forces is caused by large surface area to volume ratio of the nanofluidic system. There are two major forces acting in the nanometer range, namely, electrostatic forces and the van der Waals forces (Eijkel and Van Den Berg 2005; Napoli *et al.* 2010). Electrostatic forces act as far as the electrical double layer extends, which is typically from 1 nm to 100 nm, depending on the electrolyte concentration. van der Waals forces on the other hand predominantly act at distances smaller than 2 nm. Confining a fluid at these scales enables us to take advantage of unique transport properties at this regime for fabrication of sensitive biosensors, desalination of water, and conversion of energy. In addition to these forces, transport in a nanoconfined space can be subject to physical and chemical interactions with the surrounding boundaries. For example, nanoscale confinement can give rise to a non-Fickian diffusion regime with

altered diffusion coefficient (Cosentino *et al.* 2005). Furthermore, association of some chemical reactions with the transport in a confined space can alter both the kinetics of the reaction and also transport of the species of interest, and provides challenges and opportunities for their exploitation. Label-free electrical detection of biomolecule binding reaction and investigation of the diffusion kinetics of biomolecules in a confined state are only two applications involving physical and chemical interaction in precisely manufactured nanochannels.

Despite the extensive efforts on understanding transport phenomena and their utilization in the past decade, still "*there's plenty of room at the bottom*". For example, liquid transport in nanoscale conduits has remained relatively unexplored and there's no universal method for characterization of liquid transport in the nanochannels/tubes. Moreover, realizing potentials of the Nanofluidics for development of sensitive biosensors demands further research and exploration. Therefore, this thesis aims at theoretical and experimental examination of some of the fundamental aspects of the transport in the nanoconfined space with applications in biosensing. This thesis discusses different aspects of solutes and solvent transports through nanoscale conduits with focus on (*i*) transport of liquid in 2D nanochannels, (*ii*) transport of ions in 2D nanochannels, (*iii*) reaction-combined transport of enzymes in 2D nanochannels, and (*iv*) transport particles through nanopores. Each of these topics are presented in one chapter, starting with an introduction on significance and background of the work.

In the second chapter, well-defined 2D nanochannels are exploited to characterize liquid transport at the nanoscale. A new measurement method is proposed for liquid transport

characterization in single nanochannel/nanotubes based on capillary flow and a novel hybrid channel design. Change in flow condition compared to the results predicted by bulk hydrodynamic and the Navier-Stokes equation has been characterized by successful application of this method to hydrophilic silica channels with heights down to 7 nm. Chapter 3 theoretically and experimentally explores a new method for control of ionic current in nanofluidic system and development of a rectifier analogous to diodes in electrical circuits. The ionic rectifier is an asymmetric 2D nanochannels with rectangular cross section and a stepped structure consisting of a shallow and a deep side. Control of height and length of each side enables us to obtain optimum rectification at each ionic strength. A nondimensional concentration is presented as a function of nanochannel dimensions, surface charge and the electrolyte concentration that summarizes the rectification behavior of such geometries. Our method of fabrication and control of nanofluidic diode does not require modification of the surface charge and facilitates the integration with lab-on-a-chip fluidic circuits. Chapter 4 opens a discussion about theoretical background necessary for development of a fast-response, label-free enzyme sensors based on nanochannels. In this section, combined diffusion-reaction problem is solved in 2D nanochannels which simultaneously serve as the reaction container and the signal transducer. Here, enzymes diffuse into the nanochannel and react with the long polypeptide chains already immobilized on the walls of the nanochannel. Various reaction kinetics, enzyme diffusion and non-specific adsorption have been considered and through a 1D numerical simulation, two types of reaction fronts which progress linearly with time are identified. Simulations are validated by experimental results of the trypsin-polylysine

reaction in nanochannels and a good agreement is observed. Finally in chapter 5, resistive pulse sensing of single nanobeads in synthetic nanopores is presented. In this chapter, translocation of two different size of beads in low aspect ratio silicon nitride nanopores is studied. Here we aim at differentiating translocation signals of the two beads and measuring the nanobead concentration based on beads' capture rate. Our results demonstrated that signals of two different bead sizes can be reliably separated based on their translocation current. Accurate measurement of the concentration, however, requires precise control over the pore's surface charge. In addition, this study sheds light on some fundamental aspect of translocation through low aspect ratio pores. Results of this problem can be applied toward developing new biosensing mechanisms.

CHAPTER 2: Accurate Measurement of Liquid Transport through Nanoscale Conduits

Nanoscale liquid transport governs the behaviour of a wide range of nanofluidic systems, yet remains poorly characterized and understood due to the enormous hydraulic resistance associated with the nanoconfinement and the resulting minuscule flow rates in such systems. To overcome this problem, here we present a new measurement technique based on capillary flow and a novel hybrid nanochannel design and use it to measure water transport through single 2-D hydrophilic silica nanochannels with heights down to 7 nm. Our results show that silica nanochannels exhibit increased mass flow resistance compared to the classical hydrodynamics prediction. This difference increases with decreasing channel height and reaches 45% in the case of 7 nm nanochannels. This resistance increase is attributed to the formation of a 7-angstrom-thick stagnant hydration layer on the hydrophilic surfaces. By avoiding use of any pressure and flow sensors or any theoretical estimations the hybrid nanochannel scheme enables facile and precise flow measurement through single nanochannels, nanotubes, or nanoporous media and opens the prospect for accurate characterization of both hydrophilic and hydrophobic nanofluidic systems.

2.1 Introduction

Understanding liquid transport through nanoscale confinements is critical in a variety of practical applications, including energy conversion/storage (Ghasemi *et al.* 2014; Park and Jung 2014), water desalination (Lee *et al.* 2011; Park and Jung 2014), phase-change

thermal management (Plawsky *et al.* 2014), biological and chemical separations (Han and Craighead 2000), and lab-on-a chip devices (Kovarik and Jacobson 2009). Although it has been argued that the continuum assumption and classical hydrodynamics are capable of describing liquid transport at the nanoscale (Bocquet and Charlaix 2010; Park and Jung 2014; Thomas and McGaughey 2008; Travis and Gubbins 2000), the differences between nanoscale and micro/macroscale liquid transport, in terms of confined liquid properties (Becker and Mugele 2003; Gao *et al.* 2007; Goertz *et al.* 2007; Leng and Cummings 2005; Mante *et al.* 2014; Ortiz-Young *et al.* 2013; Qin *et al.* 2011; Raviv *et al.* 2001; Sendner *et al.* 2009; Thomas and McGaughey 2008), flow boundary conditions (slip/no slip) (Ho *et al.* 2011; Holt *et al.* 2006; Lee *et al.* 2012; Majumder *et al.* 2005; Qin *et al.* 2011; Thomas and McGaughey 2008; Whitby *et al.* 2008), secondary flows (Mortensen and Kristensen 2008; Phan *et al.* 2009; Wang *et al.* 2010), etc, still remain elusive. In fact, a wide range of slip length and confined liquid properties with up to several orders of magnitude discrepancies between different sources have been reported, indicating that nanoscale liquid transport has remained poorly characterized and novel accurate measurement techniques for this purpose are desired. The major challenge in performing precise flow measurement in nanoscale conduits is the associated huge hydraulic resistances which result in ultra-small flow rates. For example, based on classical hydrodynamics, only $\sim 0.25\ \mathrm{al/s}$ water flows through a hydrophilic tube 100 μm long and 10 nm in diameter, when one atmosphere pressure is applied. The most common method to bypass this challenge is to measure liquid transport in membranes consisting of numerous similar nanoscale conduits (Holt *et al.* 2006; Lee *et al.* 2012; Majumder *et al.* 2005; Whitby *et al.*

2008). However, analysis and verification of the data from this method is complicated by the fact that the measured flow rate constitutes an average over a large unknown number of conduits with a range of diameters and lengths. There are also concerns about possible leakage due to membrane defects and/or leakage at the membrane's edges (Joshi *et al.* 2014). Moreover, it may not be possible to create membrane structures for certain nanoscale conduits with specific geometry and surface properties, e.g. 2-D planar nanochannels that are widely used in lab-on-a-chip devices. On the other hand, capillary flow measurement is the major method used for characterizing fluid flow in individual nanoscale conduits by tracking the location of a moving meniscus as a function of time (Chauvet *et al.* 2012; Hamblin *et al.* 2011; Han *et al.* 2006; Haneveld *et al.* 2008; Oh *et al.* 2010; Qin *et al.* 2011; Sobolev *et al.* 2000; Tas *et al.* 2004; Thamdrup *et al.* 2007; van Delft *et al.* 2007). However, in this method—which is mainly applicable to hydrophilic channels—the driving pressure in the nano-conduits is not experimentally measured, but calculated based on classical theories (Chauvet *et al.* 2012; Hamblin *et al.* 2011; Han *et al.* 2006; Haneveld *et al.* 2008; Oh *et al.* 2010; Sobolev *et al.* 2000; Tas *et al.* 2004; Thamdrup *et al.* 2007; van Delft *et al.* 2007) with bulk liquid properties or molecular simulations (Qin *et al.* 2011), which can be quite different from the actual values, resulting in inaccurate calculation of the actual hydraulic resistance. Given the limitations of the current measurement techniques, it is thus necessary to develop a technique for liquid flow measurement in single nano-conduits (Li *et al.* 2012; Sinha *et al.* 2007) which can be applied to both hydrophobic and hydrophilic conduits without using any theoretical estimations. Herein, we report such a technique based on capillary flow and a novel hybrid

nanochannel design and use it to characterize water transport in single silica nanochannels with heights down to 7 nm.

2.2 Hybrid nanochannel scheme

The hybrid nanochannel design consists of a test channel (the channel under investigation) seamlessly connected to a reference channel with a different but known mass flow resistance (Figure 2.1). In a typical experiment, two capillary flow measurements are conducted in the hybrid channel, one starting from the test channel side and the other starting from the reference channel side. However, the meniscus location is only recorded in one of the two channels, which we call it the "observation channel". Without loss of generality, let's assume the observation channel is the reference channel. In this case, the first capillary filling process starts from the reference channel side (Figure 2.1.b). The location of the meniscus in the reference channel $X(t)$ is recorded and is expected to be governed by the Washburn equation. Take a rectangular-shaped channel, with width and height of w and h. If the width of the channel is much larger than its height ($w \gg h$), with the neglect of inertia term the momentum equation governing the incompressible flow in this channel can be written as (Figure 2.1.b):

$$\mu \frac{d^2u}{dz^2} = \frac{dp}{dX} \tag{2.1}$$

with μ being the fluid viscosity and z the direction along the channel height. The slip boundary condition for the lower and upper walls of the channel ($z = 0, h$) can be expressed as:

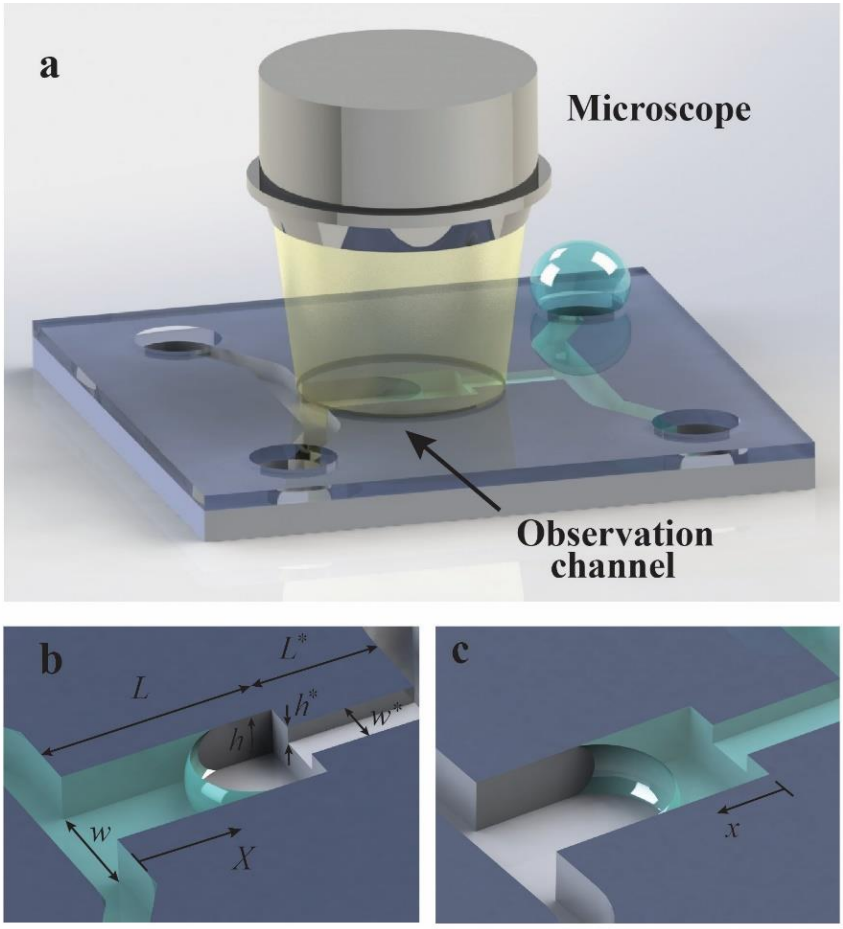

Figure 2.1: (**a**) Channel under investigation is seamlessly connected to a reference channel of known hydraulic resistance, and the data is collected from the observation channel which can be either of the channels. (**b**) The Observation channel is first characterized by a capillary flow experiment yielding the value of A. (**c**) Ratio of the mass flow resistance between the two channels can be found by introducing liquid from the other side, and tracking the meniscus again in the observation channel.

$$\frac{u}{l_s} = \pm \frac{du}{dz}\Big|_{z=0,h} \tag{2.2}$$

in which l_s is the slip length. Accordingly, the velocity profile and the mass flow rate can be found as:

$$u = \frac{1}{2\mu}\frac{dp}{dX}(z^2 - hz - hl_s) \tag{2.3}$$

$$\dot{m} = \rho w \int_0^h u dz = -\frac{\rho w h^3}{12\,\mu}\frac{dp}{dX}\left(1 + 6\frac{l_s}{h}\right) \tag{2.4}$$

wherein ρ is the fluid density. The slip boundary condition covers the "no slip" boundary condition if one simply sets $l_s = 0$. Now, defining hydraulic resistance as $r = \frac{\Delta P}{\dot{m}}$, the hydraulic resistance of a channel per unit length would be obtained as:

$$R = \frac{12\,\mu}{\rho w h^3\left(1 + 6\frac{l_s}{h}\right)} \tag{2.5}$$

Combining equations (2.4) and (2.5) yields a relation for liquid meniscus location in the channel (X) as a function of time, when a pressure difference of ΔP is applied:

$$\rho w h \frac{dX}{dt} = \frac{\Delta P}{RX}$$

$$X^2 = 2At, \quad A = \frac{1}{\rho w h}\frac{\Delta P}{R} \tag{2.6}$$

If the pressure difference is replaced by the capillary pressure, $\Delta P = 2\sigma\cos(\theta)/h$, with σ being the surface tension and θ the contact angle, and assuming $l_s = 0$, the following equation, known as the Washburn equation, governing the location of a meniscus as a function of time in capillary fillings can be derived:

$$X = \sqrt{\frac{\sigma h \cos(\theta)}{3\,\mu}t} \tag{2.7}$$

After the first measurement, liquid is removed from the nanochannel and is introduced from the test channel side for the second measurement (Figure 2.1.c). The location of the

meniscus in the reference channel during the second capillary filling process $x(t)$ is then recorded. (Figure 2.1.b, 2.1.c) One can use the resistance concept to derive a governing equation describing capillary flow in a hybrid channel. If R^* is the resistance per unit length of the test channel with length L^*, and the meniscus is at location x in the reference channel, then mass flow rate in the hybrid channel can be written as:

$$\dot{m} = \rho w h \frac{dx}{dt} = \frac{\Delta P}{Rx + R^* L^*}$$

$$(Rx + R^* L^*)dx = \frac{\Delta P}{\rho w h} dt$$

$$\frac{1}{2}x^2 + \frac{R^*}{R} L^* x = \frac{1}{\rho w h} \frac{\Delta P}{R} t$$

Defining $\eta = \frac{R}{R^*}$, this equation can be written as:

$$\frac{1}{2}x^2 + \frac{L^*}{\eta} x = At \tag{2.8}$$

$$\eta = \frac{R}{R^*} = \frac{\rho^*}{\rho} \frac{\mu}{\mu^*} \frac{w^*}{w} \frac{h^{*3}}{h^3} \frac{\left(1 + 6\frac{l_s^*}{h^*}\right)}{\left(1 + 6\frac{l_s}{h}\right)}$$

In this equation, $t = 0$ corresponds to the time when the meniscus enters the reference channel ($x = 0$, Figure 2.1.c), η is the ratio of the mass flow resistance between the reference channel and the test channel per unit length and the starred variables belong to the test channel, with L^* being the length of the test channel. By fitting experimental data sets $X(t)$ and $x(t)$ with equations (2.6) and (2.8), capillary flow constant, A, in the observation channel and the mass flow resistance ratio, η, can be extracted. Consequently, resistance of the test channel can be quantified if the resistance of the reference channel is

known. It is worth noting that the test channel can be an individual channel, tube or even nanoporous media, and no matter if it is hydrophobic or hydrophilic, as long as either of test or reference channels allows for spontaneous liquid filling, this technique can be applied.

2.3 Error Analysis

The hybrid channel scheme can be used to measure a wide range of η's and thus a wide range of nanochannel resistance, with a relatively small error. The full derivation of the error analysis is presented in Appendix 1. Our linear regression based error analysis indicates that the experimental error associated with η ($E = \delta\eta/\eta$) reaches a plateau at small values of η determined by $E \propto \sqrt{A\tau}\ \delta x/L^2$ with δx and τ being the spatial resolution and the frame interval (Figure 2.2). In this range, error is very small and is not a function of η and L^*. At large values of η, however, error is a linear function of η ($E \propto \sqrt{A\tau}\delta x\eta/LL^*$), and a larger L^* along with a smaller capillary flow constant A can be employed to reduce the error in this range. In fact, this method can be best utilized if η is smaller than 1, and thus to study test channels with a very small resistance compared with the reference channel (yielding large values of η), one should possibly choose the test channel as the observation channel such that $1/\eta$ would be measured instead of η. This resolves the theoretical limit for accurate characterization of the flow and allows for measurement of very high resistance ratios with a small error. Nevertheless, by designing a long test channel and choosing a high frame rate, the hybrid nanochannel scheme is able to detect very large values of η ($> 10^4$) with a small error (Figure 2.2) adequate for the

study of enhanced liquid transport in carbon nanotubes and graphene nanochannels where a wide range of flow enhancements have been reported (Holt *et al.* 2006; Majumder *et al.* 2005; Qin *et al.* 2011; Thomas and McGaughey 2008; Whitby *et al.* 2008).

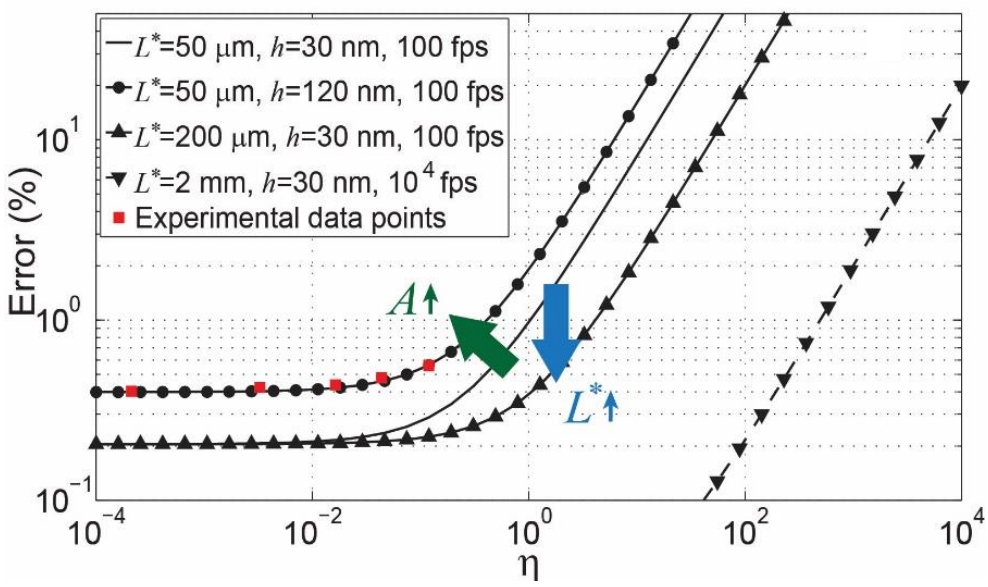

Figure 2.2: Error associated with η. Assuming $\delta x = \delta X = 1\,\mu m$, and the observation channel is $350\,\mu m$ long, error for different values of A, L^*, and frame rates has been evaluated. (The square markers are the experimental data points)

2.4 Design, fabrication, and measurement

In the present investigation, the proposed characterization scheme is utilized to study water transport in hydrophilic silica nanochannels with heights ranging from 7 nm to 59 nm. In our design, nanochannels with the same widths but larger heights (~110–120 nm) serve as the reference channels. This choice of the reference channel height serves several purposes: First, this depth of water in the reference channel can be very easily detected with an optical microscope. Second, this choice of height helps to avoid entrapment of air and creation of bubbles in the reference channel (Chauvet *et al.* 2012; Han *et al.* 2006; Thamdrup *et al.*

2007; van Delft *et al.* 2007). Finally, with this choice of heights, η would be less than 1 and the experimental error would be very small (Figure 2.2). The hybrid silica nanochannel devices are fabricated using the classic etching and bonding scheme, while the seamless connection between the test and the reference channels are achieved using double-layer photoresist coating (Figure 2.3.a). Briefly, five sets of stepped nanochannels were fabricated with $\frac{h^*}{h} = \frac{7\pm0.5\ nm}{117.5\ \pm0.5\ nm}, \frac{16.2\pm0.4\ nm}{109.5\ \pm1nm}, \frac{28\pm0.5\ nm}{110.5\pm2\ nm}, \frac{38\pm0.5\ nm}{108\pm1\ nm}$, and $\frac{59\pm0.5\ nm}{121\pm1\ nm}$. Uniformity of the RIE etching throughout the entire silicon wafers allowed us to fabricate many chips of almost exact heights in each trial. The width of both test and reference channels is 3 μm, the reference channel's length is $L = 550\ \mu m$, and the test channel's length is $L^* = 550\ \mu m$, except for the 7 nm channel, which is $L^* = 7.5\ \mu m$. Long test channels with very small heights impose a very large resistance before the reference channel such that the meniscus may stop at the step and the corner flows become the dominant mode of filling (Dong and Chatzis 1995; Ransohoff and Radke 1988; Weislogel and Lichter 1998). For this reason the 7 nm test channel is chosen to be 7.5 μm long to allow easy flow of water. After etching the nanochannels, two microchannels each 6 mm long, 1 mm wide and 40 μm deep were etched using DRIE on both terminals of the nanochannels to carry water from the reservoirs, and the four reservoirs which are 2 mm by 2 mm through holes were later etched using DRIE (Figure 2.3.b). Finally, 300 nm thick dry thermal oxide layer was grown on the silicon chips, and the chips were cleaned with Piranha (3:1, H_2SO_4:H_2O_2) and bonded to Borosilicate glass by using anodic bonding at 400 ^oC and 350 Volts. Microscope images of a bonded hybrid nanochannel device is shown in Figure 2.3.b. The test channels, reference channels, location of the steps, as well as

connection of the microchannel to the nanochannels for this device (16.2 nm/109.5 nm) is shown in Figure 2.3.c. Heights of the test and the reference nanochannels are measured using AFM before anodic bonding. Figures 2.3.d thru 2.3.g show the 3D AFM images of four representative hybrid nanochannels used for the experiments with h^*=7, 16, 38, and 59 nm.

All the experiments were performed with DI water (electrical resistivity>18 $M\Omega.cm$) at 22 ± 1 ˚C (pH=7), before each experiment oxygen plasma (500 Watts, 500 SCCM O_2) was applied to the chips for 15 minutes to make the surfaces super hydrophilic and prevent formation of bubbles in the nanochannels. The water meniscus in nanochannels were tracked by an Olympus inverted microscope model IX81 equipped with a monochromatic HAMAMATSU CMOS FLASH 4.0 C11440 camera recording at up to 900 fps (or at lower rates when not necessary). Position of the meniscus as a function of time was extracted from the recorded frames using a MATLAB image processing code.

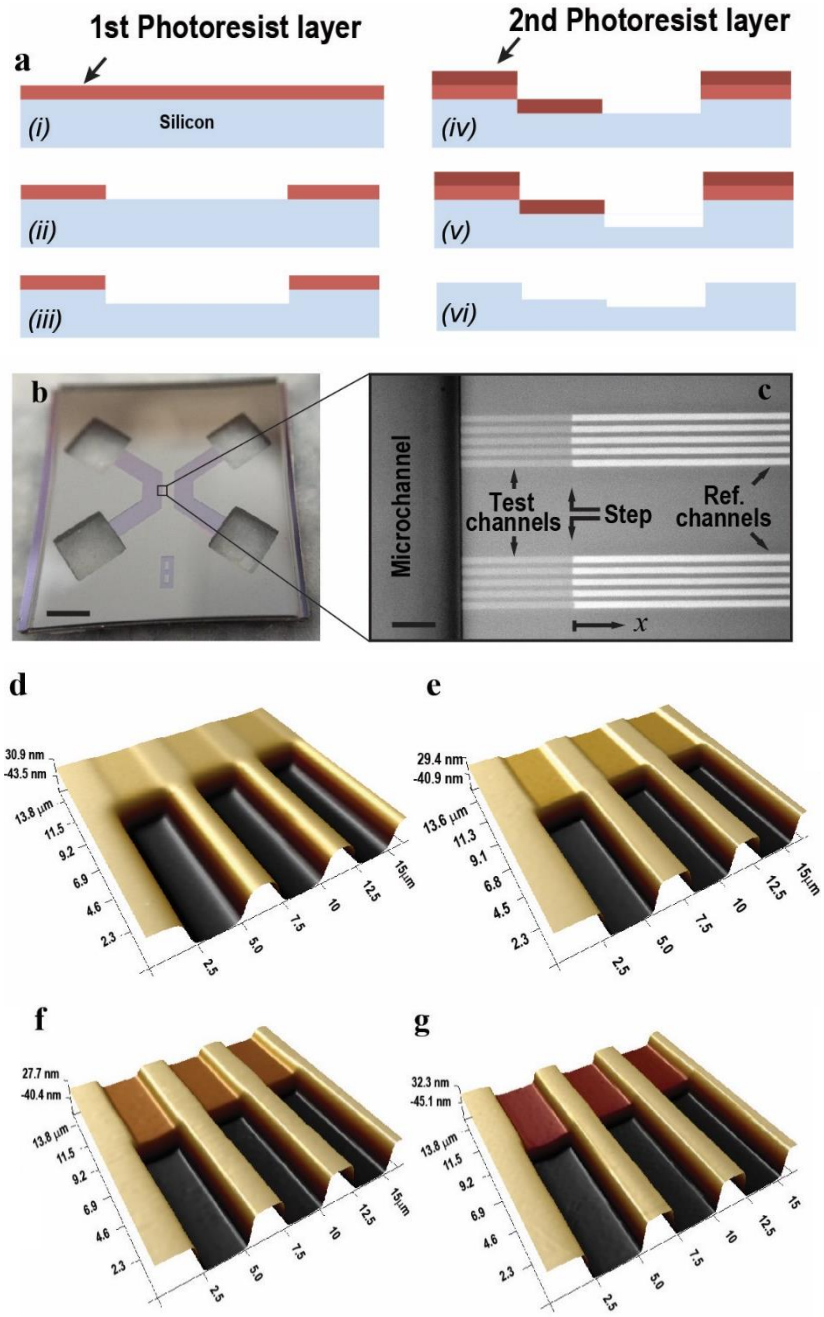

Figure 2.3: (**a**) Fabrication procedure of the hybrid channels, using double layer photoresist coating and RIE etching. (**b**,**c**) structure of a chip used for experiments; water is carried from one of the reservoirs to the nanochannels through a microchannel. Nanochannels 600 μm long are located between two microchannels, each consisting of a shallow side and a deep side creating a step in the nanochannels. (scale bars of **b** and **c** are 2 mm and 20 μm) (**d-g**) Representative AFM images of four hybrid channels used for the experiments with $\frac{h^*}{h}$ = 7 nm/117.5 nm, 16.2 nm/109.5 nm, 38 nm/108 nm, and 59 nm/121 nm.

2.5 Results and discussion

2.5.1 Obtaining the correction factor □

The capillary flow constant, A, is found by introducing water from the reference channel side, tracking the location of meniscus as a function of time and curve fitting to the experimental data (Figures 2.4.a and 2.4.b). This quantity is known to be smaller than theoretical predictions for the nanochannels and different reasons have been proposed to explain the discrepancies between theory and experiments. Increase in water viscosity (Mortensen and Kristensen 2008; Phan *et al.* 2009; Tas *et al.* 2004; Wang *et al.* 2010), surface roughness and the dynamic contact angle (Hamblin *et al.* 2011; Sobolev *et al.* 2000), and presence of pinned bubbles or entrapment of gas inside the nanofluidic channels (Chauvet *et al.* 2012; Han *et al.* 2006; Thamdrup *et al.* 2007; van Delft *et al.* 2007) are among major phenomena that have been proposed to explain it.

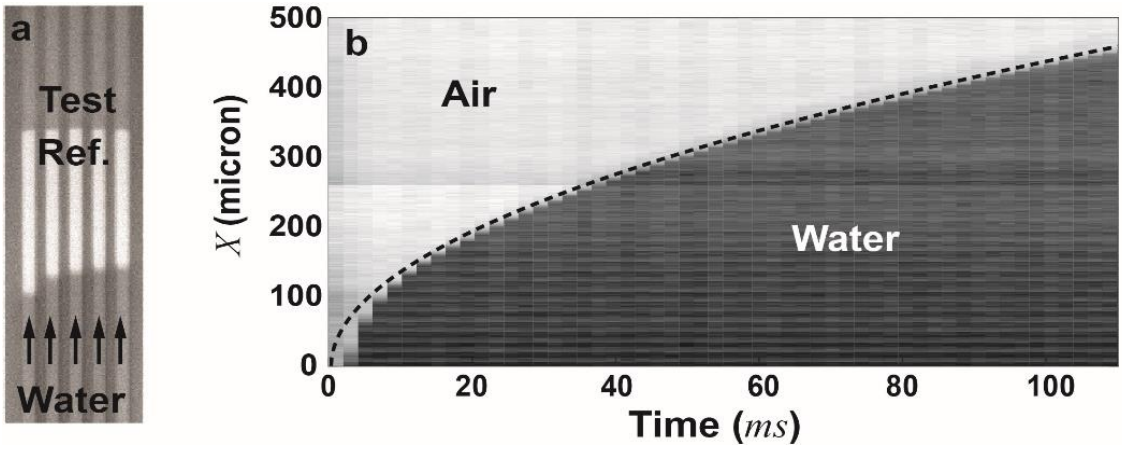

Figure 2.4: (**a**) Microscope image of capillary filling of the reference channel starting from the reference channel side. Image processing of the recorded frames allows for extraction of $X - t$ curve of the meniscus. (**b**) Meniscus location in the reference channel recorded at 500 fps, showing a clear square root time dependence.

Apparent increase in water viscosity in nanofluidic channels, known as the electroviscosity, is a phenomenon that occurs due to creation of an electro-osmosis counter flow resisting the pressure-driven flow. Dynamic contact angle is another factor that can partly explain the deviation of experiments from theory, and accounts for the fact that an advancing meniscus does not keep a constant contact angle with the walls throughout filling process, and the real average value is larger than the static contact angle. Moreover, entrapment of gas in nanofluidic channels can alter the hydraulic resistance of the channel and causes the meniscus to move slower than theory. Such deviations from theory are usually presented in the form of a correction factor defined as $C = A_{theory}/A_{actual}$ as a function of nanochannels height. In order to find the A_{actual} a curve fitting to the experimental data based on Washburn equation needs to be done. A close look at the early phase of capillary filling in the reference channel reveals that the speed of meniscus is much faster than predicted by Washburn equation (Figure 2.5.a). Addressing this phase in capillary filling which seems to be mainly ruled by the corner flows and film flows is out of scope of this work; nevertheless, to obtain A_{actual}one has to consider the entrance effect and hence in this work only data of menisci located in the range of 250 μm to 500 μm from the entrance of the reference channels were used to fit the theoretical curves. It's worthwhile mentioning that this phenomenon was a lot less pronounced in capillary filling of shallower reference channels with $h = 50$ nm. To find the correction factor C, A_{actual} is compared with the theoretical A estimated by assuming $\Delta P = 2\sigma \cos(\theta)\left(\frac{1}{h} + \frac{1}{w}\right)$, $\theta = 0$, $\mu = 1$ mPa.s, σ=0.07 N/m, $w = 3\ \mu m$, along with the height of the reference channel for each channel set. As already discussed, A has contributions from both resistance term as well as the

pressure term. However, given the relatively large height of the reference channels and also because the electroviscosity effect cannot be more than a few percent (Mortensen and Kristensen 2008; Phan *et al.* 2009; Wang *et al.* 2010), negligible deviation of the hydraulic resistance from theory is expected for the reference channels and the correction factor C can be mainly attributed to the capillary pressure. In fact, surface quality of the nanochannels, i.e., roughness and hydrophilicity, can be the major role players and in particular hydrophilicity of the surfaces can be slightly different from chip to chip and also may vary depending on the preparation of the chips, yielding different contact angles. In fact distorted menisci and/or menisci with different contact angles have been observed in our experiments reflecting the interplay between the capillary force and the viscous forces (Figure 2.5.c). The contact angles shown in Figure 2.5.c are of course the in-plane contact angles (the top view of the channel), and the capillary pressure by formation of a curved meniscus in this plane cannot be more than ~3% of the total capillary pressure ($\frac{h}{w}\sim 3\%$); however, one can expect the same behavior in the meniscus shape to be observed along the channel height which is the dominating term. In this work, for the reference channels of similar height (110 nm to 120 nm), the measured correction factors C ranged from 1 to 1.35 with the average of $C = 1.22$. Moreover, we observed that this correction factor increases over time, which is mainly attributed to deterioration of surface properties and creation of hydrophobic sites along the channels.

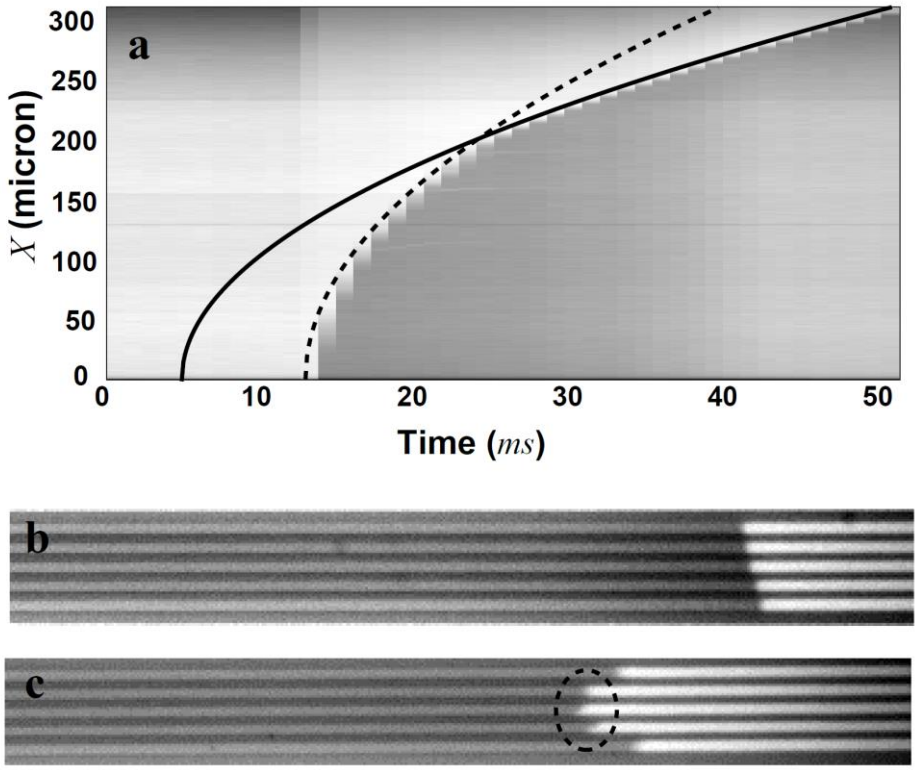

Figure 2.5: (**a**) Location of meniscus versus time in a reference channel of height h=109.5 nm. The dashed line is the best fit to the fast initial phase of filling, obtained based on the Washburn equation with the correction factor of C =0.7. The solid line is the fit to the second phase with a correction factor of C =1.2. (data recorded at 900 frames per second) (**b**,**c**) Shape of meniscus during filling can change and while in times they look normal as in **b**, they can get distorted and give rise to a reduced capillary pressure. (**c**)

2.5.2 Obtaining the resistance increase factor α

After measuring the capillary flow constant, in the second experiment water is introduced from the test channel side. (Figures 2.6.a and 2.6.b, h^*=16.2 nm) It was observed that meniscus moves with a constant speed (linear dependence of x on t, instead of $\sqrt{t}$), consistent with equation (2.8) in case of $\eta \ll 1$:

$$x = \frac{A\eta}{L^*}t \qquad (2.9)$$

In fact, when $\eta \ll 1$, most of the resistance originates from the test channels and as a result, ΔP at the meniscus has to overcome an almost constant resistance throughout the entire filling process and thus travels with a constant velocity. This velocity is much slower than the first experiment which allows for easy measurement of the $x - t$ data at low frame rates. Representative measured $x - t$ curves for each of the five tested hybrid nanochannel sets along with the experimental η's are presented in Figure 2.7.a. Our experimental results measure η's spanning over three orders of magnitude with a small error predicted by our error analysis (Figures 2.7.a and 2.2).

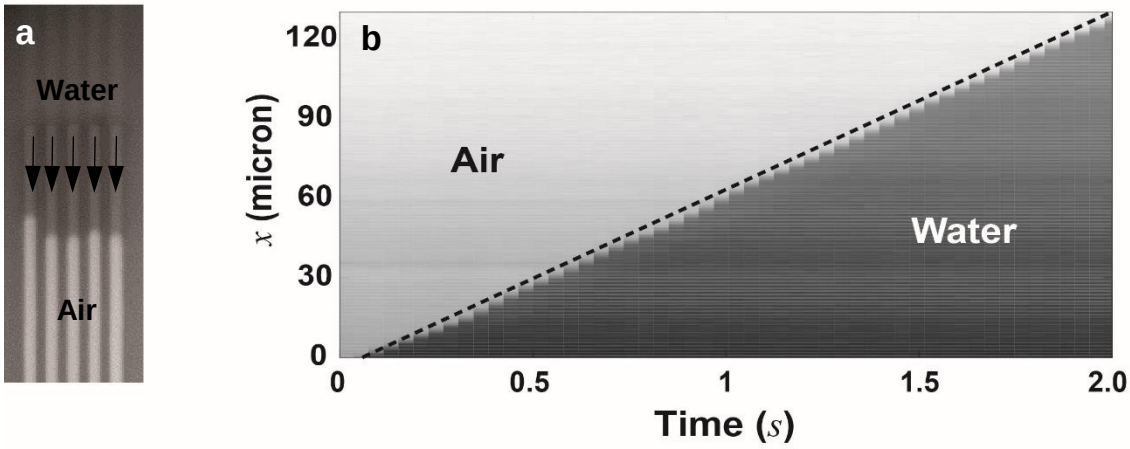

Figure 2.6: (**a**) Microscope image of capillary filling of the reference channel starting from the test channel side (h^*=16.2 nm). (**b**) Meniscus moves with a constant speed and the filling rate is 2 orders of magnitude slower than the first experiment, starting from the reference channel.

Theoretical values of η normalized by the experimental η yield the increase in the resistance as a function of height: $\alpha = \frac{\eta_{theoretical}}{\eta_{actual}} = \frac{R_{test,actual}}{R_{test,theoretical}}$. An implicit assumption here is that resistance of ~120 nm reference channels can be approximated by the classical equation for R, otherwise a slight increase in the measured α can be expected. Our results

indicate that for the 59 nm channels the actual resistance is very close the theoretical predictions and as the test channel height becomes smaller, difference between the actual and the theoretical resistance becomes more pronounced, with the ratio reaching $\alpha = 1.45 \pm 0.31$ in case of 7 nm channels (Figure 2.7.b). As it's clear from the definition of R, within the realm of hydrodynamics the liquid-surface interaction can manifest itself in the boundary conditions, i.e., slip/no-slip boundary condition, and/or in the form of an altered liquid property (i.e., density and viscosity). In terms of the boundary condition, while slip boundary condition has been reported for the hydrophilic channels (Ho *et al.* 2011; Lee *et al.* 2012), however any non-zero slip lengths could only reduce the resistance and hence cannot serve as an explanation for our results (here $R_{theoretical}$ is calculated with $l_s = 0$). In terms of liquid properties, several of previous studies have employed long-range electrostatic forces to explain the slow capillary filling in hydrophilic nanochannels through the Debye-layer correction for the hydraulic resistance. However, this effect known as electroviscosity has been proven insignificant for realistic estimates of central parameters (Mortensen and Kristensen 2008; Phan *et al.* 2009; Wang *et al.* 2010). On the other hand, change in the interfacial liquid properties due to short-range interaction forces can be another way to explain the increased resistance (Haneveld *et al.* 2008; Li *et al.* 2012). When water is in contact with a polar surface, water dipoles reorient making formation of stagnant/tenacious hydration layers at the interface favorable.

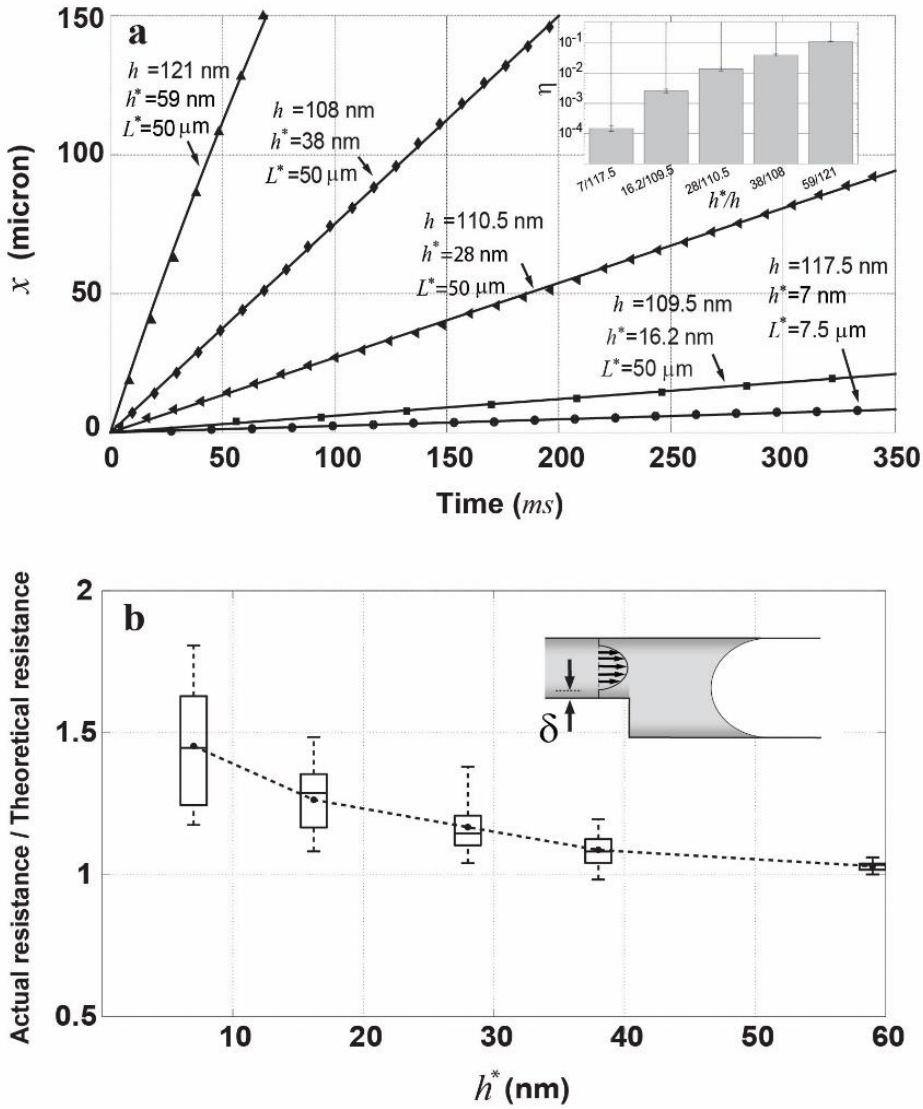

Figure 2.7: (**a**) Representative curves of the location of meniscus versus time for hybrid nanochannels with different η's. Solid lines are fitted curves to the experimental results (markers). (**b**) Ratio of the actual resistance of the nanochannels to the theoretical resistance (α) vs nanochannel height. Formation of a stagnant layer of water on the silica surface with the thickness of δ=4.3, 7.1, 8.9, 8, and 7 angstroms (from shallow to deep) can explain the increased resistance. The error bars contain all of the measurements.

Experimental studies concerning fluidity of confined water between hydrophilic surfaces less than a few nanometers apart have demonstrated 1 to 6 orders of magnitude increase in water viscosity due to ordering of the water structure at the hydrophilic surfaces (Becker

and Mugele 2003; Gao *et al.* 2007; Goertz *et al.* 2007; Leng and Cummings 2005; Ortiz-Young *et al.* 2013), although there are other studies indicating this increase is not more than three-folds (Mante *et al.* 2014; Raviv *et al.* 2001; Sendner *et al.* 2009). Moreover, MD simulations indicate a three to five fold increase in water density near hydrophilic surfaces (Gao *et al.* 2007; Mante *et al.* 2014; Sendner *et al.* 2009). Such changes in interfacial liquid properties, or formation of an ice-like network of water adsorbed on silica (Asay and Kim 2005), can reduce the effective flow cross-sectional area and hence be a possible explanation for our measurements. According to our measurements, a stagnant layer of water on the silica surfaces with thickness of $\delta = 7.06^{+1.84}_{-2.76}$ Å corresponding to two to three layers of water molecules can explain the observed increase in the mass flow resistance. However, due to the fabrication method we have used that involves anodic bonding, there is a concern about decrease in channel height after bonding. (See the next section) Of course if any reduction in the channel height is going to happen after bonding, it must be subtracted from the measured thickness of the hydration layer. When comparing our results with previously reported hydration layer thickness of 5 angstroms (Gruener *et al.* 2009) or 4 angstroms (Li *et al.* 2012) in capillary filling studies one may argue that heights of our channels might have decreased by a few angstroms after bonding. However, it is worth noting that our measured value is in agreement with infrared reflection spectroscopy of water adsorbed on hydrophilic silicon oxide surfaces, which revealed that the first three adsorbed water layers (~8.4 angstroms thick) have an ice-like configuration (Asay and Kim 2005). Haneveld et al. also reported a thickness of $\delta = 9 \pm 5$ angstroms for the hydration layer in sub-10 nm nanochannels in their capillary filling study (Tas *et al.*

2004), although their results may have overestimated the thickness of the hydration layer as they attribute deviations of both capillary pressure and hydraulic resistance from theory to the increase in hydraulic resistance. Additional possible sources of error for such measurements include capillary pressure induced channel wall deflection and dissolution of silica in water over time (Andersen *et al.* 2011). Nevertheless, the capillarity-induced channel wall deflection during water filling (Haneveld *et al.* 2008; Tas *et al.* 2003; Van Honschoten *et al.* 2009; Van Honschoten *et al.* 2007) can be safely ignored for our nanochannels because of the thick cover layers (i.e., 0.5 mm thick glass/silicon). Moreover, the effect of channel wall dissolution with dissolution rate ~45 pm/hr (Andersen *et al.* 2011), a phenomenon observed when water flows in nanochannels over a long period, e.g. 48 hrs, is negligible as it only takes 1~2 minutes to perform multiple experiments in each nanochannel.

2.5.3 Decrease in channel height after anodic bonding

Although the height of nanochannels before bonding have been very accurately measured several times with AFM to ensure the consistency between different measurements, height of the nanochannels after bonding may not be the same as before bonding. It's known that applying too large of a voltage during anodic bonding may cause a deflection equal to the height of nanochannels, in which case nanochannels collapse. This deflection is a function of applied voltage, channels' width and the thickness of oxide layer (Duan and Majumdar 2010). In our case, however, we observe that increasing the voltage more than a certain value first decreases the height of channels without channels collapsing, and by continuing

to increase the applied voltage finally nanochannels collapse. In order to understand this phenomenon and find a bonding recipe that ensures minimal change in the channel heights we used a hybrid channel with 16.2 nm test channel. First we bonded the silicon chip with glass by applying 250 Volts at 400^{o}C and performed the capillary filling experiment, after oxygen plasma. Next, we applied 300 V to the same chip and re-bonded the chip (at the same temperature) and did the capillary experiment. We continued this experiment with 400 and 450 volts too. The results are presented in Figure 2.8. At 250 Volts, the channels are not completely bonded and a large variation in filling speed from one channel to another is observed. (Figure 2.8.a) Imperfect bonding at this relatively low voltage gives rise to the measured values of actual resistance to be smaller than theoretical values for some channels in Figure 2.8c, shown by dashed ellipses. In addition complex flow pattern between channels caused irregularities in the measured x-t curves for this chip which gave rise to large fitting errors and yielded some very large resistance values, too.

As the voltage increases to 350 V filling speed of different channels become consistent. (Figure 2.8.b and 2.8.c) By further increasing the applied voltage to 400 V, the curve maintains its shape and only shifts upward (the blue and black curves in Figure 2.8.c) which can be explained on the basis of decrease in the channel heights by 1.5 nm in case of 400 V bonding. (Figure 2.8.d) Results of 450 V bonding —obtained by another chip of exact same dimensions — does not show appreciable difference compared with 400 V bonding. (Figure 2.8.e) Further increasing the voltage collapses the channel, and even 450 V cannot be applied to the 7 nm channels. According to our experiments 350 V (at 400 ^{o}C for 300 nm silicon oxide layer) is the minimum voltage that ensures all the channels are bonded and the channel heights have been minimally affected. Of course, if any change in the

channel height is going to happen, it must be subtracted from the measured thickness of the hydration layer. In the other word, 7 Å is the upper limit for the thickness of the hydration layer and for example compared with previously measured hydration layer of 5 Å (Gruener *et al.* 2009) one may argue that heights of our channels might have decreased by ~4 Å after bonding. Finally, we would like to mention that results presented in Figure 2.8 allows us to conclude that the hybrid channel scheme is a reliable tool to measure very small differences in the channel heights.

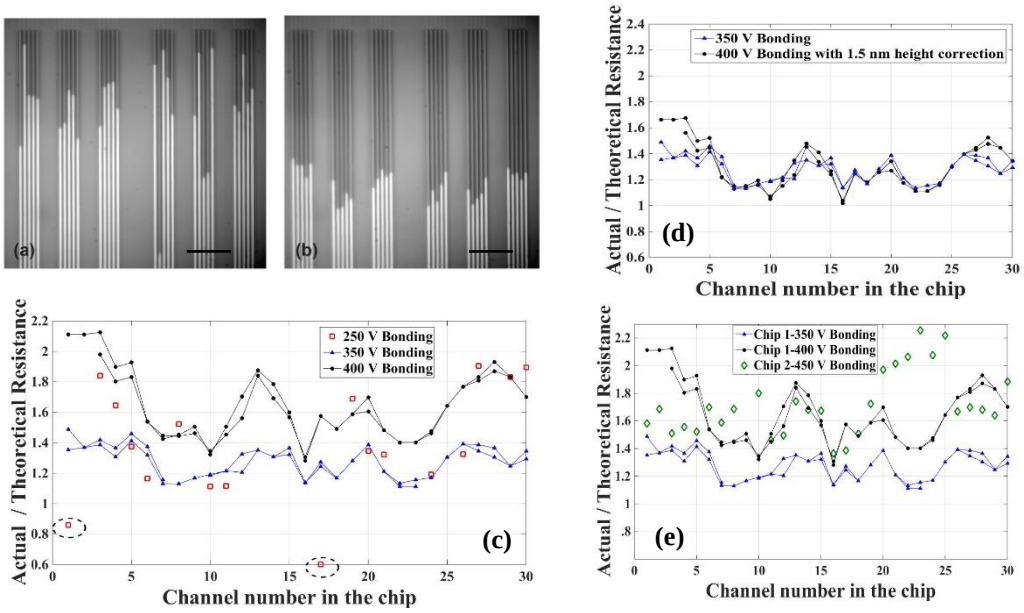

Figure 2.8: (**a**) Snapshot of capillary filling in a 16.2 nm/109.5 nm hybrid channel bonded with 250 V and (**b**) 350 V. 250 V is not enough to form perfect bonding and thus a large variation in the capillary speed is observed. Further increasing the voltage to 350 makes all the channels consistent. (The scale bars are 50 μm).(**c**) The ratio of the actual to theoretical resistance for the same chip bonded at different voltages. Two black (blue) lines are two trials under the same conditions. (**d**) Applying a 1.5 nm height correction to the results obtained with 400 V bonding yields very consistent results as obtained with 350 V bonding. (**e**) Further increasing the voltage to 450 V does not change the channel height.

After the experiments the glass layer of the bonded chip was dissolved in HF and again 300 nm oxide was grown on the Si chip. Channel heights in this chip was measured using

AFM and perfect agreement with initial measurement was observed. This indicated that any deformation as a result of bonding occurs to the glass and not to the silicon chip. It can be shown that glass deflection cannot be more than a few nanometers and for such a small deflection, plastic deformation is not expected. Instead, we hypothesize that conformation of the glass to the round edges of the silicon chip, as shown in Figure 2.9, causes a reduction in channel height. If so, creating sharp edges can reduce the extent of this problem, and thus lithography and etching steps in the fabrication become more important. This hypothesis can explain why increasing bonding voltage from 400 V to 450 V did not change the channel height and suggests that 400 V is enough to conform the glass capping layer to the round edges of the silicon substrate. It's also probably because of this reason that the shallowest channel tested (7 nm height) yields smallest value for the thickness of the hydration layer. (4.3 Å) In fact, for the 7 nm channel the etching time is shortest and the edges are expected be sharper than deeper channels. Further research is required for better understanding of the post-bonding channel geometry.

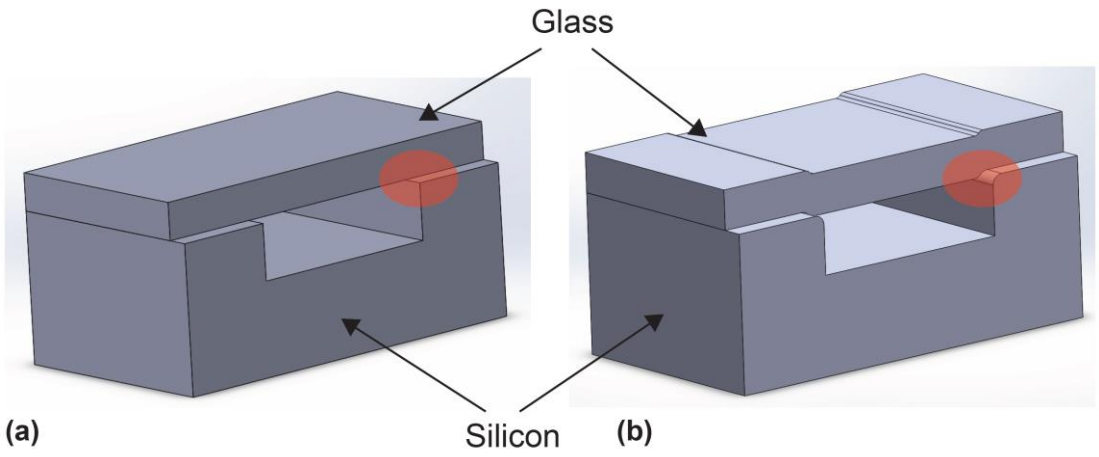

Figure 2.9: Effect of round edges on post-bonding channel height. (**a**) Sharp edges prevent any change in channel height after bonding. (**b**) Capping layer conforms to the round edges. (image not in scale)

2.5.4 Deterioration of the surface hydrophilicity, and dominance of the corner flows

Another aspect of the capillary flow at the nanoscale that we observed was the increase in the correction factor C over time. In fact, the smallest correction factor in each channel was usually achieved in the first few times a chip was tested and it increased afterwards, despite all the experiments were performed after applying oxygen plasma to the chips. Even in cases which after fabrication of a chip no experiments was performed with it and the chip was stored in a water dry storage for later use, an increased correction factor C was measured the first time it was tested which clearly showed the surface quality of the channels deteriorate over time. The correction factor C for the reference channels of such a chip reached the values of up to 2 over time (Figure 2.10.a). Therefore, for the purpose of this paper only the results of the experiments with fresh chips (right after Piranha cleaning, bonding with glass, and applying oxygen plasma) were used. However study of

the deteriorated chips enabled us to better evaluate the performance of the hybrid nanochannels scheme, and also to get some insight about mechanism of the formation of bubbles in the nanochannels. When water is introduced from the test channel side of an old unused chip, some air pockets were trapped in several spots along the channel (Chauvet *et al.* 2012; Thamdrup *et al.* 2007; van Delft *et al.* 2007). These bubbles had not been observed for most of the fresh chips of similar dimensions, or the results were discarded otherwise (Figure 2.10.b). Repeating the experiment several times in a few consecutive days indicated that air pockets are always consistently trapped in the same spots (Figures 2.8.c, 2.8.d) and indicated that at those spots silica surface is relatively hydrophobic. On the other hand, when water was introduced from the reference channel side no air was trapped in those spots (Figure 2.10.f), indicating that in addition to the local hydrophobicity of the surface acting as the weak points along the channel, the hydraulic resistance behind the meniscus is another factor giving rise to entrapment of air in the channel. In fact, when the meniscus reaches a hydrophobic site it is momentarily distorted. (Figure 2.10.g) This distortion along with increase in the contact angle give rise to a reduced capillary pressure. Now if the resistance behind the meniscus is small enough to allow the reduced capillary pressure drive the water through the entire channel, no air would be trapped; otherwise, water flows from the corners and forms another meniscus downstream, leaving some air behind. (Figure 2.10.h) Finally the air pocket forms a bubble because of the liquid pressure. (Figure 2.10.i)

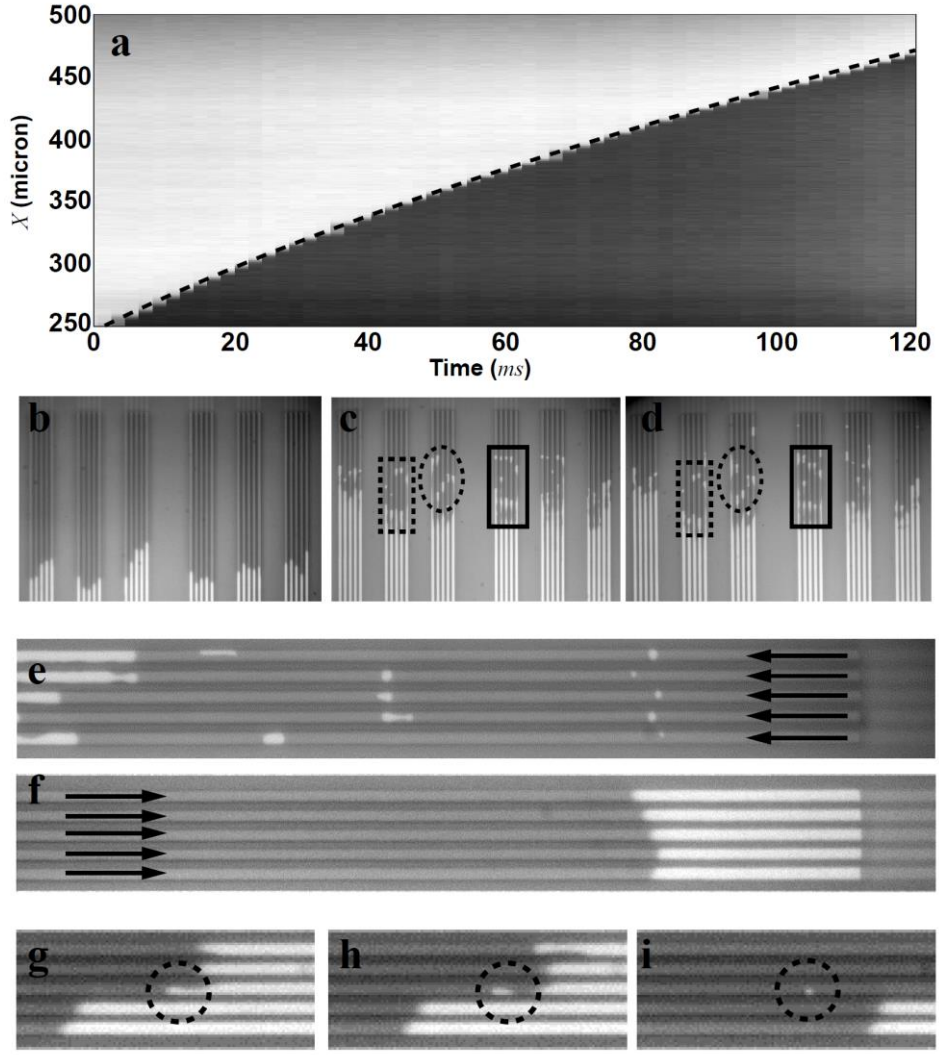

Figure 2.10: (**a**) $X-t$ curve of the meniscus of a chip with deteriorated surface hydrophilicity (C=1.98). (**b**-**d**) No trapped air or bubble is observed when water flows from test side of a fresh 28 nm hybrid channel. (**b**) For the deteriorated chip, however, bubbles are observed and they are consistently formed in the same spots. (**c** and **d**) (**e**,**f**) When water in introduced from the test side of a deteriorated chip (**e**), bubbles are consistently formed at several spots along the channels. But for the same chip when water in introduced from the reference side no bubble is observed. (**f**) (**g**-**i**) Formation of a bubble when a meniscus meets a hydrophobic site. The reduced capillary pressure at a hydrophobic site combined with a large resistance behind the meniscus make water only flow through the sharp corners, leaving bubbles behind.

Corner flows even in case of fresh chips with no hydrophobic sites can be observed. Here we experimentally observed that choice of an excessively long test channel by imposing a huge resistance to the reference channel causes the corner flows to become the dominant

mode of liquid transport (Figure 2.11). Since flow at the sharp corners moves quite faster than the bulk flow (Dong and Chatzis 1995; Ransohoff and Radke 1988; Weislogel and Lichter 1998) and can easily fill the nanochannels—as narrow as 3 μm —with a different speed, they are considered a major problem is accurate measurement of the capillary flows. The hybrid nanochannel design, however, gives us the latitude to eliminate or greatly reduce the corner flows by adjusting the total hydraulic resistance through right choice of test channel length (L^*) and adjusting the driving capillary pressure by right choice of the reference channel height (h).

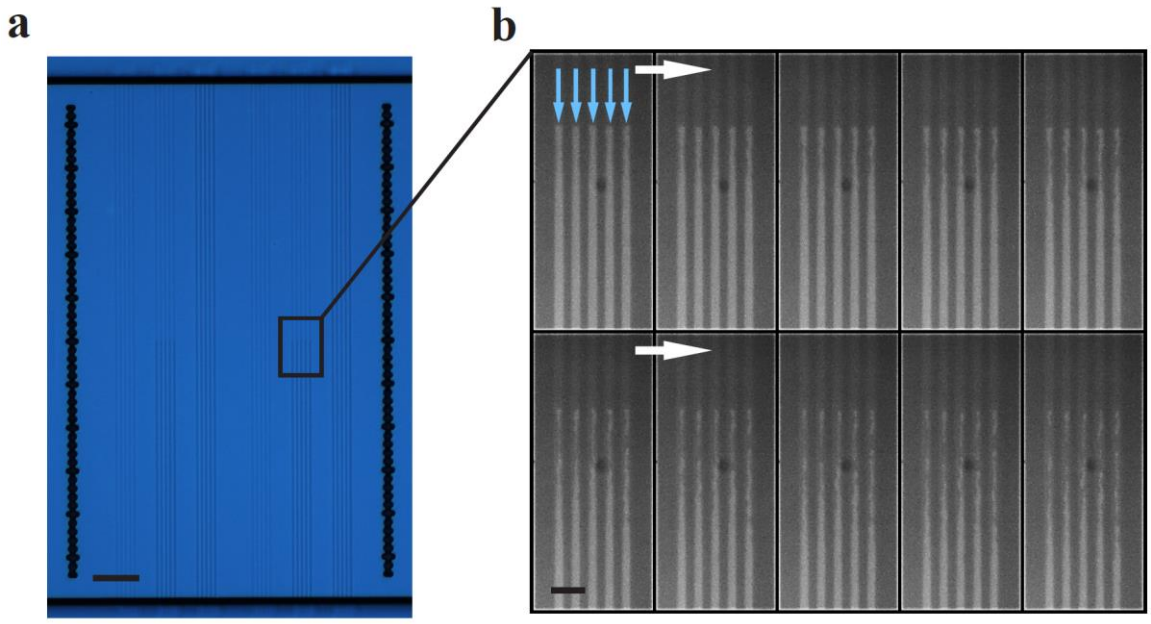

Figure 2.11: (**a**) Microscope image of a chip consisting of hybrid nanochannels with $h^* = 18.8$ nm, $h = 39.7$ nm, and $L = L^* = 300\ \mu m$, intended to characterize both deep and shallow nanochannels by introducing water from either sides. (**b**) 10 microscope shots of the capillary filling of five neighboring hybrid nanochannels. This design of hybrid nanochannels failed to characterize the shallow channel side, because the resistance imposed by the long test channel caused the corner flows to become the dominant mode of filling. Corner flows leave large pockets of air behind and don't allow formation of menisci. This problem was overcome by choice of shorter test channels and deeper reference channels. (scale bars in **a** and **b** are 50 and 10 μm, respectively)

We've been able to take advantage of the chips with deteriorated surface properties to better evaluate the hybrid nanochannel scheme and it's capability in decoupling the hydraulic resistance from the driving pressure. Using an old unused hybrid chip (a few months after bonding the chip) with $h^* = 28$ nm experiments were performed, after applying Oxygen Plasma (500 Watts, 500 SCCM O_2, 30 minutes). By introducing water from the reference channel side the correction factor C was measured to be $C = 1.84^{+0.29}_{-0.16}$, about 50% larger than the fresh chips (Figure 2.12). When water is introduced from test channel side it advances for about ~50 μm before any bubble is formed. We used this part of the data to find α for this channel height. Results showed that while the value of A in the reference channel has significantly decreased, the calculated α maintained its value within 10% of the fresh chips ($\alpha = 1.05^{+0.16}_{-0.07}$), verifying that hybrid nanochannel scheme can avoid a large error arising from any changes in the pressure term (Figure 2.12). We hypothesize that the 10% decrease in the hydraulic resistance can be due to formation of hydrophobic sites in the test channels similar to ones observed in the reference channels. Nonetheless, because the entire process of change in hydrophilicity of the surfaces could not be easily controlled and hence due to lack of experimental support, we could not further investigate the alteration of the hydraulic resistance of deteriorated silica channels.

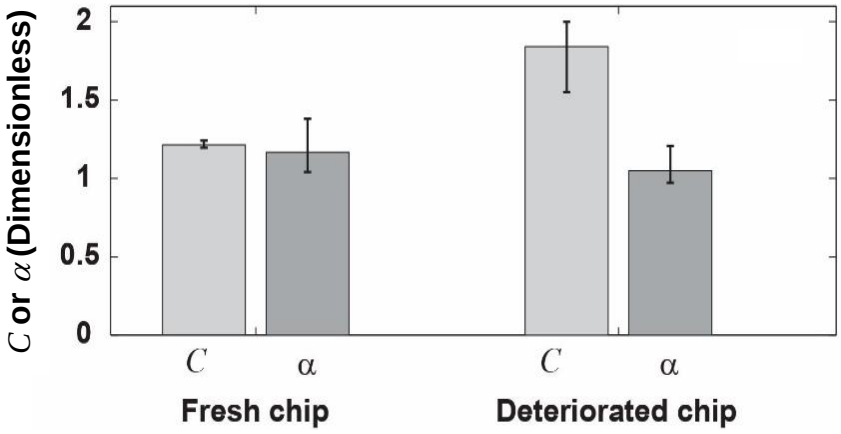

Figure 2.12: Characterizing the increased hydraulic resistance for a 28 nm channel measured with two chips of different hydrophilicity. Decrease in the capillary pressure due to change in hydrophilicity of the surfaces does not impact the measured hydraulic resistance.

2.6 Hybrid nanochannel scheme's advantages and disadvantages

Besides decoupling the driving capillary pressure term from the hydraulic resistance and enabling us to characterize the hydraulic resistance of nanoscale conduits, the hybrid nanochannel design offers some other advantages. For example, previous measurements of capillary flow in sub-10 nm channels (Haneveld *et al.* 2008; Oh *et al.* 2010) other than encompassing both deviations of the capillary force and the hydraulic resistance from theory, suffered from elastic deformation and contraction of the channel height due to the huge negative capillary pressure at the meniscus (Tas *et al.* 2003; Van Honschoten *et al.* 2009; Van Honschoten *et al.* 2007). For a 7 nm channel the negative capillary pressure can be as high as 20 MPa, which can cause a deformation in the channels at the location of meniscus, giving rise to an increased capillary pressure and also increased hydraulic resistance which is known to boost the filling rate (Van Honschoten *et al.* 2007). This error, however, can be avoided using our method as data is only collected when meniscus moves

in the reference channels of large height. Needless to say, in case of our measurements due to large thickness of the glass and silicon wafers (500 μm) and small width of the channels (3 μm) elastic deformation can be safely neglected, but if the nanochannels lack strong mechanical supports, this deformation can be significant. Another advantage of this method is that since only the ratio of the fluid properties in the test and reference channels determines η (and value of A is experimentally found), use of this method to a large extent eliminates the errors associated with the temperature dependence of fluid properties. This method other than characterization of the hydrophilic nanochannels can be used to characterize 1-D nanotubes and nanoporous media, even if they are hydrophobic. In fact characterization of hydrophobic conduits/nanoporous materials which don't allow for spontaneous filling can be done through their integration with a hydrophilic reference channel. Similar approach that has been explained would be used for characterization of such hydrophobic-hydrophilic hybrid channels, except that for the experiment that starts from the test channel side (hydrophobic side) we have to provide some external pressure to drive the water through the hydrophobic test channel until water enters the hydrophilic reference channel. The external pressure can be immediately removed once water enters the hydrophilic part, or it can be maintained to further drive water through the hydrophilic reference channel. In the second case, when introducing water from the hydrophilic channel side for the second measurement, the same external pressure also needs to be applied. In case of CNTs, it has been previously shown that water spontaneously fills the CNT and applying extra pressure is not needed (Qin *et al.* 2011).The real challenges of CNT flow characterization include integration of CNTs in a hybrid setting and tracking the

location of meniscus as a function of time. We are currently working on solving these two challenges and will report our results in another paper.

The realm of validity of the hybrid nanochannels scheme is the validity of Washburn equation, which if for any reason is violated, e.g., due to formation of bubbles in the nanochannels or corner flows, the method may not be applied. In addition, if the liquid of interest is non-evaporating, or cannot be removed from the hybrid channels after the first experiment, this method fails to work. Finally, rate dependence of the dynamic contact angle can introduce error to the results of this method. In our method, the velocity of meniscus can be widely different between the two experiments, i.e., the filling experiment that starts from the test channel side and another one that starts from the reference channel side, which means the driving capillary pressure can be different between the two experiments. However, in our measurements since the capillary numbers in all cases are very small ($Ca = \frac{u\mu}{\sigma} < 10^{-4}$ with u being the velocity), variations in $\cos(\theta)$ due to different filling rates is no more than 1% (Ralston *et al.* 2008), consistent with previous contact angle measurements in nanochannels (Li *et al.* 2012).

2.7 Conclusions

Our experimental results characterize water transport in sub-10 nm hydrophilic nanochannels and lends more validity to the use of classical hydrodynamics at the nanoscale. The proposed hybrid nanochannel scheme provides insight into collective effects of the boundary condition as well as the properties of a nanoscale confined liquid, and can open the prospect for accurate characterization of liquid transport through 2-D

nanochannels, 1-D nanotubes, as well as nanoporous media. In particular, characterization of water transport in hydrophobics CNTs and graphene nanochannels can be improved through their integration with hydrophilic channels in the form of hydrophobic-hydrophilic hybrid channels. This method has the potential to be standard for nanofluidic flow characterization and can serve to advance studies of many nanofluidics-involved disciplines, including membrane separation, soil science, colloid chemistry, biology and physiology.

CHAPTER 3: Geometrical Control of Ionic Current Rectification in a Configurable Nanofluidic Diode

Control of ionic current in nanofluidic system and development of the elements analogous to electrical circuits has been subject of theoretical and experimental investigations over the past decade. Here we theoretically and experimentally explore a new technique for rectification of ionic current using asymmetric 2D nanochannels. These nanochannels have a rectangular cross section and a stepped structure consisting of a shallow and a deep side. Control of height and length of each side enables us to obtain optimum rectification at each ionic strength. A 1D model based on Poisson-Nernst-Planck equation is derived and validated against the full 2D numerical solution, and a nondimensional concentration is presented as a function of nanochannel dimensions, surface charge and the electrolyte concentration that summarizes the rectification behavior of such geometries. The rectification factor reaches a maximum at certain electrolyte concentration predicted by this nondimensional number and decays away from it. This method of fabrication and control of nanofluidic diode does not require modification of the surface charge and facilitates the integration with lab-on-a-chip fluidic circuits. Experimental results obtained from the stepped nanochannels are in good agreement with the 1D theoretical model.

3.1 Introduction

Nanofluidic channels with dimensions comparable to the Debye screening length portray peculiar transport characteristics due to the effect of surface charge. Ion transport in such systems has been under extensive studies due to their relevance in understanding the activity of biological ion channels (Alcaraz *et al.* 2006; García-Giménez *et al.* 2009; Miedema *et al.* 2007), as well as the prospect of exploiting them in biomedical and chemical applications. Over the past decade there has been a wealth of studies focusing on design of nanofluidic components analogous to solid-state elements, and in particular, efforts have been made to design nanofluidic transistors (Daiguji *et al.* 2005; Daiguji *et al.* 2004; Kalman *et al.* 2008; Karnik *et al.* 2006; Karnik *et al.* 2005b; Zhang *et al.* 2016) and diodes (Apel *et al.* 2011; Apel *et al.* 2001; Cervera and Schiedt 2005; Cheng and Guo 2007, 2009; Constantin and Siwy 2007; Green *et al.* 2015; Guan *et al.* 2011; Jung *et al.* 2009; Karnik *et al.* 2007; Li *et al.* 2015; Liu and Yobas 2013; Mafe and Ramirez 1997; Singh *et al.* 2011; Siwy *et al.* 2003a; Siwy *et al.* 2003b; Siwy *et al.* 2002; Siwy *et al.* 2004; Siwy 2006; Slouka *et al.* 2014; Sonin and Grossman 1972; Sun *et al.* 2016; Vlassiouk *et al.* 2009; Vlassiouk and Siwy 2007; Vlassiouk *et al.* 2008; Wei *et al.* 1997; Yan *et al.* 2009; Yossifon *et al.* 2009a) as the key elements for ionic circuits. These elements have been widely used for sensing, separation, and concentration of biomolecules such as nucleic acids, proteins and DNA (Karnik *et al.* 2006; Karnik *et al.* 2005b; Liu and Yobas 2013; Slouka *et al.* 2014; Vlassiouk *et al.* 2009), single cell analysis (Zhang *et al.* 2016), and precise control of the transport of ions and charged molecules (Apel *et al.* 2011; Apel *et al.* 2001; Cervera and Schiedt 2005; Cheng and Guo 2007, 2009; Constantin and Siwy 2007; Daiguji *et al.* 2005;

Daiguji *et al.* 2004; Green *et al.* 2015; Guan *et al.* 2011; Jung *et al.* 2009; Kalman *et al.* 2008; Karnik *et al.* 2007; Kim *et al.* 2007; Li *et al.* 2015; Mafe and Ramirez 1997; Singh *et al.* 2011; Siwy *et al.* 2003a; Siwy *et al.* 2003b; Siwy *et al.* 2002; Siwy *et al.* 2004; Siwy 2006; Slouka *et al.* 2014; Sonin and Grossman 1972; Stein *et al.* 2004; Sun *et al.* 2016; Vlassiouk and Siwy 2007; Vlassiouk *et al.* 2008; Wei *et al.* 1997; Yan *et al.* 2009; Yossifon *et al.* 2009a).

Rectification of ionic current in nanofluidic channels is a result of asymmetry in the system. While a symmetric nanofluidic channel acts analogous to a solid-state resistor, when the symmetry breaks a nanofluidic diode is realized. A nanochannel with asymmetric geometry (Apel *et al.* 2011; Apel *et al.* 2001; Cervera and Schiedt 2005; Constantin and Siwy 2007; Siwy *et al.* 2003b; Siwy *et al.* 2002; Siwy *et al.* 2004; Siwy 2006; Vlassiouk and Siwy 2007; Wei *et al.* 1997), surface charge distribution along the nanochannel, (Cheng and Guo 2009; Green *et al.* 2015; Guan *et al.* 2011; Karnik *et al.* 2007; Li *et al.* 2015; Singh *et al.* 2011; Vlassiouk *et al.* 2008; Yan *et al.* 2009) electrolyte concentration (Cheng and Guo 2007; García-Giménez *et al.* 2009) or pH (Alcaraz *et al.* 2006; García-Giménez *et al.* 2009) at the nanochannel terminals, or concentration polarization (Jung *et al.* 2009; Yossifon *et al.* 2009a) conducts ionic current preferentially in one direction and inhibits the ionic current in the opposite direction. Each of these rectification methods have been employed and extensively studied by researchers in the past decade. Yet, utilization of this transport phenomena in nanofluidic channels is hampered by difficulties in their controlled design and fabrication as well as their integration in a larger fluidic circuits. The existing rectification methods based on conical nanopipettes/nanopores, (Cervera and Schiedt 2005;

Constantin and Siwy 2007; Siwy *et al.* 2003a; Siwy *et al.* 2003b; Siwy *et al.* 2002; Siwy *et al.* 2004; Siwy 2006; Vlassiouk and Siwy 2007; Wei *et al.* 1997) bipolar membrane systems (Mafe and Ramirez 1997; Sonin and Grossman 1972; Sun *et al.* 2016) or asymmetric membranes (Apel *et al.* 2011; Apel *et al.* 2001) have limited control over their geometries and are very difficult to integrate in 2D lab-on-a-chip devices. On the other hand, nanofluidic channels with patterned surface charge as the symmetry breaker have been shown to effectively rectify the ionic current (Cheng and Guo 2009; Green *et al.* 2015; Guan *et al.* 2011; Karnik *et al.* 2007; Li *et al.* 2015; Singh *et al.* 2011; Vlassiouk *et al.* 2008; Yan *et al.* 2009). Nevertheless, this method requires access to and surface modification of only certain part of a nanochannel, which may not be easily possible in larger fluidic circuits. In addition, some of the surface modification methods are subject to decay over time which may limit the diode's life time to as short as several hours. Alternative method is to apply a gate voltage along certain part of the nanochannel which makes the fabrication more complicated (Guan *et al.* 2011). In this paper we present a technique for rectifying current that is solely based on geometry control and does not require any surface modification, and yet can be easily designed, fabricated, and integrated in a larger circuit with more components. The theoretical background necessary for understanding the rectification behavior is presented as a 1D numerical model, and the numerical results are compared and validated against experimental results and a good agreement is observed. This nanofluidic diode can be configured to yield optimum current rectification at electrolyte concentration of interest.

3.2 Theoretical Background

3.2.1 Problem Description

The problem geometry is schematically shown in Figure 3.1. The nanochannel has a stepped structure and is divided into two parts with length L_1 having a height of $h_1$and length L_2 at height h_2. Width of both parts of the nanochannel is w, and without loss of generality let's assume $h_2 > h_1$.

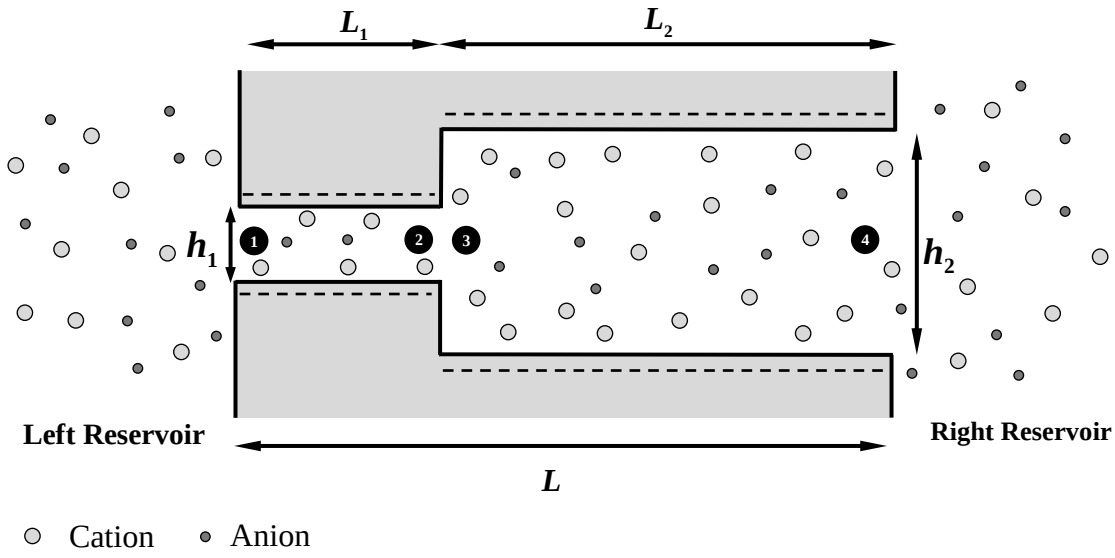

Figure 3.1: The nanochannel geometry consisting of a shallow and a deep side with rectifying property.

The Poisson-Nernst-Planck equation relating charge density and electrostatic potential can be employed to solve this problem:

$$\nabla^2\varphi = \frac{-\sum z_i n_i\, e}{\varepsilon\varepsilon_0} \tag{3.1}$$

$$\frac{\partial n_i}{\partial t} + \mathbf{u}.\nabla n_i = \nabla.\left(D_i\nabla n_i + n_i\,\frac{D_i z_i e}{k_b T}\nabla\varphi\right) \tag{3.2}$$

where n is the concentration of species with the index i referring to either of cations or anions, D_i is the diffusivity of species, k_b is the Boltzmann constant, T is the temperature,

z_i is the valence, e is the elementary charge, φ is the electric potential, and $\mathbf{u}$ is the velocity vector. Assuming the electroosmotic flow is negligible ($\mathbf{u} = 0$) and for steady state condition the Nernst-Planck equation can be further simplified. One should note that it is not trivial that electroosmotic flow can be neglected for all nanochannel heights and electrolyte concentrations (Daiguji *et al.* 2004; Haywood *et al.* 2014). Nevertheless, for the sake of simplicity here this terms is neglected and a complementary discussion will be presented in the experimental results section. These equations can be numerically solved using Finite Element Method (FEM) to yield the current as a function of the applied voltage for the geometry of interest. Alternatively, a 1D model can be constructed based on these equations (Karnik *et al.* 2007) which is easy to solve without a finite element package, and facilitates parametric study of the system under investigation. This system of equation for monovalent ions ($|z_i| = 1$) with similar diffusion coefficient D for both cations and anions is written as (see Appendix 2):

$$\bar{N}_2{}^2 - 1 = \bar{N}_3{}^2 - \frac{1}{\tau^2} \tag{3.3a}$$

$$\bar{\varphi}_2 - \bar{\varphi}_3 = ln\frac{\bar{N}_2 + 1}{\bar{N}_3 + \frac{1}{\tau}} \tag{3.3b}$$

$$\bar{M}l = -(\bar{N}_2 - \bar{N}_1) + (\bar{\varphi}_2 - \bar{\varphi}_1) \tag{3.3c}$$

$$\bar{M}(1 - l) = -(\bar{N}_4 - \bar{N}_3) + (\bar{\varphi}_4 - \bar{\varphi}_3) \tag{3.3d}$$

$$l = \left(\frac{\bar{N}_1}{\bar{M}} + \frac{\bar{I}}{\bar{M}}\right)\left[1 - \exp\left(\frac{\bar{\varphi}_2 - \bar{\varphi}_1}{\bar{I}}\right)\right] + \frac{1}{\bar{M}}(\bar{\varphi}_2 - \bar{\varphi}_1) \tag{3.3e}$$

$$1 - l = \left(\frac{\bar{N}_3}{\bar{M}} + \frac{\bar{I}}{\bar{M}}\right)\left[1 - \exp\left(\frac{\bar{\varphi}_4 - \bar{\varphi}_3}{\bar{I}}\right)\right] + \frac{1}{\bar{M}}(\bar{\varphi}_4 - \bar{\varphi}_3) \tag{3.3f}$$

In this equation, the nondimensional values of $\bar{x}\ \bar{\varphi}, \bar{N}, \bar{M}, \bar{I},\ \tau$ are defined as:

$$\bar{x} = \frac{x}{L}, \qquad \bar{\varphi} = \frac{\varphi}{\frac{k_b T}{e}}, \qquad \bar{N} = \frac{N}{\frac{2\sigma}{eh_1}},$$
$$\bar{M} = \frac{M}{2\sigma D/eL}, \qquad \bar{I} = \frac{I}{M},\ \ \tau = \frac{h_2}{h_1} \tag{3.4}$$

with $N = n_+ + n_-$, l being the length ratio ($l = \frac{L_1}{L}$) and the indices '1' thru '4' referring to different location along the nanochannel shown in Figure 3.1. Moreover, M and I are two constants proportional the mass flow rate and the current ($i = Iwe$) that based on shallow side quantities can be written as $M = -h_1 D\frac{dN}{dx} + \frac{2\sigma D}{k_b T}\frac{d\varphi}{dx}$ and $I = -\frac{Nh_1 De}{k_b T}\frac{d\varphi}{dx}$. It's important to note that the concentration and the electric potential at the entrance of the nanochannel (points 1 and 4 in Figure 3.1) are different from the reservoirs values. However assuming an equilibrium between the reservoir and the nanochannel entrance, one can utilize the Boltzmann distribution to correlate the entrance values to the reservoir values. Assuming the left reservoir is grounded ($\varphi_{left\ res.} = 0$) and the right reservoir is biased at voltage v ($\varphi_{right\ res.} = v$) we can write:

$$N_1 = N_{res}\sqrt{1 + (\frac{2\sigma}{eh_1 N_{res}})^2} \tag{3.5a}$$

$$N_4 = N_{res}\sqrt{1 + (\frac{2\sigma}{eh_2 N_{res}})^2} \tag{3.5b}$$

$$\varphi_1 = \frac{k_b T}{e}\frac{\sigma}{|\sigma|} cosh^{-1}\left(\sqrt{1 + (\frac{2\sigma}{eh_1 N_{res}})^2}\right), \tag{3.5c}$$

$$\varphi_4 = v + \frac{k_b T}{e}\frac{\sigma}{|\sigma|} cosh^{-1}\left(\sqrt{1 + (\frac{2\sigma}{eh_2 N_{res}})^2}\right) \quad (3.5d)$$

Since $N_{left}, N_{right}, \varphi_{right}$ and φ_{left} are known, we can directly find the values for $N_1, N_4, \varphi_1, \varphi_4$.

There are six factors that dictate the diode characteristic of the stepped nanochannel, three of which are geometric, including channel height h_1, height ratio τ and the length ratio l, in addition to the surface charge, the electrolyte concentration, and the applied voltage. The aforementioned nondimensionalization allows us to see the above system of equation is only a function of the length ratio l and not the channel length (L). In fact, although the current is inversely proportional to the nanochannel length ($I = \bar{I}M = \bar{I}\bar{M}2\sigma D/eL$), the rectification factor ($\left|\frac{I_{\text{forward bias}}}{I_{\text{reverse bias}}}\right|$) remains the same for any length of channel as long as the length ratio l does not change.

3.2.2 Model Validation

Equations (3.1) and (3.2) and the associated boundary conditions were solved using the COMSOL Multiphysics Finite element Package v4.4. All six factors were varied and the results obtained were compared against the 1D model. Excellent agreement between the full numerical solution and the 1D model was observed, with error typically being ~1%. Table 1 compares the forward bias current, reverse bias current and the rectification factor obtained by these two models for a representative case of a stepped nanochannel with length $L = 50\ \mu m$, $w = 3\ \mu m$, $\sigma = -3\ mC/m^2$ and 10 mM salt concentration at $\pm 1V$.

This comparison is made to evaluate the 1D model and to ensure it has been correctly implemented.

Table 3.1. Comparison of the simulation results obtained by the 1D model and the FEM model for different heights and height ratios.

Geometric factor			Forward bias current (nA)		Reverse Bias current (nA)		Rectification Factor	
h_1	l	τ	1D Model	2D FEM	1D Model	2D FEM	1D Model	2D FEM
5 nm	0.1	5	-0.308	-0.31	0.0614	0.0618	5.01	5.02
		10	-0.664	-0.661	0.071	0.0717	9.35	9.21
		15	-0.879	-0.869	0.081	0.082	10.85	10.6
	0.5	5	-0.19	-0.19	0.059	0.06	3.20	3.18
		10	-0.195	-0.194	0.069	0.07	2.80	2.77
		15	-0.181	-0.181	0.0795	0.0802	2.27	2.25
10 nm	0.1	5	-0.553	-0.552	0.1317	0.133	4.20	4.13
		10	-1.002	-0.99	0.166	0.169	6.04	5.86
		15	-1.254	-1.234	0.201	0.204	6.24	6.04
	0.5	5	-0.278	-0.277	0.118	0.119	2.35	2.33
		10	-0.278	-0.278	0.146	0.148	1.90	1.88
		15	-0.263	-0.264	0.161	0.162	1.63	1.62

3.3 Numerical Results

The 1D model relies on the assumption of constant surface charge along the nanochannel. In addition, while accumulation of ion at the step can cause a reduction in the diffusion coefficient, here the diffusion coefficient is assumed to be constant along the nanochannel. For all the calculations, the diffusion coefficient is calculated based on the Einstein relation, $D = \frac{\mu k_b T}{e}$, with $\mu = 7.8 \times 10^{-8}\, m^2 V^{-1} s^{-1}$.

The $i - v$ curve of a stepped nanochannel with $h_1 = 5\, nm$, $\tau = 20$, $L = 600\, \mu m$, $l = 0.1$, $\sigma = -3\, mC/m^2$ and 0.01 M electrolyte is shown in Figure 3.2.a which clearly demonstrates the current rectification. The rectification factor is shown in the inset as a

function of the applied voltage. The rectification increases with voltage and can reach values up to 38 at 5 V. Further increasing the voltage is known to first cause a diffusion-limited current regime, and then again there will be the overlimiting current due to creation of a strong flow (Kim *et al.* 2007; Yossifon *et al.* 2009b). Such phenomena cannot be predicted by our model as the diffusion and the electrolyte flow from the reservoir to the nanochannel have not been accounted for. Addressing phenomena at such high voltage regimes is out of scope of this paper and the parametric study of the rectification factor is performed at 1 V in the rest of paper. To explain the current rectification, the concentration of cations and anions as well as the electric potential along the nanochannel for the forward bias and reverse bias cases are plotted in Figures 3.2.b and 3.2.c. It is clear that the forward bias corresponds to significant accumulation of both cations and anions at the step of the nanochannel, while a concentration depletion zone occurs in the same location under the reverse bias. The accumulation and depletion result from different levels of selective ion transport in the shallow and deep side of the nanochannel. Because of a relatively thick electrical double layer (i.e. larger $\frac{\lambda_d}{h}$, λ_d is the Debye screening length), the shallow side of the channel is more cation selective than the deep side. This selectivity difference would temporarily result in an imbalance of ionic current of each ion type across the step when a bias is applied. Consequently, the cation current in the shallow side of the channel would be larger than that in the deep side and the anion current in the shallow side would be smaller than that in the larger side. Under a forward (or reverse) bias, this current imbalance will cause continuous accumulation (or depletion) of cation and anion at the step until the

concentration gradient can compensate the existing imbalance of ionic current, which then leads to a steady-state.

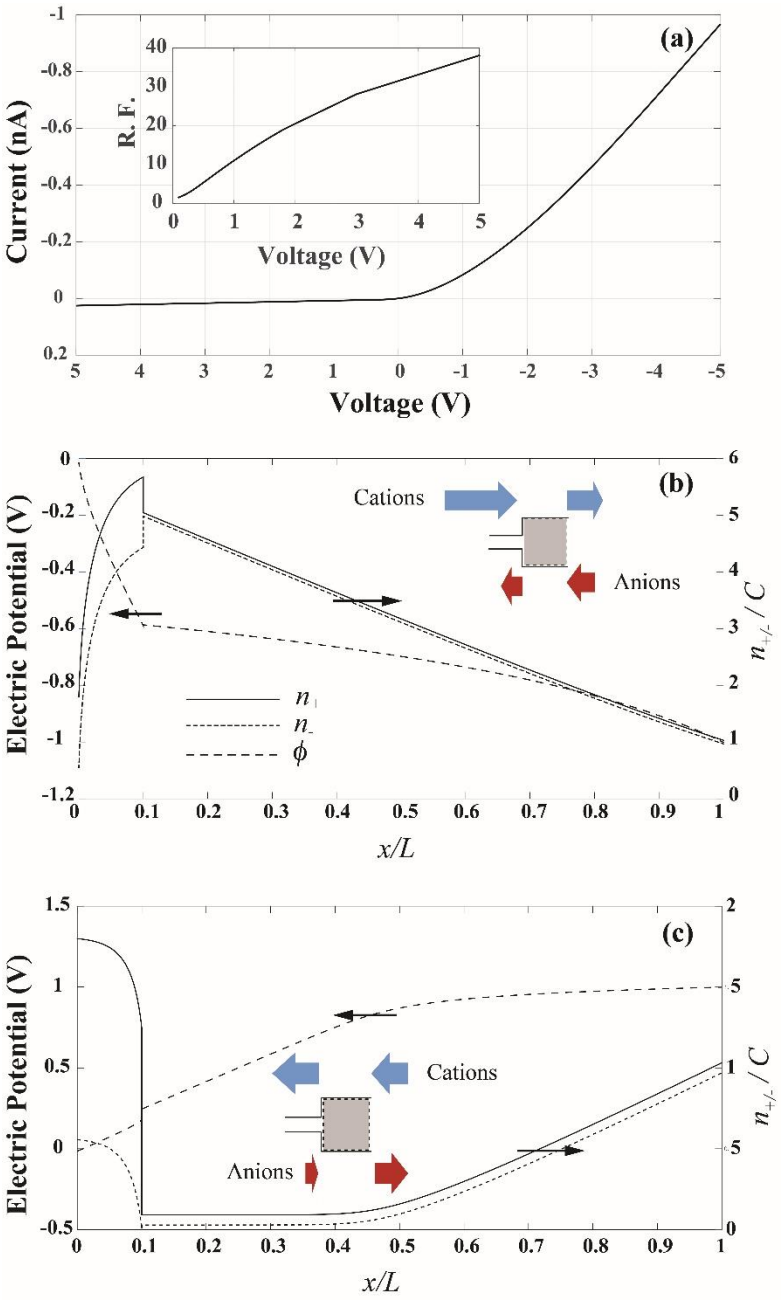

Figure 3.2: (**a**) The $i - v$ curve for a stepped channel with $h_1 = 5\ nm$, $\tau = 20$, $L = 600\ \mu m$, $l = 0.1$, $\sigma = -3\ mC/m^2$ and 0.01 M. inset: The rectification factor as a function of applied bias. (**b**) Cations, anions, and electric potential profiles along the nanochannel for the forward bias and (**c**) reverse bias for 1 V applied voltage.

Current rectification mechanism can be better understood by looking at the conductance as function of electrolyte concentration. The nanochannel conductance ($G = i/v$) and the rectification factor of a stepped nanochannel with $h_1 = 10\ nm$, $\tau = 10$, $L = 600\mu m$, $l = 0.2$, $\sigma = -3\frac{mC}{m^2}$ as a function of electrolyte concentration is presented in Figure 3.3.a. It is observed that rectification factor does not monotonically increase with the decreasing bulk concentration but shows a maximum value (C_{max}) at a concentration between $\frac{2|\sigma|}{eh_2}$ and $\frac{2|\sigma|}{eh_1}$. Such a behavior has been previously reported for single conical nanopores (Vlassiouk *et al.* 2009) or membranes with such asymmetric pores (Apel *et al.* 2011). The existence of this maximum rectification factor can be explained again by the degree of selective ion transport in two sides of the nanochannel. At very low concentrations, electrical double layers from the top and bottom surfaces overlap in both the shallow side and the deep side of the nanochannel and the difference of cation selectivity across the step becomes small. This thus decreases the imbalance of ionic current for each ion type across the step and leads to reduced accumulation (depletion) when a forward (reverse) bias is applied and hence a small rectification. This is aligned with the known fact that nanochannel conductance at low concentration is not a function of channel height, and as such the height difference in the nanochannel is not sensed. On the other hand, at high concentrations where the thickness of electrical double layer is much smaller than the height of both the shallow side and the deep side of the channel, both sides do not have much cation selectivity and current rectification diminishes as well. Therefore, the maximum rectification would occur at a concentration where the shallow channel is very cation-selective but the deep channel shows negligible selectivity. This concentration (C_{max}) is

a function surface charge and nanochannel geometry. Normalizing the concentration by $\left|\frac{2\sigma}{eh_1\tau}\right| = \left|\frac{2\sigma}{eh_2}\right|$ for different values of σ and h_1 yields a universal curve for rectification factor shown in Figure 3.3.b, if the height ratio (τ) and the length ratio (l) are kept constant. This is not unexpected and is consistent with our normalization in equation 4. In the system of equation (3.3) for a fixed applied bias all the independent factors are summarized in three nondimensional parameters, namely $\bar{N}$, τ, and l. So if the height ratio and the length ratio don't change, then the nondimensional concentration $\bar{N}(=\frac{N}{2\sigma/eh_1})$ carries all the information, and hence the aforementioned normalization results in a universal curve. On the other hand, if the other two nondimensional geometric factors (l and τ) vary, they create a more complicated picture. Different height ratios dictate different levels of ion selectivity to the deep side of the nanochannel, which in addition to changing the rectification factor, shifts the C_{max}. This is demonstrated in Figure 3.3.c with thin lines where h_1, l, and σ are kept constant and only the height ratio (τ) takes different values ($h_1 = 10\,nm$, $l = 0.2$, $\sigma = -3\frac{mC}{m^2}$). Nevertheless, as it can be seen the normalized C_{max} is not appreciably affected by variations of τ (thick lines), allowing us to predict C_{max} for arbitrary values of h_1, h_2, and surface charges. Finally, in Figure 3.3.d the effect of last nondimensional number and geometric factor, i.e., the length ratio (l) is accounted for. The length ratio (l) mainly manifests itself by altering the electric field along the nanochannel, and any change in the length ratio other than altering the peak rectification factor can shift the value of C_{max}, too (compare the squares and circles with l=0.1 and l=0.5 plotted with thin lines in

Fig. 3.3.d). Nevertheless, by using $\frac{2|\sigma|}{eh_1\tau}(1-l)$ for concentration normalization, no appreciable change in C_{max} occurs. (thick lines)

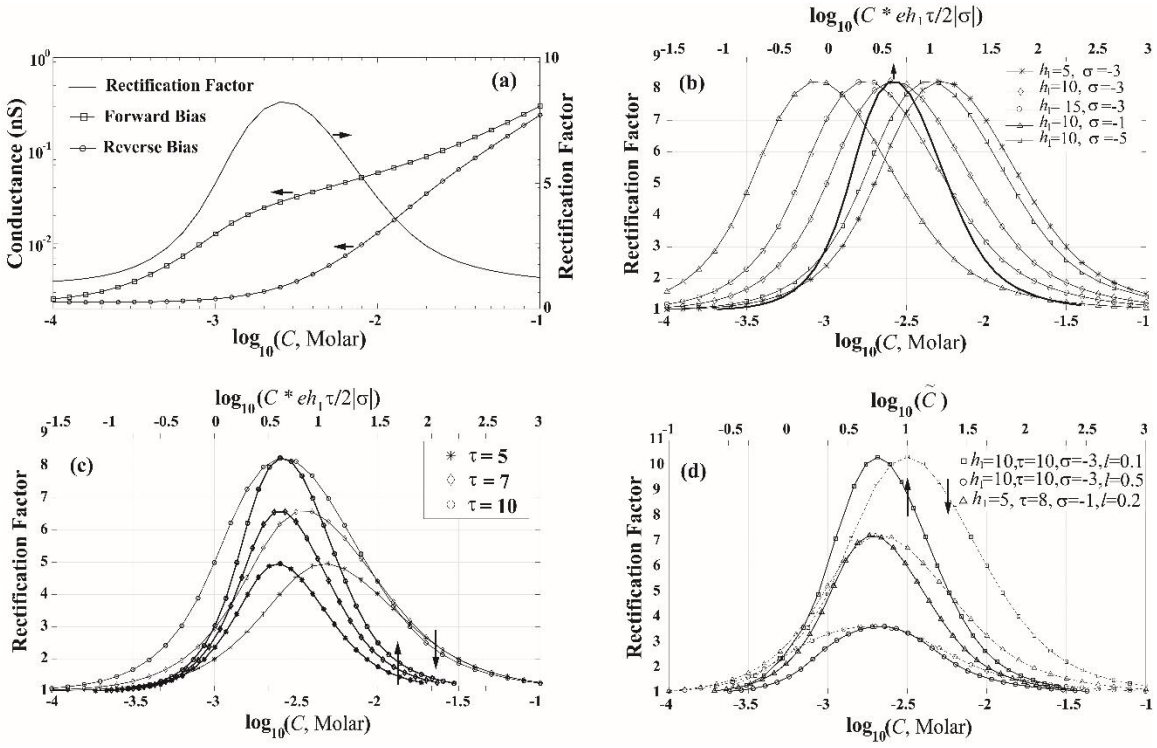

Figure 3.3: (**a**) Forward bias and reverse bias conductance and rectification factor versus concentration for $h_1 = 10\,nm$, $\tau = 10$, $L = 600\mu m$, $l = 0.2$, and $\sigma = -3\frac{mC}{m^2}$. (**b**) Rectification factor versus nondimensional concentration for different h_1 and σ ($l = 0.2$ and $\tau = 10$). (**c**) Effect of height ratio on C_{max} with other factors kept constant ($h_1 = 10\,nm$, $l = 0.2$, $\sigma = -3\frac{mC}{m^2}$) (**d**) Effect of length ratio on C_{max} and comparison of the rectification factors of two nanofluidic diodes with different heights, height ratios, length ratios, and surface charges.

This normalization indicates that C_{max} is governed by the height and length of the deep side of the nanochannel. Through this normalization ($\tilde{C} = C * \frac{eh_1\tau}{2|\sigma|(1-l)}$) we can combine all three nondimensional numbers to provide an accurate estimation of the electrolyte concentration associated with maximum rectification for any of such nanofluidic diodes. This can be better observed by comparing the squares and triangles in Fig. 3.3.d where two

completely different geometries and surface charges yield the same $\tilde{C}_{max}$. Use of this proposed nondimensional concentration, $\tilde{C}$, facilitates the design and prediction of rectification of this type of nanofluidic diodes.

Further numerical analysis yields the optimal length ratio and height ratio for maximum rectification. Figure 3.4.a presents the rectification factor as a function of the length ratio with $\tau = 10$, $\sigma = -3\ mC/m^2$ and the 10mM electrolyte concentration. It can be observed that rectification is maximized when length of the shallow side is less than one tenth of the entire nanochannel. Larger length ratios would decrease the rectification and very small length ratios ($l < 0.05$) also would sharply reduce the rectification factor. This observation can be explained on the basis of resistance of the shallow and deep sides of the nanochannel. At any given height ratio, a large length ratio causes the resistance of the shallow nanochannel to dominate the transport and a diode starts to act more like a resistor (rectification factor close to 1). Similar scenario can also occur for very small length ratios where the resistance of the shallow side becomes insignificant compared with the deep side. For this same reason the l_{max} (length ratio at which maximum rectification occurs) for a constant height ratio is not sensitive to the absolute value of the height. While the l_{max} is not sensitive to the nanochannel height, it shifts to smaller length ratios for larger height ratios as shown in Fig. 3.4.b. In fact, a large height ratio causes the resistance of the shallow nanochannel to dominate and decreasing the length ratio brings the balance between the resistance of the two sides back. Study of rectification factor versus height ratio for a constant length ratio ($l = 0.5,\ \sigma = -3\ mC/m^2,$ and 10mM concentration) presented in Fig. 3.4.c demonstrates a similar trend as in Fig. 3.4.a. Very small height ratios

depreciate the ion selectivity contrast between the shallow and deep side of the nanochannel which results in small rectification factors. Very large height ratios on the other hand make the resistance of the deep side negligible compared with the shallow side and the stepped nanochannel acts similar to its shallow side. Therefore, for any nanochannel height (h_1) there is an optimal height ratios for which the rectification factor is maximum. However unlike Figure 3.4.a, the optimal height ratio is not constant and for smaller values of h_1 it shifts to larger values to ensure the deep side is not as perm selective as the shallow side. Finally in Figure 3.4.d rectification factor versus height ratio for different values of length ratio is shown. Once again it can be seen that smaller length ratios along with larger height ratio yield larger rectifications. For the length ratios of $l = 0.1, 0.3,$ and 0.5 maximum rectification occurs at $\tau = 13$, 6, and 4, respectively.

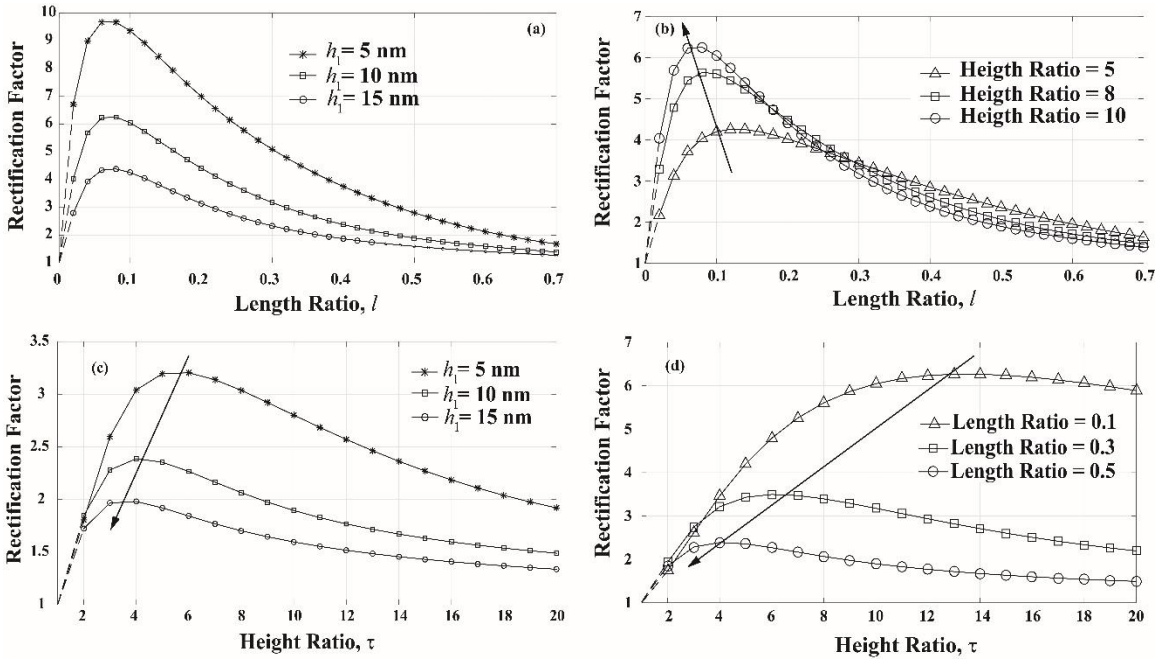

Figure 3.4: Rectification factor versus length ratio for (**a**) different heights and a constant height ratio ($\tau = 10$) and (**b**) different height rations and constant height ($h_1 = 10\ nm$). Rectification factor versus height ratio for (**c**) different heights and a constant length ratio ($l = 0.5$) and (**d**) different length ratios and a constant height ($h_1 = 10\ nm$). Calculations performed for a 10mM electrolyte concentration, with surface charge $\sigma = -3\ mC/m^2$.

3.4 Experimental Results

3.4.1. Materials and Methods

Stepped nanochannels were fabricated using the standard etching and bonding method (Alibakhshi *et al.* 2016). The stepped nanochannels were fabricated by two steps photolithography, each followed by the reactive ion etching. Before the second photoresist is spun-coat, the first layer must be hard baked over night at 120 ^{o}C to ensure it remains unaffected by the second UV exposure and maintains its structural stability during second development. Width of both sides of the nanochannels is 3 μm, the shallow side is $L_1 = 50\ \mu m$ long and the deep side is $L_2 = 550\ \mu m$ long. After etching the nanochannels, two

microchannels each 6 mm long, 1 mm wide and 40 μm deep were etched using DRIE on both terminals of the nanochannels and four 2 mm by 2 mm through holes later etched using DRIE serving as the reservoirs. Finally, 300 nm thick dry thermal oxide layer was grown on the silicon chips, and the chips were cleaned with Piranha (3:1, H_2SO_4:H_2O_2) and bonded to Borofloat glass by using anodic bonding at 400^oC and 350 Volts. A microscope image of a chip used for the experiments along with an AFM image of the location of the steps are shown in Figures 3.5.a and 3.5.b. Each chip contains 30 stepped nanofluidic channel with $h_1 = 16\ nm$ and $h_2 = 110\ nm$. A Keithley 6430 source meter (Keithley Instruments Inc.) controlled by a Matlab program was used for the conductance measurements. All the measurements were performed with the Potassium Chloride solutions using Silver/Silver Chloride electrodes in a dark Faraday cage to isolate the measurements from any external electromagnetic waves and electric fields. The pH value of the solutions was measured to be 6. Measurements were carried using a linear sweep sequence from 0 to 4 V with 20 second source delay to ensure a steady state readout. Before the measurement, 20 minutes oxygen plasma was applied to the chips to create super-hydrophilic surfaces and thus to avoid any gas entrapment in the nanochannels.

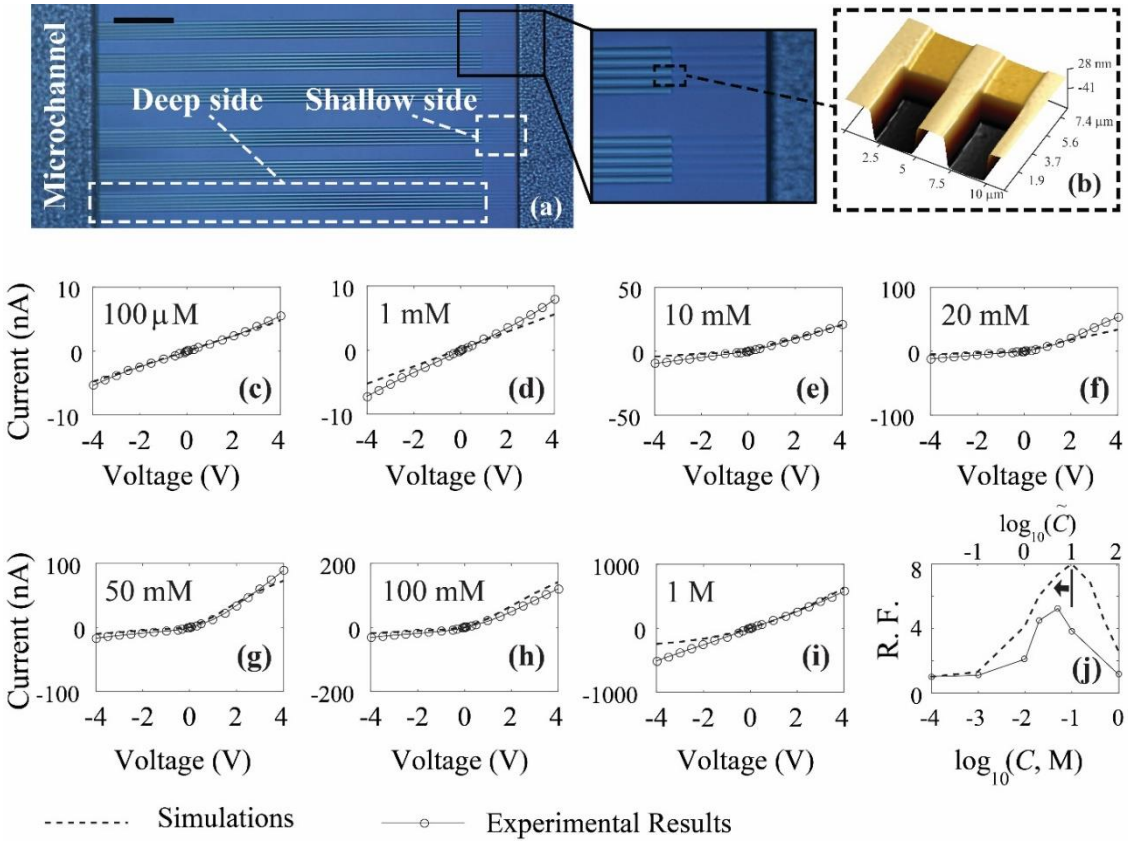

Figure 3.5: (**a**) Microscope and (**b**) AFM images of a stepped channel used for experiment. The scale bar in **a** is 100 μm. (**c-i**) The measured $i - v$ curves (solid lines) for 100 μM, 1 mM, 10 mM, 20 mM, 50 mM, 100 mM, and 1M KCl concentrations compared against theoretical results. (dashed lines) (**j**) Experimental and theoretical rectification factor versus concentration at 4 V.

3.4.2 Measurements

The voltage-current curves for seven concentrations ranging from $100\,\mu M$ to $1\,M$ is shown in Figures 3.5.c thru 3.5.i. In each plot the solid line is the experimental results and the dashed line is the theoretical prediction. In order to compare the experimental results with theory, in particular at higher concentrations, it is important to account for decrease in the ionic mobility at higher concentrations. For full dissociated ions such as K^+ and Cl^-, ionic mobility in a bulk solution can be expressed as (Baldessari 2008)

$$\mu = \frac{1}{1 + \frac{c_1 z\sqrt{I_z}}{1 + c_2 a\sqrt{I_z}}}\mu_\infty \tag{3.6}$$

where $I_z = \frac{1}{2}\sum_j {z_j}^2 n_j$ is the ionic strength, and $c_1 = 1.825\,(\varepsilon T)^{-3/2}$ and $c_2 = 50.3(\varepsilon T)^{-3/2}$ depend on the absolute temperature and the dielectric constant of the solvent. For water at 25 ℃ , $c_1 = 0.508\,M^{-1/2}$ and $c_2 = 3.29\,nm^{-1}\ M^{-1/2}$. Finally, a is an adjustable parameter related to the ion size which for K^+ and Cl^- is equal to a ≈ 0.3 nm. Mobilities of K^+ and Cl^- in infinite-dilution are $\mu_{\infty,K^+} = 7.6 \times 10^{-8}\,m^2V^{-1}s^{-1}$and $\mu_{\infty,Cl^-} = 7.91 \times 10^{-8}\,m^2V^{-1}s^{-1}$, respectively. According to this equation the ionic mobility of KCl at 1M is about 66% of that at infinite-dilution.

The experimental results are in agreement with the theoretical results, although there are some discrepancies observed, too. The rectification factor as a function of concentration illustrates a trend expected from the model (Figure 3.5.j) with a peak rectification at 50 mM. Nevertheless the theoretical peak rectification has shifted to higher values of normalized concentration compared with the experiments, suggesting that surface charge has been overestimated. To obtain the surface charge the theoretical $i - v$ curve was fit to the 100 μM results and the value of $\sigma = -50\ mC/m^2$ was obtained. While this fairly high measured surface charge is consistent with previous measurements in similar nanochannel (Stein *et al.* 2004), this value can only serve as an upper limit for the surface charge. In fact, when fitting a curve to the 100 μM results, we ignored the electroosmosis effect which can be as important as the electrophoretic term at low concentrations (Daiguji *et al.* 2004; Haywood *et al.* 2014). This results in overestimation of the surface charge which in turn

would shift the rectification factor curve in Figure 3.5.j to the right. In fact, this design of nanofluidic diode enables us to estimate the value of surface charge without relying on $i - v$ curves at low concentrations. Based on the peak rectification location (C_{max}) the surface charge cannot be higher than $\sim -20\ mC/m^2$. At high electrolyte concentrations (50 mM, 100 mM, and 1 M) where the electroosmosis becomes negligible compared with the electrophoretic term, reducing the surface charge to $-20\ mC/m^2$ in the 1D model better predicts the experimental results; however it causes significant deviation from experiments at lower concentrations (Results not shown). It's noticed that the experimental rectification factor is smaller than the theoretical values. We believe this is also due to the electroosmosis effect which reduces the rectification mainly by increasing the absolute value of reverse bias current, although it increases the forward bias current too. Another shortcoming of the present analysis is the assumption of constant surface charge throughout the entire nanochannel and for different concentrations. It's known that this assumption does not reflect the complete physics and a more sophisticated model accounting for dissociation of SiOH groups better predicts the experimental results (Andersen *et al.* 2011; Behrens and Grier 2001; Smeets *et al.* 2006). However, implementation of this model in our simulation is not easily possible and makes the system of equation very complicated, and hence is avoided. Nonetheless, the constant surface charge assumption allowed us to reliably predict the experimental results.

3.5 Conclusions

In summary, we presented a new method for ionic current rectification in nanofluidic systems. The advantages of this method over previously reported methods are (*i*) it does not require any surface modification and thus is very stable and easy to work with, (*ii*) it can very easily be integrated with other fluidic elements in 2D lab-on-a-chip fluidic circuits. Additionally, design of this nanofluidic diodes is facilitated by knowledge of the nondimensional concentration that dictates its rectification behavior. It was observed that the rectification factor does not monotonically increase by decreasing the electrolyte concentration, rather it reaches a peak in midrange concentration. The location of this peak is determined by the surface charge density and the nanochannel dimensions, and hence this type of nanofluidic diode can be configured to yield high rectifications at high electrolyte concentrations. Future studies will focus on electroosmotic flow in stepped nanochannels and its effect on the electrokinetics in such systems**.**

CHAPTER 4: Enzymatic Hydrolysis of Polypeptides in a Nanofluidic Channel

Label-free detection of enzymes using nanofluidic channels requires enzymes to diffuse into the nanochannel and react with the substrate already immobilized on the walls of the nanochannel. In this paper, enzymatic hydrolysis of polypeptides in a nanochannel is numerically studied using a 1-D model that considers various reaction kinetics, enzyme diffusion and non-specific adsorption. It is observed that two types of reaction fronts are formed inside the nanochannel and the reaction fronts advance linearly with time once they are fully developed. Such constant reaction rates can be predicted by an analytical model. The numerical simulations are validated against experimental results of the trypsin-polylysine reaction in nanochannels and a good agreement is observed. A further parametric study shows that below a certain channel length, enzymatic reactions in nanochannels are significantly faster than those on a plain surface. This enhancement stems from the reduced diffusion length, and reactions with small catalytic rate constant**,** low enzyme diffusivity and large grafting density at low enzyme concentration would benefit the most in nanochannels. This study deepens our understandings of enzymatic reactions in nanoscale-confined space and can guide the development of a fast-response, label-free enzyme sensor based on nanochannels.

4.1 Introduction

Level of certain proteolytic enzymes in blood may reveal state of diseases such as heart attack and cancer and thus can be an important indicator for clinical diagnosis (Giannini *et*

al. 2005; Puente *et al.* 2003; Raja *et al.* 2011; Stefanini 1985). Current enzyme assays for characterizing enzymatic activity use fluorogenic/chromogenic labeled substrates (Manafi *et al.* 1991; Van Noorden 2010), which are expensive and may cause unexpected kinetics change due to modification. Compared with these classic labeling methods, label-free techniques are capable of providing rapid enzyme assay without labeling the molecules of interest. To date, several label-free techniques including field-effect transistors (Dzyadevych *et al.* 2003; Kharitonov *et al.* 2000; Makowski and Ivanisevic 2011; Neff *et al.* 2007; Yoon *et al.* 2008), quartz crystal microbalance (Liss *et al.* 2002; Muratsugu *et al.* 1993), and surface plasmon resonance (Anker *et al.* 2008; Lee *et al.* 2005; Malmqvist 1993; Nelson *et al.* 2001) have been proposed to utilize surface reactions for label-free detection of enzymatic activities. Along with development of these techniques, binding and reaction kinetics on surface have been studied using both experimental and theoretical approaches (Fang *et al.* 2005; Karlsson *et al.* 1994; Lee *et al.* 2005; Schuck and Minton 1996). It is found that analyte (enzyme in this scenario) diffusion is actually the limiting factor for such surface reaction based detection techniques, especially for samples with low enzyme concentrations, because diffusion results in the formation of a large depletion zone (ranging from μm to mm or up to cm). One possible way to resolve the diffusion limitation and thus achieving fast detection is to restrain the substrates and enzymes in a nanoscale confinement where the diffusion-induced depletion zone is eliminated. This idea has actually been widely implemented for fast protein analysis, where enzymes are immobilized into a nanoporous material and accelerated enzymatic hydrolysis occurs due to confinement once low concentration analytes (protein substrates in this case) diffuse into

this porous material (Bi *et al.* 2009; Tischer and Wedekind 1999). However, despite its tremendous success in protein analysis, nanoscale confinement has not been fully utilized for fast-response and label-free enzyme detection.

Nanofluidic channels, another type of nanoscale confinement, can simultaneously serve as the reaction container and the signal transducer for label-free detection of surface reactions, as long as such reactions can lead to a change in surface charge density and/or channel height (Karnik *et al.* 2005a; Orosco *et al.* 2009; Schoch *et al.* 2007). However, it is not well understood at this point how enzymatic reactions, in the case of immobilized substrates in a nanoscale confinement differ from similar reactions on a plain surface and whether such confinement could really lead to a fast reaction. Herein, we answer these questions by investigating enzymatic hydrolysis in nanofluidic channels using a comprehensive numerical simulation. The focus of this study is enzymatic hydrolysis of polypeptide chains with many cleavage sites, yet the results are applicable to the simple substrates too. Two reaction models, namely random reaction and ordered reaction models, corresponding to the fastest and slowest enzymatic hydrolysis reactions are proposed and their reaction rates are studied as a function of enzyme diffusivity, channel height, substrate grafting density and enzyme kinetics' constants. Theoretical results obtained from these models are validated against experimental results and quantitatively compared with reaction on a plane surface. A regime of parameters is identified in which nanochannel exhibits a faster reaction compared to the surface reaction.

4.2 Enzyme-substrate kinetics: governing equations

The schematic of our simulation model is shown in Figure 4.1. Enzymes diffuse towards a nanochannel center from both ends of the nanochannel and hydrolyze polypeptide substrates which are already immobilized on the walls. Since each substrate has many susceptible bonds that enzymes could cleave, one has to think how enzymes act on these susceptible bonds. There are two basic types of enzyme actions on protein/polypeptide substrates, namely endo- and exoproteolytic reactions. In exoproteolytic reactions, proteolytic enzymes can only react with the terminal peptide bonds of a polypeptide chain. However, in endoprotelytic reactions, enzymes can react with all susceptible bonds. Based on these two basic reaction mechanisms, several reaction models, including zipper model, one-by-one model, and sequential model have been proposed (Bi *et al.* 2009; Srividhya and Schnell 2006) to simulate enzymatic hydrolysis of polypeptides in solution or on surface. The zipper mechanism assumes an enzyme binds to the terminal peptide bond of a chain, and keeps cleaving the bonds in order and does not dissociate from the substrate until all cleavable bonds are digested. The one-by-one mechanism assumes an enzyme randomly chooses a bond whose cleavage gives rise to a low MW peptide (final product) and a shorter substrate chain. After this cleavage enzyme dissociates from the substrate. This model also assumes that only one bond at a time is available to enzymes. Sequential model is similar to one-by-one model, except that after each cleavage two shorter substrate chains are produced (instead of one final product and one shorter substrate chain) each of which can be further hydrolyzed until final products are produced.

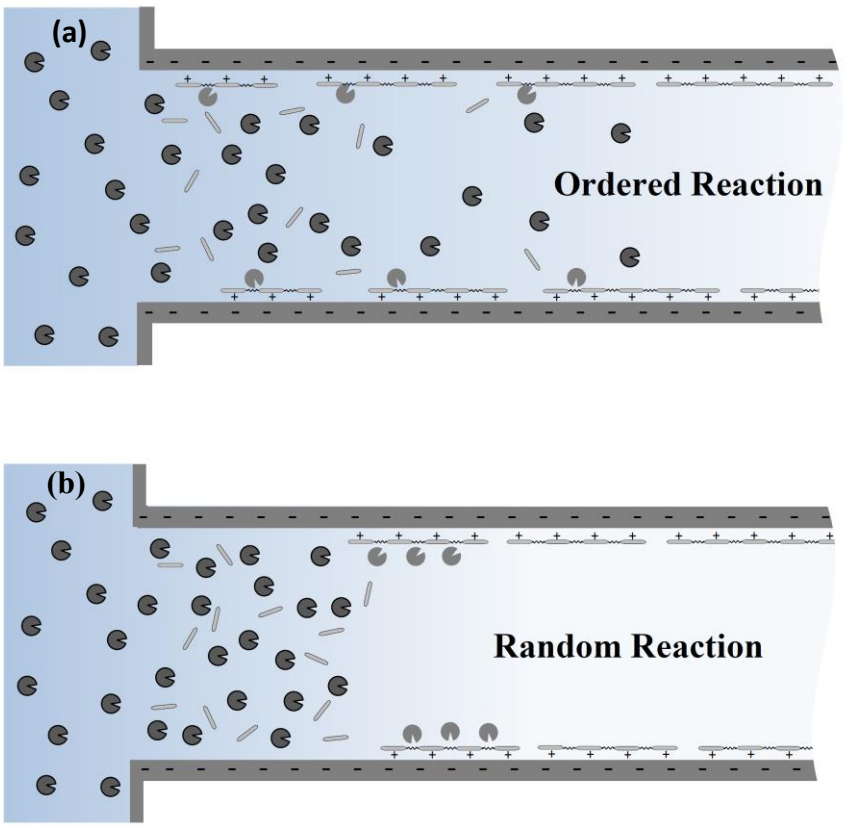

Figure 4.1: Schematic of the problem. Top (bottom) side of the nanochannel illustrates an ordered (random) reaction. In an ordered reaction the susceptible bonds are cleft in order and only one enzyme can bind to a chain at a moment, whereas in random reaction multiple enzymes can attack a chain.

In this paper, two slightly different models are proposed, namely "ordered" and "random" reaction models. The ordered reaction model is quite similar to the zipper model, except that in this model enzyme after each cleavage can dissociate from the substrate. In this model, only one enzyme molecule can act on the substrate at a time, and the cleavable bonds are digested from one end in order. After each cleavage, enzyme is able to dissociate from the substrate before it binds to the next susceptible bond. This reaction (shown in Figure 4.1.a) is expected to give the slowest reaction rate for such a reaction compared to other mechanisms and mimics an exoproteolytic reaction. By contrast, the random reaction

model (Figure 4.1.b) assumes that all the cleavable bonds of a substrate are available to enzymes. These susceptible bonds may simultaneously be cleft by multiple enzymes and each cleavage yields a final product. This mechanism mimics an endoproteolytic reaction and is believed to be the fastest possible reaction. This "multiple attack possibility" distinguishes the random reaction model from the "one-by-one" and the "sequential" model and represents the case that an immobilized polypeptide chain spreads on the surface in a 2-D form due to its multi-interactions with the surface instead of its 3-D compact structure in solution. Since the random and ordered models in this work consider possible enzyme dissociation from the substrate after cleaving a bond and also consider the scenario where multiple enzymes may attack the same substrate simultaneously, they are more appropriate to describe enzymatic proteolytic reactions in nanochannels compared with the previous models. Furthermore, these two models represent two extremes of all such reactions and thus can provide us a better understanding for a particular reaction.

4.2.1 Random reaction in nanochannel

Suppose complete hydrolysis of a chain gives rise to m identical products. In order to make all cleavable bonds available to enzymes, one can think of one substrate chain as m small segments of substrate to each of which enzymes can bind. This assumption allows the enzymes to randomly react with the bonds. As a result, kinetics of the enzyme-substrate reaction follows the kinetics of simple substrate with a single cleavable bond and can be shown in the following form

$$E + S \underset{k_d}{\overset{k_a}{\rightleftarrows}} ES \xrightarrow{k_{cat}} E + P \tag{4.1}$$

where E, S, ES, and P represent enzyme, substrate, enzyme-substrate complex and final product, respectively. Furthermore, k_a is the association rate constant, k_d is the dissociation rate constant, and finally k_{cat} is the catalytic rate constant. Here**,** the differences between amino acid residues are neglected and as a result the reaction rates (k_a, k_d, and k_{cat}) are assumed to be similar for all reaction steps, which is not necessarily valid in practice. A set of three ordinary differential equations and one algebraic equation governs this kinetics:

$$\frac{\partial [E]}{\partial t} = \frac{Q}{A}\left\{-k_a[S][E] + \left(k_d + k_{cat}\right)[ES]\right\} + D\frac{\partial^2 [E]}{\partial x^2} \tag{4.2.a}$$

$$\frac{d[ES]}{dt} = k_a[S][E] - \left(k_d + k_{cat}\right)[ES] \tag{4.2.b}$$

$$\frac{d[P]}{dt} = k_{cat}[ES] \tag{4.2.c}$$

$$[S] = m[S_n] - [ES] - [P] \tag{4.2.d}$$

where $[E]$ is the enzyme concentration, $[S]$ is the surface density of the substrate chains with $[S_n]$ being its initial value, $[ES]$ is the surface density of the enzyme-substrate complex, $[P]$ is the surface density of product, D is enzyme diffusivity, Q is the perimeter of the channel and A is the channel's cross sectional area. Last term in the first equation accounts for the diffusion of the enzyme to the channel. This system of four equations and four unknowns is closed and can be solved by applying appropriate initial and boundary conditions:

$$[S](x,0)=m[S_n],\ [ES](x,0)=0,\quad [P](x,0)=0,\quad [E](x,0)=0$$
$$[E](0,t)=[E_0],\quad \frac{\partial[E]}{\partial x}(l/2,t)=0 \tag{4.2.e}$$

where l is the channel length.

4.2.2 Ordered reaction in nanochannel

Let's again assume that complete hydrolysis of a chain produces m identical products. Then, an ordered reaction may be represented as:

$$\begin{aligned}
&E + S_n \underset{k_d}{\overset{k_a}{\rightleftarrows}} ES_n \xrightarrow{k_{cat}} E + S_{n-\frac{n}{m}} + P \\
&E + S_{n-\frac{n}{m}} \underset{k_d}{\overset{k_a}{\rightleftarrows}} ES_{n-\frac{n}{m}} \xrightarrow{k_{cat}} E + S_{n-\frac{2n}{m}} + P \\
&\quad\vdots \\
&E + S_{\frac{2n}{m}} \underset{k_d}{\overset{k_a}{\rightleftarrows}} ES_{\frac{2n}{m}} \xrightarrow{k_{cat}} E + 2P
\end{aligned} \tag{4.3}$$

Similar to the random reaction, rate laws can be written for each step in the reaction. This gives rise to a system of $2m$ equations whose solution for large m's is computationally intensive. Instead, adding up the governing equations at each step results in equations (4.4.a), (4.4.b), and (4.4.c):

$$\frac{\partial[E]}{\partial t}=\frac{Q}{A}\left\{-k_a[E][S]+\left(k_d+k_{cat}\right)[ES]\right\}+D\frac{\partial^2[E]}{\partial x^2} \tag{4.4.a}$$

$$\frac{d[ES]}{dt}=k_a[E][S]-\left(k_d+k_{cat}\right)[ES] \tag{4.4.b}$$

$$\frac{d[P]}{dt}=k_{cat}[ES] \tag{4.4.c}$$

in which $[ES] = \sum_{i=0}^{m-2} [ES_{n-in/m}]$, and $[S] = \sum_{i=0}^{m-2} [S_{n-in/m}]$. It's worth mentioning that final cleavage in equation (4.3) creates 2 products, one of which is ignored in equation (4.4) for the sake of simplicity. These equations are similar to the random reaction equations (4.2.a, 4.2.b, and 4.2.c), except that here $[S]$ and $[ES]$ have different interpretations. One last equation describing substrate density is required to close the system of equations. Assuming the substrate concentration does not change until last bonds are cleft, one can write

$$[S] = \begin{cases} [S_n] - [ES]; & \text{If } [P] < (m\text{-}1)[S_n] \\ [S_n] - [ES] - \{[P] - (m-1)[S_n]\}; & \text{otherwise} \end{cases} \quad (4.4.d)$$

Boundary conditions of this system of equation is similar to equation 4.2.e, except for $[S](x,0) = [S_n]$. The accuracy of these simplifications was verified by solving the complete system of $2m$ equations in a nanochannel for several cases and comparing the results against the results obtained from equations (4.4.a) thru (4.4.d). Results (not presented) suggest that the aforementioned assumptions perfectly reflect the intended physics, and the reaction progress, as well as the concentration profiles along the nanochannel at different times for two cases are in excellent agreement.

4.2.3 Reaction on a surface

Reaction on a surface may be considered as a boundary condition for the differential equation governing the diffusion of enzymes. With y being the coordinate normal to the surface, and surface located at $y = 0$ one can write:

$$\frac{\partial [E]}{\partial t} = D\frac{\partial^2 [E]}{\partial y^2} \tag{4.5.a}$$

$$\left.\frac{\partial [E]}{\partial y}\right|_{y=0} = \frac{-1}{D}\left(-k_a[S][E] + \left(k_d + k_{cat}\right)[ES]\right) \tag{4.5.b}$$

$$\left.\frac{\partial [E]}{\partial y}\right|_{y=\infty} = 0 \tag{4.5.c}$$

This equation can be solved along with equations (4.2.b) thru (4.2.d) or (4.4.b) thru (4.4.d), depending whether modeling random or ordered reaction is desired.

4.2.4 Non-specific adsorption effect

Enzymes confined in a nanochannel are susceptible to non-specific adsorption to the surfaces which has an unfavorable effect on the reaction rate. This non-specific adsorption can schematically be shown as

$$E + N \underset{k_{d,ns}}{\overset{k_{a,ns}}{\rightleftarrows}} EN \tag{4.6}$$

in which $[N]$ is the density of the vacant surface sites, and $[EN]$ is the surface density of the enzymes non-specifically adsorbed to the surface. The governing equation of $[EN]$ can be written as

$$\frac{d[EN]}{dt} = k_{a,ns}[E]\left([EN]_{\max}\eta - [EN]\right) - k_{d,ns}[EN] \tag{4.7}$$

In this equation, $k_{a,ns}$ and $k_{d,ns}$ are rate constants associated with the non-specific adsorption, and η which is the ratio of the vacant surface sites to total surface sites, is given by

$$\eta = \frac{[P]}{m[S_n]} \tag{4.8}$$

In the presence of non-specific adsorption, the governing equation of the enzyme concentration also has to be corrected as:

$$\frac{\partial[E]}{\partial t} = -\frac{Q}{A}\left(\frac{\partial[ES]}{\partial t} + \frac{\partial[EN]}{\partial t}\right) + D\frac{\partial^2[E]}{\partial x^2} \tag{4.9}$$

The required background for modeling reaction in a nanofluidic channel and reaction on a surface is now complete. Next, numerical analyses are presented.

4.3 Numerical results

Parameters used in this study were obtained from the reaction of poly-l-lysine (PLL) with the serine endopeptidase trypsin. This reaction has been extensively studied and the relative rates of hydrolysis of several susceptible bonds have been addressed (Waley and Watson 1953). It has been shown that in the reaction of PLL with trypsin peptide bonds adjacent to a carboxyl or amino group are not split, and therefore almost no monolysine is formed (Waley and Watson 1953). Although this reaction mainly produces di- and tri-lysine, in the current study for the sake of simplicity it is assumed that the only product is di-lysine, and as a result $m = \kappa/2$, where κ is the average degree of polymerization of PLL chains. In order to perform simulations, the rate constants and the substrate surface density have to be determined: the reported value for k_M is 400 nM (Neff *et al.* 2007), and the value of k_{cat} from figure 2 in (Neff *et al.* 2007) may be calculated as $k_{cat} = 13.16\ s^{-1}$; also it is assumed that k_d is equal to k_{cat}. Assuming the area occupied by a monomer (lysine) is

0.23 nm (Colville *et al.* 2009; Neff *et al.* 2007) and only a single layer of substrate is immobilized at the surface, the surface density of substrate is calculated. The implicit assumption here is that long polypeptides take the Pancake structure at the surface (versus Mushroom or Brush morphologies). This is consistent with the fact that a positively charged polylysine chain can minimize its energy state by adsorbing on the negatively charges silica surface and hence is likely to take the "Pancake" form (Liu and Zhang 2013). Finally, diffusion coefficient of trypsin is $D = 9.6 \times 10^{-9}$ (m^2/sec), and PLL molecular weight is 70–150 kDa. The reaction has been modeled in a nanochannel 120 μm long, 2 μm wide and 50 nm high.

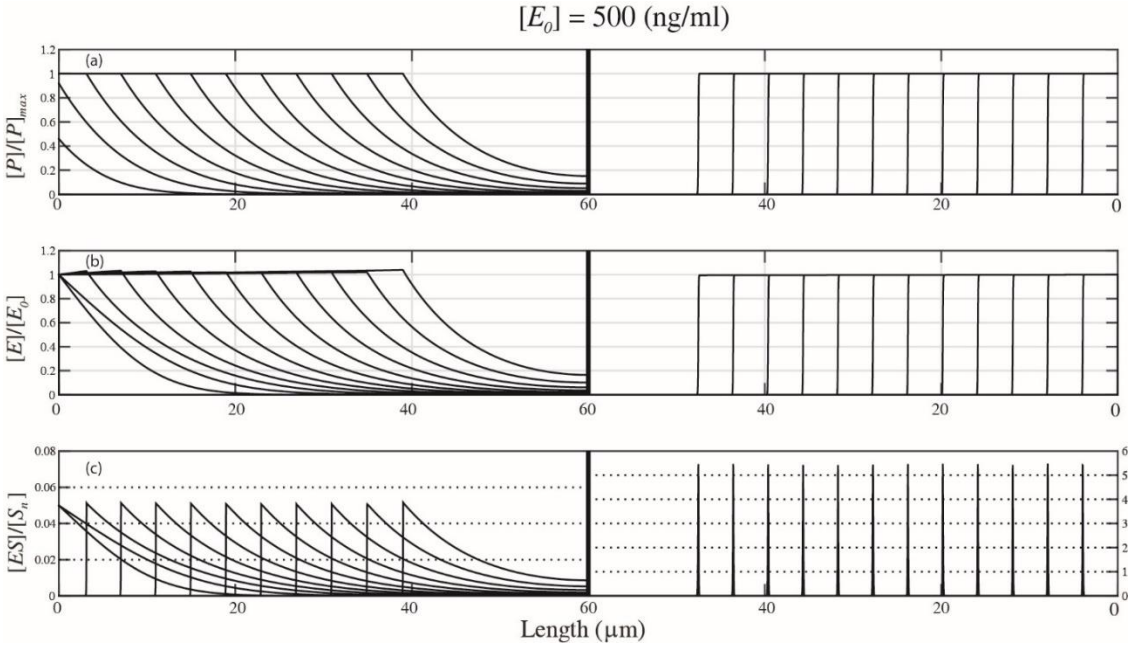

Figure 4.2: Concentration profiles along the nanochannel for the enzyme concentration of 500 ng/ml. Left (right) figures demonstrate ordered (random) reaction. (**a**) Product concentration profile (**b**) enzyme concentration profile (**c**) enzyme-substrate complex concentration profile.

Effect of two proposed reaction mechanisms on the concentration/surface density profiles along the nanochannel is investigated in Figure 4.2. The normalized surface density of product, enzyme concentration and the enzyme-substrate complex density along the nanochannel are respectively plotted in Figures 4.2.a, 4.2.b, and 4.2.c, after 5,10,…,60 minutes. Enzyme concentration in the two reservoirs supplying enzymes to the nanochannel is 500 ng/ml, and the non-specific adsorption is not accounted for in this case. It can be observed that for both reactions, once reaction fronts are developed, they preserve their shapes during the reaction and propagate along the nanochannel with a constant speed. Similar reaction fronts for fully reaction-limited and fully diffusion-limited transports in two dimensional microfluidic channels have been previously reported (Gervais and Jensen 2006). Unlike random reaction which immediately renders a sharp reaction front, in the ordered reaction no sharp front is established, and instead a much wider reaction front gradually occurs after a relatively long developing time. This front shape difference can be better understood by looking at the normalized $[ES]$ profile for each case. While both reactions comprise a sharp peak in their $[ES]$ profiles, unlike the ordered reaction, $[ES]$ in random reaction is only localized at the reaction front and the peak value of $[ES]$ in random reaction is 2 orders of magnitude larger than that of ordered reaction. This high local $[ES]$ results in the sharp reaction front. It can be seen in this figure that for random reaction $[ES]_{max}$ occurs at $[E](x) = [E_0]/2$, and for the ordered reaction it occurs at $[E](x) = [E_0]$. Accordingly, the following relations for the peak value of $[ES]$ are derived:

$$\frac{\left[ES\right]_{random,\max}}{\left[S_n\right]} = \frac{m\left[E_0\right]}{4k_M + 2\left[E_0\right]} \tag{4.10}$$

$$\frac{[ES]_{ordered,\max}}{[S_n]} = \frac{[E_0]}{k_M + [E_0]} \tag{4.11}$$

The accuracy of these relations has been numerically investigated and confirmed at different enzyme concentrations. Finally, comparison of Figures 2.a and 2.b reveals that for both reaction mechanisms, the product density maintains the same profile as the enzyme concentration. Later, it will be mathematically shown that this is a requisite for a self-similar propagation.

Figure 4.2 for the random reaction demonstrates that concentration profiles preserve their shapes and travel with a constant speed (V). A parametric study is performed in Figure 4.3 to determine the dependence of this speed on enzyme concentration, enzyme diffusivity, substrate density, nanochannel dimensions, and the rate constants. Figure 4.3.a illustrates the reaction progress after 5, 10, 15, and 20 minutes as a function of $\sqrt{[E_0]}$. Reaction progress is defined as the ratio of the amount of di-lysine (product) produced in the nanochannel to the amount of di-lysine at the end of reaction which is simply proportional to the front speed. Calculations have been performed for five values of reservoir enzyme concentration (5, 50, 200, 500, and 5000 ng/ml), and results clearly exhibit a linear dependence. In Figure 4.3.b dependence of the reaction progress on the channel height, enzyme diffusivity, substrate surface density, and the catalytic rate constant has been investigated. A nondimensional parameter, ξ, is defined which can take any of $\sqrt{D/\tilde{D}}$, $\sqrt{k_{cat}/\tilde{k}_{cat}}$, $\sqrt{[\tilde{S}_n]/[S_n]}$, and $\sqrt{h/\tilde{h}}$, and allows us to concisely present the results. Here, h is equal to $2A/Q$ which for small channel heights is equal to the channel height. Also, the tilde quantities refer to the reference values of the corresponding variable. ξ was varied

for each of four aforementioned parameters at enzyme concentrations of 5, 50, 500, and 5000 ng/ml, and reaction progress after 10 minutes was calculated. It is observed that results of all four cases are quite alike with a negligible difference much smaller than the marker size. In fact, Figure 4.3.b illustrate that the reaction progress is a linear function of $\sqrt{h}$, $\sqrt{D}$, $\sqrt{k_{cat}}$, and $\sqrt{1/[S_n]}$, and along with Figure 4.3.a suggests the front speed V is proportional to $\sqrt{h\ D\ k_{cat}[E_0]/[S_n]}$. Also, it was observed that k_a and k_d don't change the front speed appreciably. The clear dependence of the front speed on $[E_0]$, h, D, k_{cat} and $[S_n]$ indicates that an analytical formula for the reaction front speed can be derived. For a self-similar propagation under quasi-static assumption ($\frac{\partial[E]}{\partial t} \cong 0$), equations 4.2.a and 4.2.c yield:

$$\frac{d[ES]}{dt} = \frac{A}{Q} D \frac{\partial^2[E]}{\partial x^2} = -V \frac{d[ES]}{dx} \tag{4.12.a}$$

$$\frac{d[P]}{dt} = k_{cat}[ES] = -V \frac{d[P]}{dx} \tag{4.12.b}$$

Differentiating equation 4.12.b with respect to x and combining with 4.12.a yields a second order differential equation whose solution, by virtue of the fact that V is not a function of x and t, is:

$$\frac{[P]}{m[S_n]} = \frac{[E]}{[E_0]} \tag{4.13}$$

$$V = \sqrt{\frac{h}{2} D k_{cat} \frac{[E_0]}{m[S_n]}} \tag{4.14}$$

Equation (4.13) elucidates the resemblance of the normalized enzyme concentration profile and the normalized product surface density profile (Figure 4.2), and equation (4.14) presents an analytical solution for the reaction front speed. Further examination of equation (4.14) is done in Figure 4.3.c, where the location of the reaction front calculated by this formula is compared against the results obtained from full numerical analysis and perfect agreement between the numerical and analytical results is observed. Here, reaction front location is defined as the point where the product concentration reaches the 90% of its final value.

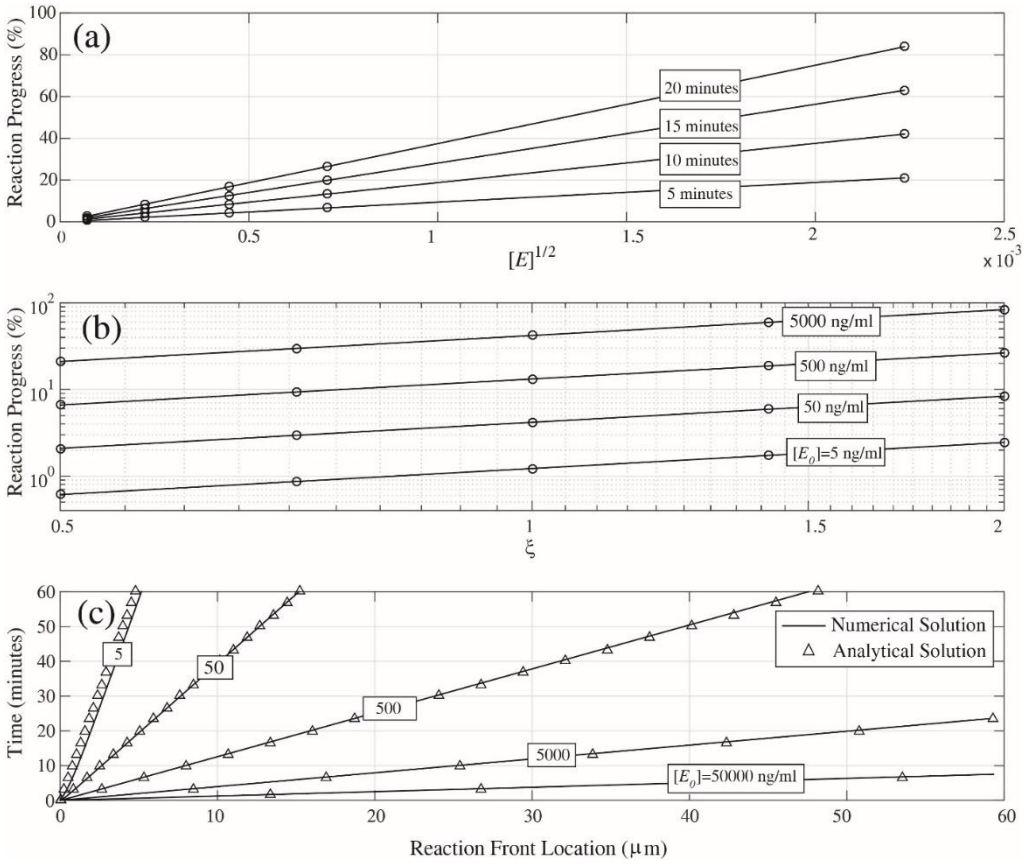

Figure 4.3: (**a**) Dependence of random reaction progress on enzyme concentration after 5, 10, 15, and 20 minutes (**b**) dependence of random reaction progress on nondimensional diffusivity, substrate density, channel height, or catalytic rate constant, for different enzyme concentration after 10 minutes **(c**) random reaction front location versus time for different enzyme concentrations.

As it was observed in Figure 4.2, in case of an ordered reaction no sharp front is established. Further investigation of the front speed for an ordered reaction requires the reaction be modeled in a semi-infinite channel to avoid the reaction fronts coming from two sides to merge**.** Figure 4.4.a exhibits the location of the reaction front versus time for the ordered reaction obtained from numerical analysis and compares it with the results predicted by equation (4.14). Low enzyme concentration curves are associated with intercepts which indicate how long it takes for the front to be developed. It's interesting to note that after reaction front is developed, it moves with the speed predicted by equation (4.14). In fact, this figure shows that although random and ordered mechanisms reflect two extreme rates in hydrolysis of polypeptides, their final speeds are the same which indicates the reaction progress is dictated by the diffusion of enzymes. At higher enzyme concentration, reaction front is rapidly developed and hence a good agreement between the analytical solution and the numerical results is established. Development of reaction front can be further investigated by monitoring the evolution of the front width during a reaction. Let's define the front width as the distance over which the product concentration decreases from 90% to 10% of its final value. In Figure 4.4.b, front widths in a semi-infinite channel for different enzyme concentrations are plotted as a function of time. It can be seen that after a certain period of initial development, there is a break point after which reaction front maintains an approximately constant width. Data presented in this figure can be cast in the form of Figure 4.4.c, to reveal the front width is approximately a linear function of $1/\sqrt{[E_o]}$. Further numerical examination of the front width in the parameter space is presented in Figure 4.4.d by varying $\sqrt{h/\tilde{h}}$, $\sqrt{D/\tilde{D}}$ and $\sqrt{[\tilde{S}_n]/[S_n]}$ between 0.5 and 2 ($[E_0] = 500$

ng/ml). The observed linear dependence of front width on β (which can take any of the mentioned quantities) confirms that front width is proportional to $L \propto \sqrt{h\,D\,/[S_n][E_0]}$ and suggests that an analytical solution should exist for it. Starting from equation (4.12b) while keeping in mind that from Figure 4.2 normalized values of $[P]$ and $[ES]$ have similar profiles ($[ES] \approx \frac{[ES]_{max}}{[P]_{max}}[P]$), yields:

$$\frac{d[P]}{dx} = -\left(\frac{k_{cat}}{V}\frac{[ES]_{\max}}{[P]_{\max}}\right)[P]$$

which has a solution in the form of $\frac{[P](x)}{[P]_{max}} = e^{-\frac{x}{\lambda}}$, consistent with our observation in Figure 4.2.a. Substituting for $[ES]_{max}$ and V from equation (4.11) and (4.14) for λ yields:

$$\lambda = \left(k_M + [E_0]\right)\sqrt{\frac{mhD}{2k_{cat}[S_n][E_0]}} \qquad (4.15)$$

The front width should be a factor of λ and the investigated $1/\sqrt{[E_o]}$ dependence only holds when $[E_o] \ll k_M$. It can be seen from Figure 4.4.c that reaction front width can be accurately estimated as $L \cong 1.5\,\lambda$. Needless to say, a similar relation can be derived for random reactions, too. However, even at enzyme concentration of 50 ng/ml (which has the largest front width among studied concentrations) front width of random reaction only can each reach 0.24 μm.

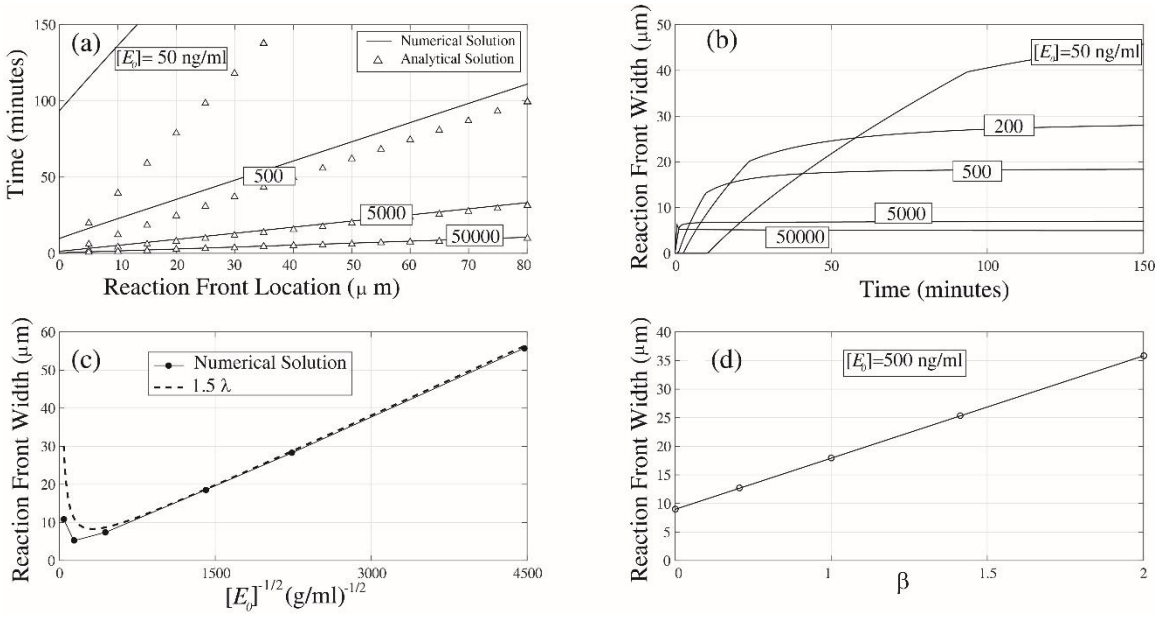

Figure 4.4: (**a**) Reaction front location versus time for different enzyme concentrations, (**b**) Front width vs. time for different enzyme concentrations, (**c**) Dependence of front width on enzyme concentration, (**d**) Dependence of front width on nondimensional channel height, substrate surface density, and diffusivity.

Despite the fact that final reaction front speed for random and ordered reactions are identical, a parametric study can shed light on the early stage of an ordered reaction, when no front is developed yet. Four lines in Figure 4.5.a show the ordered reaction's progress as a function of $\sqrt{[E_o]}$ after 5, 10, 15, and 20 minutes. These results indicate that at low enzyme concentrations reaction progress is proportional to $[E_o]$, while at higher concentrations it is proportional to $\sqrt{[E_o]}$ (same as in random reaction). This is consistent with our observation that at low enzyme concentrations numerical results of an ordered reaction deviate from analytical results. In Figures 5.b dependence of reaction progress on substrate density, diffusion coefficient, catalytic rate constant, and channel height are presented. Similar to Figure 4.3.b, the reaction progress after 20 minutes is plotted as a function of the nondimensional parameter ξ. In this Figure, the solid lines are associated

with $\sqrt{h/\tilde{h}}$, $\sqrt{D/\tilde{D}}$, and $\sqrt{[\tilde{S}_n]/[S_n]}$, and dashed lines represent the results of $\sqrt{k_{cat}/\tilde{k}_{cat}}$. Interestingly, reaction progress is still a linear function of $\sqrt{h}$, $\sqrt{D}$, and $\sqrt{1/[S_n]}$. However, its dependence on $\sqrt{k_{cat}}$ is more complicated, and only at high enzyme concentrations, reaction progress is approximately a linear function of $\sqrt{k_{cat}}$. Hence, at early stage of an ordered reaction at low enzyme concentrations, reaction progress is proportional to:

$$\textit{Reaction Progress} \propto [E_0]\sqrt{h\,D\,/[S_n]}\,f(k_{cat}) \tag{4.16}$$

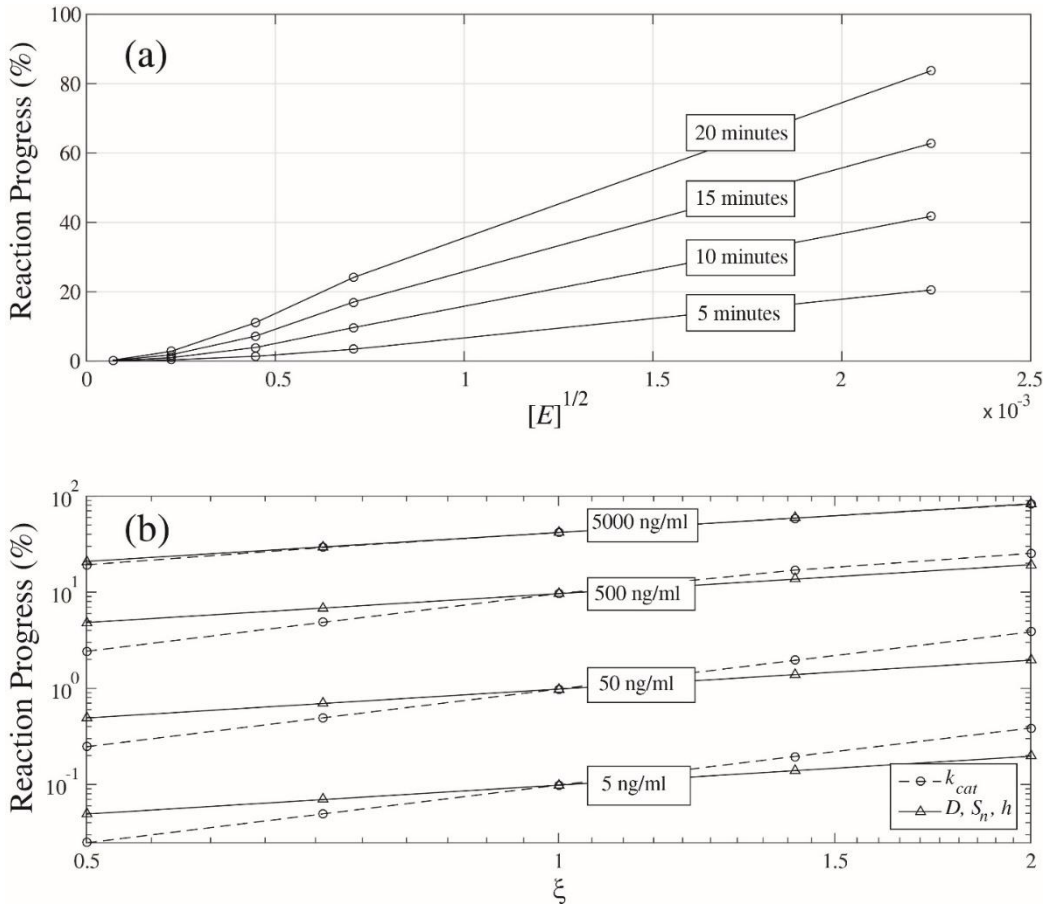

Figure 4.5: Dependence of the ordered reaction progress on (**a**) enzyme concentration after 5, 10, 15, and 20 minutes, (**b**) nondimensional channel height, diffusivity, substrate density, and catalytic rate constant, after 10 minutes.

Non-specific adsorption of enzymes can be a limiting factor for the reaction, and it is worthwhile studying how non-specific adsorption alters the reaction progress. The non-specific adsorption and desorption rate constants for the current simulation (adsorption of trypsin to a glass surface) can be estimated from available data in the literature (Löfroth and Augenstein 1967). Defining $k_{M,ns} = k_{d,ns}/ k_{a,ns}$, from figure 2 in (Löfroth and Augenstein 1967) the values of $k_{M,ns}$ and $[EN]_{max}$ are estimated as: $k_{M,ns} = 80 \times 10^{-6}\ M$ and $[EN]_{max} = 18 \times 10^{-3}\ gr/m^2$. Also it's further assumed $k_{a,ns} = k_a$. Figure 4.6 compares the reaction progress of random and ordered reactions versus times, with/without considering the non-specific adsorption at enzyme concentrations of 50, 500, and 5000 ng/ml. At low enzyme concentrations, non-specific adsorption has a negligible effect, whereas at higher concentrations it appreciably slows the reaction down. For example for the case of 5000 ng/ml, non-specific adsorption causes the reaction to take almost twice longer to finish. Without considering non-specific adsorption random mechanism always exhibits a faster reaction compared with ordered reaction, even though at high concentrations results are very close. However, in the presence of non-specific adsorption, ordered reaction may become even faster.

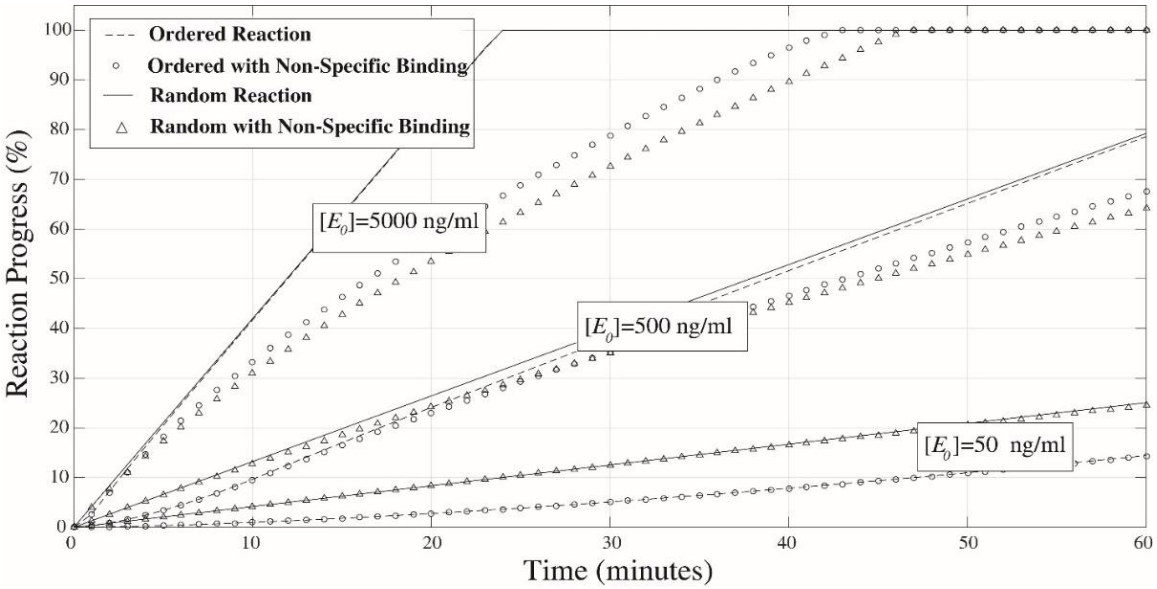

Figure 4.6: Reaction progress versus time for random and ordered reactions with and without considering non-specific binding.

To validate our models, the theoretical results are compared against experimental results of trypsin-polylysine reactions in nanochannels. Details of the setup, measurements, and the experimental results have been previously presented in (Duan *et al.* 2016). Measurement of the reaction progress in a nanochannel relies on the fact that it is entropically favorable for the cleft fragments of the immobilized PLL chains to leave the surface, which in turn causes a change in the surface charge density of the nanochannel walls. Since the surface charge is proportional to the conductance of the nanochannel at low ionic strength solution (Karnik *et al.* 2005a), the reaction progress can be monitored by measuring the conductance of the nanochannel. In Figure 4.7, reaction progress of random and ordered mechanisms versus enzyme concentration is compared against the experimental results. Six enzyme concentrations (5, 50, 200 500, 5000, and 50000 ng/ml) were considered and reaction progress was measured/calculated after one hour. The non-

specific adsorption of enzymes was also considered in the calculations, and a good agreement between the theoretical and experimental results was observed. At 5000 and 50000 ng/ml, both theoretical and experimental results indicate that reaction is over after one hour. At lower concentrations it seems that experimental results follow the ordered reaction's footprints. This suggests that, even though an endopeptidase, trypsin tends to cut fragments of PLL from one end in an ordered fashion. An explanation for this phenomenon could be due to the mobility of the chains' ends, enzymes are more likely to interact with the bonds at either ends, and therefore most of the cleft PLL bonds are located near the ends of the chains (Waley and Watson 1953). However, at the lowest concentration (5 ng/ml) experimental result is very close to the random reaction model, which needs to be addressed. Unfortunately, explaining the phenomena occurring at this really small concentration, corresponding to approximately a single molecule of enzyme in the nanochannel, is hampered by difficulties of performing more accurate experiments. Nevertheless, these comparisons confirm the accuracy of our models and suggest these two models can help us predict the progress of various enzymatic reactions in nanoscale-confined space. One last observation from this figure is that, as it was earlier discussed, reaction progress for ordered and random reactions are asymptotic to two solid lines indicating the slopes of $[E_o]$ and $\sqrt{[E_o]}$, respectively. Deviation of theoretical results from solid asymptotic lines at intermediate concentrations is due to non-specific adsorption of enzymes.

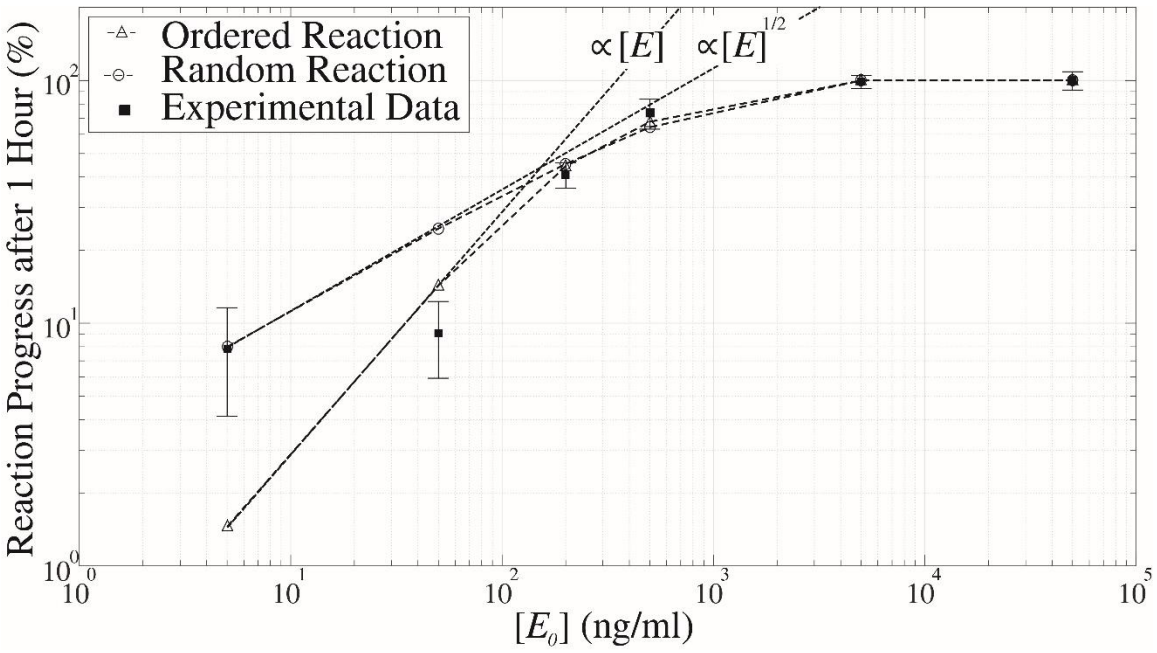

Figure 4.7: Comparison of the random and ordered reactions in nanochannel against experimental results for PLL- trypsin reaction.

One remained question is whether the nanochannel can accelerate the reaction compared with a "reaction on a surface" and thus provide us with a new tool for label-free detection of enzymes. To address this question, comparison of reaction in a nanochannel with surface reaction was performed over a fairly large range of enzyme concentrations, kinetic rate constants, substrate grafting density, enzyme diffusivity, and nanochannel dimensions. A new parameter, T_{50}, is defined which stands for the time that takes to complete 50% of a reaction. Calculations (not presented) demonstrated that reaction in nanochannels can be faster than surface reaction as we approach the low enzyme concentration limit (e.g., 5 ng/ml), and thus nanochannels may be promising tools for detection of very low concentration of analytes. Hence, further comparisons were limited to 5 ng/ml concentration. At this concentration a length study is performed to figure out at what

channel length, nanochannel reaction progress can surpass surface reaction. In Figures 8.a and 8.b, T_{50} is plotted in solid lines as a function of channel length for random and ordered reactions, respectively. T_{50} for the corresponding surface reactions is also plotted in dashed lines. It is clear that channels shorter than 11 μm (31 μm) for random (ordered) reaction give rise to a faster reaction compared to the corresponding on-surface reaction. Such accelerated reactions in nanochannels actually do not stem from the nanoscale confinement as we have shown that larger nanochannels would lead to faster reactions (see Figure 4.3.b and the corresponding discussion). Instead, these enhancements are attributed to the reduced diffusion length. In fact, at low enzyme concentrations due to formation of a large depletion zone on the surface the reaction rate is limited by diffusion. However, since enzymes only need to diffuse a relatively short distance along the nanochannel, reactions in nanochannel do not suffer from slow diffusion as much and thus can be faster. To further investigate the regime at which nanochannel is faster, a 5 μm long channel at enzyme concentration of 5ng/ml is considered. Parametric study suggests that values of the grafting density and the catalytic rate constant are key parameters that cause a significant difference between nanochannel and surface reactions. Figure 4.8.c shows in a random reaction, increasing the grafting density or decreasing k_{cat} makes the reaction in a nanochannel significantly faster than on-surface reaction. Similar trend is observed in Figure 4.8.d for the ordered reaction, except that the corresponding enhancement factor is relatively small, especially when decreasing k_{cat}. In addition, effect of k_a and k_d were investigated by changing them over a large range of magnitudes and it was observed (not presented) that they have a negligible effect in enhancement of reaction progress in nanochannels. Finally,

study of the enzyme diffusivity (not presented) suggested lower enzyme diffusivities can benefit from nanochannel more. In summary, nanochannels are appropriate for monitoring reactions with lower enzyme diffusivity, smaller k_{cat}, and larger $[S_n]$.

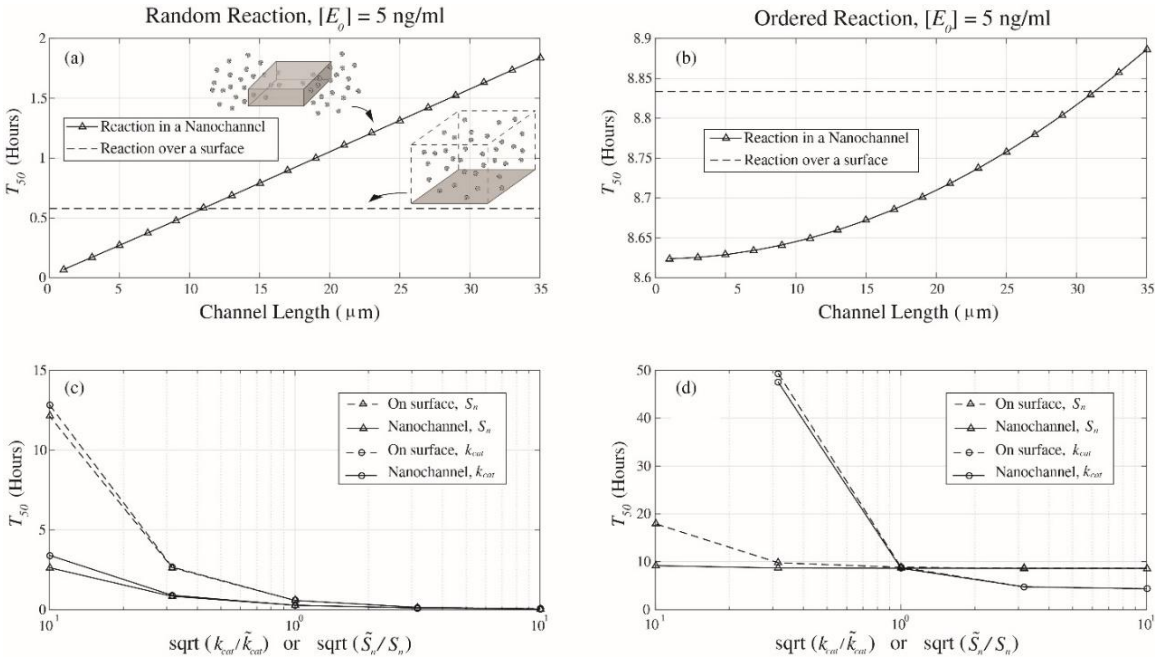

Figure 4.8: T_{50} versus channel length for (**a**) random reaction, and (**b**) ordered reaction, and comparing with their corresponding on-surface T_{50}. Comparison of T_{50} in nanochannel with its corresponding on-surface value versus catalytic rate constant and substrate density for (**c**) random reaction, and (**d**) ordered reaction, in a 5 μm long nanochannel. (ordered reaction at this very low enzyme concentration, for k_{cat} 100 times smaller than the original value is very slow and the corresponding T_{50} is not reported)

4.4 Conclusion

In this paper, an enzymatic reaction in a nanochannel was studied based on two different reaction mechanisms, i.e., random and ordered mechanisms. These two mechanisms mimic the endopeptidase and the exopeptidase enzyme actions and reflect the maximum and minimum reaction rate, respectively. It is observed that both mechanisms give rise to self-similar propagating reaction fronts in the nanochannel. Although differing in width and

developing time, both fronts propagate at the same constant speed once fully developed, indicating that diffusion determines the reaction rate inside the nanochannel. The propagating speed is a function of surface grafting density, enzyme concentration, channel geometry, catalytic rate constant and enzyme diffusivity. Further study of the non-specific adsorption of enzyme to the surface reveals that its role is significant only at high enzyme concentrations. Theoretical results of reaction in nanochannels were compared against experimental results and a good agreement between theory and experiment was observed. Finally, comparison of reaction progress in a nanofluidic channel with reaction on a surface disclosed that small enzyme diffusivity, small catalytic rate constant, and large substrate surface density at low enzyme concentration make the nanofluidic channel a faster tool for detection of enzymatic reaction compared with surface reaction based devices.

CHAPTER 5: Size Based Separation of Nanobeads in Solid-State Nanopores

Study of nanobeads translocating through solid state nanopores is an interesting problem which finds applications in biosensing. In this chapter, we study translocation of two different size of beads in low aspect ratio silicon nitride nanopores. The aims of this study are to (*i*) differentiate translocation signals of the two beads and (*ii*) measure the nanobead concentration based on beads' capture rate. Our results demonstrated that signals of two different bead sizes, i.e., 50 nm and 100 nm, can be reliably separated based on their translocation current. The capture rate, however, is a function of the nanopores' surface charge which may changes over time and varies from one pore to another making comparison between different experiments difficult. Therefore, better control of the pore's surface charge is necessary for accurate measurement of the capture rate. Study of nanobeads of different size translocating through different size of nanopores reveals that smaller beads translocate faster than large beads in the same pore, and for one the same size of beads translocation occurs more slowly in larger pores.

5.1 Introduction

Translocation of nanobeads through nanopores has been subject of extensive research due to its application in characterizing suspensions (Ben-Sasson *et al.* 1974; DeBlois and Bean 1970; Gregg and Steidley 1965; Grover *et al.* 1969a, 1972; Grover *et al.* 1969b; Saleh and Sohn 2001), i.e., measuring their size (Ben-Sasson *et al.* 1974; DeBlois and Bean 1970; Edwards *et al.* 2015; Gregg and Steidley 1965; Grover *et al.* 1969a, 1972; Grover *et al.* 1969b; Ito *et al.* 2003; Saleh and Sohn 2001), concentration (DeBlois and Bean 1970;

Gregg and Steidley 1965; Saleh and Sohn 2001), zeta potential/surface charge (Ito *et al.* 2003; Venta *et al.* 2014), and the diffusion coefficient (Angeli *et al.* 2015), and size similarity of nanobeads to liposomes (Rudzevich *et al.* 2014), viruses (DeBlois and Wesley 1977; Harms *et al.* 2011), or even individual cells (Ben-Sasson *et al.* 1974; Golibersuch 1973; Gregg and Steidley 1965; Grover *et al.* 1972). Additionally, nanobeads can mimic bio-nanoparticles such as proteins and biomolecules (Yeh *et al.* 2012). The antibody bound nanobeads have been used for resistive-pulse sensing of antibodies (Wang *et al.* 2013), cancer growth factors (Cai *et al.* 2015), and also detection of antibody–antigen binding (Saleh and Sohn 2003) and the DNA-nanobead conjugates (Wu *et al.* 2014) can be a new paradigm for probe/analytes detection. Besides the applied aspect of this problem, study of nanobeads translocation in nanopores can shed light on some intricate electrokinetics phenomena encountered in resistive pulse sensing (Bacri *et al.* 2011; Davenport *et al.* 2012; German *et al.* 2012; Goyal *et al.* 2013; Lan *et al.* 2011; Lan *et al.* 2014; Lan and White 2012; Liu *et al.* 2013; Pevarnik *et al.* 2012; Pevarnik *et al.* 2013; Qiu *et al.* 2016; Tsutsui *et al.* 2016; Tsutsui *et al.* 2012; Yeh *et al.* 2012; Zhang *et al.* 2009) which make performing the experiments and/or the data analysis difficult. The difficulty of this problem mainly arises from the number of factors contributing to the translocation events, such as pore size and aspect ratio, salt concentration, pH, applied bias, bead size and its surface charge or surface groups, etc. As a result there have been plenty of works on this problem over the past decade.

The existing studies from experimental view point can be roughly categorized based on the type of nanopores used for sensing: Glass nanopipette (Cai *et al.* 2015; Edwards *et al.* 2015;

German *et al.* 2012; Holden *et al.* 2011; Lan *et al.* 2011; Lan *et al.* 2014; Lan and White 2012; Wang *et al.* 2013), Carbon nanotube (Ito *et al.* 2003; Sun and Crooks 2000), PDMS pores (Angeli *et al.* 2015), and silicon nitride pores are the major types of nanopore used for this study, among which the silicon nitride pores is widely used owing to its ease of fabrication over a large range of diameters and excellent control over its length. With the aid of these nanopores translocation of different types of nanobeads/particles, e.g., solid beads with different surface groups, antibody or DNA coated beads (Cai *et al.* 2015; Saleh and Sohn 2003; Wang *et al.* 2013; Wu *et al.* 2014; Yeh *et al.* 2012), aspherical particles (Ai and Qian 2011; Golibersuch 1973; Venta *et al.* 2014), and deformable microgel (Holden *et al.* 2011) have been investigated in the past. Despite the wealth of literature on this subject our understanding of different aspects of this problem is limited and there's a room for further research, in particular if resistive pulse sensing for biosensing in clinical settings is intended. Accurate measurement of the beads concentration along with differentiation of beads based on their size or charge can enable and facilitate several biosensing modalities with the aid of beads. This requires optimal design of the pore size and right selection of the bead size for maximum sensitivity and perfect control over the pore and the beads' surface charge/surface group to allow for easy translocations with minimal interactions with the pore. Too large pores cause weak translocation signals which limits the capacity for detection and differentiation of different bead sizes. The pore-nanobead interactions also can yield either very long events (blockage) or very short collision with the pore without translocation (Bacri *et al.* 2011; Davenport *et al.* 2012) which leads to inaccurate estimation of the concentrations and makes extraction of the

intended information complicated. In some other cases due to these interactions no translocation can happen or only a certain bead size can translocate (Bacri *et al.* 2011; Prabhu *et al.* 2010). It's worth pointing out to another constraint in the design of experiments and that's the pH and the salt concentrations must be biologically relevant to be applicable to biosensing, and hence very low or high pH values and salt concentration must be avoided (Davenport *et al.* 2012).

In this chapter we study translocation of two different size nanobeads in a low aspect ratio silicon nitride pore. Our ultimate goals from this work is (*i*) to accurately separate translocation signals of two bead sizes and (*ii*) measure the nanobead concentration based on the capture rate of beads in the nanopore. In what follows, first the theoretical background necessary for understanding the nanobead translocation through silicon nitride pores is presented and our experimental procedures and results are detailed next. It will be demonstrated that with right design of the pore/bead combination in our experiments while very strong translocation signals can be obtained, the pore-bead interactions are minimal.

5.2 Theoretical Background

Translocation of nanobeads through a nanopore causes a momentary decrease in the ionic current due to volume exclusion of the pore. Each translocation event can be characterized based on the translocation time, i.e., time that it takes for a bead to pass through a pore, and the translocation current, i.e., decrease in current due to passage of a bead. While the translocation current is mainly a function of pore geometry and the bead size (at high salt concentrations), the translocation time is a function of pore and beads zeta potential, and

applied bias, too. On the other hand, the capture rate of the beads which is a very important factor for measuring the concentration of beads and characterization of suspensions, is even more difficult to measure as it's a function of bead concentration, the energy barrier of translocation, as well the salt gradient. (Table 5.1) Understanding different forces involved in a translocation event is necessary for any further analysis and key to understanding how these factors influence the results. In what follows a brief derivation of the relevant equations is presented that clarifies the underlying physics of the translocation-associated phenomena.

Table 5.1: Important translocation quantities and the associated influencing factors.

Quantity	Influencing factors
Translocation current (%)	• Pore geometry • Bead size
Translocation time (sec)	• Pore geometry • Bead size • Zeta potential on the beads and the pore • Applied bias
Capture rate (event/sec)	• Pore geometry • Zeta potential on the beads and the pore • Bead concentration • Salt concentration gradient • Applied bias • Energy barrier

5.2.1 Electrophoretic and Electroosmotic Velocity

All charged particles accelerate under an external electric field and reach a steady state velocity when the electric force is balanced by the opposing viscous drag. For a spherical particle of radius a and zeta potential ζ, immersed in a liquid with viscosity η and dielectric

permittivity ε under the electric field $\vec{E}$, this velocity is proportional to the applied electric filed:

$$\vec{u} = \mu\vec{E} \tag{5.1}$$

The factor μ known as the mobility can be shown to take the form (Ohshima 2002):

$$\mu = \frac{2}{3}\frac{\varepsilon\zeta}{\eta}\mathrm{H}(\kappa a) \tag{5.2}$$

Here, $\mathrm{H}(\kappa a)$ is the Henry's function and depends on the thickness of the Debye layer ($1/\kappa$) which acts to screen the electrostatic interactions around the particle. The Debye layer thickness for a monovalent electrolyte can be written as:

$$\lambda = 1/\kappa = \sqrt{\frac{\varepsilon k_b T}{2ne^2}} \tag{5.3}$$

with k_b the Boltzmann constant, T the temperature, e the elementary charge and n the salt concentration. When the radius of the particle is significantly larger than the Debye layer thickness the Henry function would be equal to 1.5 (Figure 5.1) and the electrophoretic mobility is simplified to:

$$\mu = \frac{\varepsilon\zeta_{bead}}{\eta} \tag{5.4}$$

This assumption is valid when the beads are immersed in a high salt solutions where the Debye layer is very thin compared with the bead's diameter. For a 150 mM NaCl solution (used in our experiments throughout this entire chapter) the Debye length is less than 1 nm and the Henry function can be approximated as 1.5. This velocity -and its associated force- are called the electrophoretic velocity and is the main driving force behind the translocation of particles.

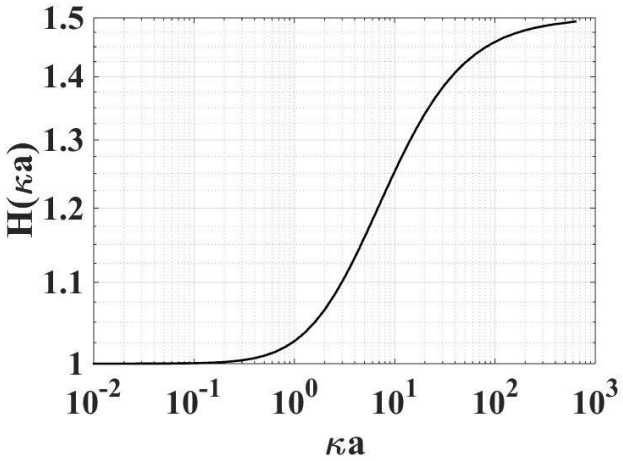

Figure 5.1: Henry function varies between 1 and 1.5.

Along with the electrophoretic force, there's another force stemming from the charge on the nanopore which counteracts on the particles. When a charged surface is wet by an electrolyte, the counter-ions form an electric double layer at the surface. For example, when the surface is negatively charged, cations from the electrolyte rearrange and form a layer at the surface to balance the electric field created by the negative surface charge. Now, when an external electric field is applied this mobile layer of cations starts to move and displace the adjacent electrolyte by viscous force. For an electrolyte in an infinitely long cylinder this velocity can be easily found by accounting for viscous stress and the electrostatic body force in the momentum equation. To find the body force we need to first find the electric potential in the pore. When $\psi \ll k_b T/e$ the Poisson-Boltzmann equation can be linearized as:

$$\nabla^2 \psi = \kappa^2 \psi \tag{5.5}$$

with ψ being the electric potential in the nanopore. For an infinitely long cylinder and uniform boundary conditions, ψ is only a function of radial coordinates and this equation

can be conveniently solved which finds a solution in the form of modified Bessel function of the first kind and zero[th] order:

$$\frac{1}{r}\frac{d}{dr}\left(r\frac{d\psi(r)}{dr}\right) = \kappa^2\psi(r)$$

$$\psi = A\, I_0(\kappa r) + B\, K_0(\kappa r)$$

$$\frac{d\psi}{dr}|_{r=0} = 0, \frac{d\psi}{dr}|_{r=a} = \frac{\sigma}{\varepsilon}$$

$$\psi(r) = \frac{\sigma}{\kappa\varepsilon}\frac{I_0(\kappa r)}{I_1(\kappa a)} \tag{5.6}$$

Here, σ is the surface charge on the pore's wall. After finding the electric potential in the pore, one can use it to find the body force and plug it in the Navier-Stokes equation.

$$\eta\nabla^2 u + \rho E = 0$$

with ρ being the charge density which can be replaced by an electric potential term according to the Poisson-Boltzmann equation:

$$\eta\nabla^2 u - E\varepsilon\nabla^2\psi = 0$$

$$\nabla^2\left(u - \frac{E\varepsilon}{\eta}\psi\right) = 0$$

No-slip boundary condition at the circumference of the pore and zero velocity gradient on the pore axis yields:

$$u(r) = \frac{\varepsilon E}{\eta}[\psi(r) - \zeta]$$

When the Debye length is smaller than the radius of the pore (non-overlapping electric double layer) the electric potential at the center of the channel is zero and the on-axis fluid velocity, known as the electroosmotic (EO) velocity, can be written as:

$$u_{EO} = -\frac{\varepsilon \zeta_{pore}}{\eta} E \tag{5.7}$$

Of course, the linearization assumption comes with some error as the electric potential in the pore is comparable with $k_b T/e$. In addition, here it was assumed that the pore is infinitely long and any entrance effect has been ignored which is not trivial. Nevertheless, these assumptions allow us to derive a relation for the electroosmotic velocity similar to the electrophoretic term and enables qualitative comparison of the two terms. (Figure 5.2)

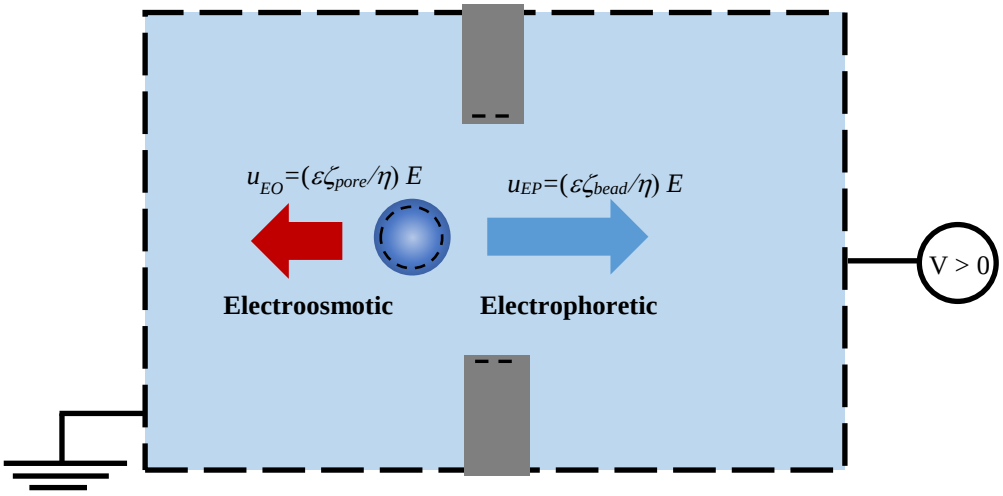

Figure 5.2: Electrophoretic and electroosmotic forces applied to a bead during translocation.

Based on what was explained, translocation of a bead can be electrophoretically driven or electro-osmotically driven and in case the two terms cancel each other no translocation happens. Needless to say, the translocation time also depends on the difference between the two velocities.

5.2.2 Electric field in the pore and the access resistance

In the previous part, we assumed that the electric field in the pore in known. This value is usually estimated as the applied voltage divided by the length of pore ($E = V/l$) which implicitly neglects any entrance effect. However, the entrance effect can be significant especially when the length of pore is smaller than the pore diameter. Conductance of such low-aspect-ratio pores is dominated by the access resistance associated with the pore entrance which means a significant potential drop occurs outside the pore. (Figure 5.3)

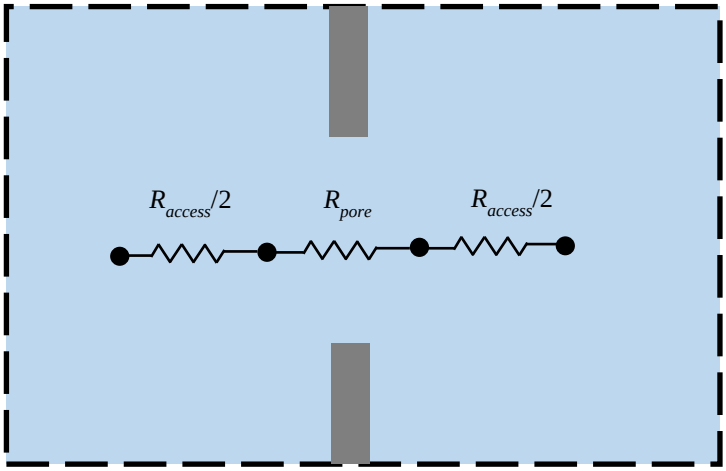

Figure 5.3: Schematics of a low aspect ratio nanopore and the resistance terms.

For low aspect ratio pores the total resistance of the pore can be written as (Davenport *et al.* 2012):

$$R = R_{pore} + R_{access}$$

$$R_{pore} = \frac{l}{\gamma A},\ R_{access} = \frac{1}{\gamma D}$$

$$R = \frac{(l + \pi D/4)}{\gamma A} \tag{5.8}$$

with γ being the conductivity of the electrolyte, D the diameter of the pore, A cross sectional area of the pore, l the length of pore. This is equivalent to extending the length of pore by $\pi D/4$. This allows us to determine the electric field in the pore more accurately:

$$E_{pore} \sim \frac{V}{l + \pi D/4} \tag{5.9}$$

Finally, in case $l \ll D$, $G = \frac{1}{R} = \gamma D$ which means unlike the long pores ($l > D$), the pore diameter determines the conductivity of the pore and not the pore's cross sectional area.

5.2.3 Translocation Current

Pore resistance when a bead is translocating can be written as: (for $d > l$)

$$R_{pore,bead} = \frac{1}{\gamma} \int_{-\frac{l}{2}}^{\frac{l}{2}} \frac{dx}{A(x)} = \frac{1}{\pi\gamma} \int_{-\frac{l}{2}}^{\frac{l}{2}} \frac{dx}{\left(\frac{D}{2}\right)^2 - h(x)^2}$$

and with $h(x)^2 = (\frac{d}{2})^2 - x^2$ the integral can be calculated as:

$$R_{pore,bead} = \frac{4}{\pi\gamma\sqrt{D^2 - d^2}} arctan\left(\frac{l}{\sqrt{D^2 - d^2}}\right) \tag{5.10}$$

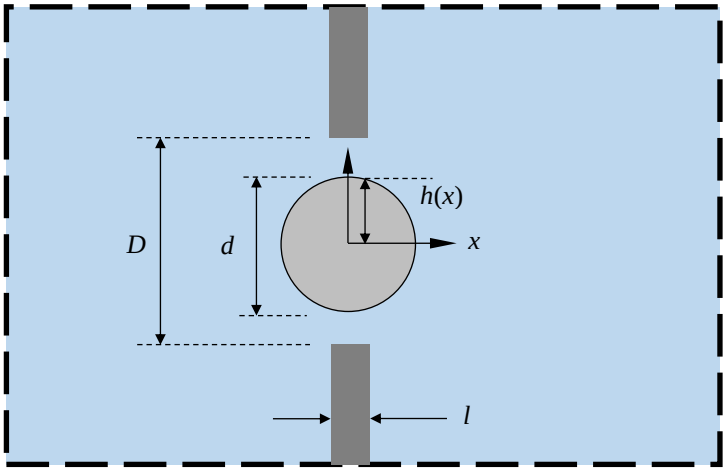

Figure 5.4: Pore resistance increases during a bead translocation.

Assuming that only pore resistance increases during translocation, the translocation current (in percentage) can be written as:

$$i = \frac{R_{pore,bead} - R_{pore}}{R_{pore} + R_{access}} \tag{5.11}$$

Another way to derive a relation for translocation current is to calculate the volume excluded by the bead from the pore. Maximum volume of the bead in the pore when $d > l$ occurs when bead is located at the center of the pore, and can be written as:

$$\delta_{Vol} = \int_{-l/2}^{l/2} \pi\, h(x)^2 dx = \pi\left(\frac{d^2 l}{4} - \frac{l^3}{12}\right)$$

$$\chi = \frac{\delta_{Vol}}{Vol} = \frac{\pi\left(\frac{d^2 l}{4} - \frac{l^3}{12}\right)}{\pi D^2 l/4} = \frac{d^2}{D^2} - \frac{l^2}{3D^2}$$

Pore resistance is expected to increase by $\delta R = \chi R_{pore}$. Therefore, again assuming only the pore resistance increases during translocation, the translocation current (%) can be written as:

$$i = \frac{\chi R_{pore}}{R_{pore} + R_{access}} \tag{5.12}$$

This equation allows us to find the optimal length of a pore if multiplexed detection of two size of beads, i.e., 50 and 100 nm, is to be studies. Summary of this analysis is presented in Figure 5.5. For two pore diameters of 150 nm and 250 nm, reasonably larger than size of the 100 nm bead, length of pore has to be 40 nm to yield the highest sensitivity for detection of the smaller bead in the larger pore.

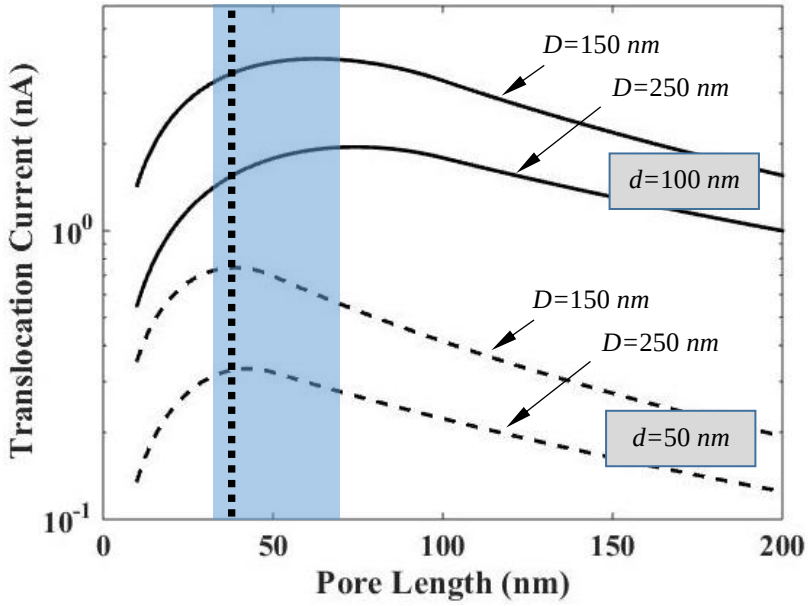

Figure 5.5: Translocation current of 50 and 100 nm beads passing through 150 and 250 nm pores. The dashed vertical line and the shaded area show the best and optimal design for the length of the pore. (γ=2 S/m)

5.2.4 Capture rate

In order to understand the capture rate of nanobeads in a nanopore, the electric field and the flow field far from pore must be understood. Considering the electroosmotic flow, a

nanopore acts as a source/sink positioned in a half-space. So by virtue of the continuity, the electroosmotic velocity far from the pore can be written as:

$$U_{EO}(r) = \frac{A_{pore}}{2\pi r^2} u_{EO} = -\frac{A_{pore}}{2\pi r^2} \frac{\varepsilon \zeta_{pore}}{\eta} E_{pore} = -\frac{A_{pore}}{2\pi r^2} \frac{\varepsilon \zeta_{pore}}{\eta} \frac{V}{l + \pi D/4}$$

Here r is the radial distance from the pore (in spherical coordinates). Moreover, the electric field extended to the chamber (where the bead suspension is placed) can be found as (Davenport *et al.* 2012):

$$E(r) = -\frac{d\psi}{dr} = I \frac{dR}{dr} = \frac{A_{pore}\, \gamma\, V}{l + \pi D/4} \frac{dR}{dr}$$

$$E(r) = \frac{A_{pore} \gamma V}{l + \pi D/4} \left(\frac{dr/2\pi r^2 \gamma}{dr} \right) = \left(\frac{V}{l + \pi D/4} \right) \frac{A_{pore}}{2\pi r^2} \tag{5.13}$$

which can be used to obtain the electrophoretic velocity as:

$$U_{EP}(r) = \frac{\varepsilon \zeta_{bead}}{\eta} E(r) = \frac{\varepsilon \zeta_{bead}}{\eta} \frac{V}{l + \pi D/4} \frac{A_{pore}}{2\pi r^2}$$

Finally, the beads velocity is the superposition of the two velocities:

$$U_{bead} = \frac{\varepsilon \{\zeta_{bead} - \zeta_{pore}\}}{\eta} \left(\frac{V}{l + \pi D/4} \right) \frac{A_{pore}}{2\pi r^2}$$

Beads at distance r move with this speed toward the pore. However, farther than certain distance, $r_{capture}$, beads can escape from the electric/flow field by diffusion. This distance can be found by equating the bead's velocity (U_{bead}) and the diffusive velocity:

$$U_{bead} = \frac{\beta}{r_{capture}}$$

$$r_{capture} = \frac{\varepsilon \{\zeta_{bead} - \zeta_{pore}\}}{\eta \beta} \left(\frac{V}{l + \pi D/4} \right) \frac{A_{pore}}{2\pi} \tag{5.14}$$

β is the bead's diffusion coefficient. Ultimately the capture rate is determined by the diffusion of beads across the border of the capture zone determined by $r_{capture}$:

$$f = 2\pi r_{capture}\beta\, C = \frac{\varepsilon\{\zeta_{bead} - \zeta_{pore}\}}{\eta}\left(\frac{V}{l + \pi D/4}\right) A_{pore} C$$

$$f = \mu_{eff}\,.\,E_{pore}\,.A_{pore}\,.C \tag{5.15}$$

Here C is the bead concentration and μ_{eff} is the beads' effective mobility:

$$\mu_{eff} = \frac{\varepsilon\{\zeta_{bead} - \zeta_{pore}\}}{\eta} \tag{5.16}$$

5.3 Fabrication and Measurement

In order to fabricate the nanopores, first 5 μm thick silicon oxide layer was deposited on a 4 inch silicon wafer followed by deposition of 40 nm LPCVD silicon nitride layer. Small windows were opened on one side of the wafer using the standard photolithography technique and the nitride layer was etched away by the reactive ion etching. Next, the oxide layer was removed by buffered oxide etchant (BOE) and the silicon was anisotropically etched along the [100] crystal direction using potassium hydroxide (KOH). Further, the oxide layer under the nitride was etched by BOE with surfactant to yield a free standing silicon nitride membrane 20 μm wide. (Figure 5.6.a) A dual column focused ion beam (FEI Quanta 3D FEG FIB) with 10 pA current at 30keV was used to mill the pores in the membranes. Typically, a thin layer of gold is deposited on the membrane for ease of imaging with the scanning electron microscope (SEM), which later must be removed by gold etchant. However, in this work in order to avoid introducing any foreign elements to the pore which may alter the pore condition the FIB process was performed without

deposition of gold. Before the measurements each chip was cleaned two times with Piranha (H2SO4:H2O2 3:1) at 110 ^{o}C for 10 minutes, followed by 5 minutes immersing in hot DI water (18 MOhm-cm) and finally rinsing under DI water stream and drying by nitrogen. All the surfaces of the chips other than the membrane were painted by a fast cure silicone rubber adhesive (Sil-poxy) to reduce the capacitance noise during the current measurement**.** (Figure 5.6.b) Finally chip was loaded into a Teflon holder with two chambers at either side (*cis* and *trans* chambers).

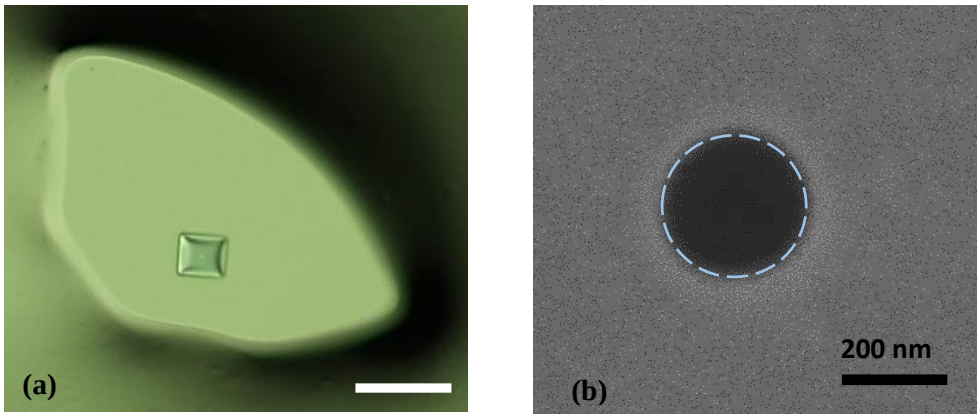

Figure 5.6: (a) Microscope image of a chip used for experiments with a free standing silicon nitride membrane at the center. Surface of the chip is painted by silicone adhesive to reduce the electrical noise. The scale bar is 40 μm. (b) SEM image of a nanopore milled by focused ion beam.

Silver/silver chloride electrodes were made by electroplating silver wires in KCl solutions prior to and several times during each experiment. An Axon 200B current amplifier with 100 kHz lowpass Bessel filter along with a Digidata 1550 digitizer (Molecular Devices, Inc.) at 500 kHz sampling rates were used for the measurement. The choice of 100 kHz lowpass filter allows to measure the translocation time as small as 7 micro-seconds, i.e., twice the rise time of the filter. No extra digital filter was applied to the recordings. A dark Faraday cage placed on a floating air table minimized the external electromagnetic

radiation and the vibration induced noise. All measurements were performed with Phosphate-buffered saline (PBS, Sigma Aldrich), equivalent to 150 mM NaCl at pH 7.4 mimicking the blood plasma. The PBS buffer was filtered with 20 nm alumina filter membrane (Whatman Anodisc) prior to use. The polystyrene nanobeads with carboxyl surface groups were bought from Bangs lab (Bangs Laboratories, Inc.) and different nanobead concentrations obtained with serial dilution with the PBS buffer. Bead suspensions were sonicated after dilution and were agitated before the experiments. Although use of surfactants can reduce nanobeads aggregation, we did not add any surfactants to the suspension to avoid reduction in the ζ-potential of the beads and the nanopores. If necessary to use surfactant, special attention must be paid to selection of the electrolyte concentration and the pH to ensure adequate surface charge on the beads for translocation. A MATLAB (The Mathworks, R2014b) script was written to find the height and width of each event for further post processing.

5.4 Nanobeads Characterization

Before any experiments the nanobeads must be characterized to obtain their accurate size distribution as well as the zeta potential. Nanobeads with different size, material and surface functional group were used for the experiments. However only some of them could translocate through the nanopores. Table 5.2 summarizes the nanobeads used for the experiments and whether they translocated through the nanopore.

Table 5.2: Summary of the beads used for the experiment.

Nanobead material	**Size**	**Results**
Silica, no surface functional group	50 nm	Successful
Silica, no surface functional group	140 nm	Successful
Polystyrene, Streptavidin coated	20 nm	Failed
Polystyrene, Streptavidin coated	50 nm	Failed
Polystyrene, COOH surface group	50 nm	Successful
Polystyrene, COOH surface group	100 nm	Successful
Polystyrene, NH_2 surface group	100 nm	Failed

Nanobeads size distribution were measured using two different techniques: The more reliable way of measuring the size distribution is to do Scanning Electron Microscope imaging of the beads and finding the size distribution by image processing in MATLAB (The Mathworks, R2014b). Alternatively Dynamic Light Scattering (Brookhaven 90 plus nanoparticle sizer) was used to measure the size distribution as well as the zeta potential of the beads. Figures 5.7 and 5.8 display the SEM image of the beads, size distribution based on SEM, size distribution based of DLS, and the light scattering phase diagram recorded during the zeta potential measurement. These figures correspond to the two types of polystyrene beads with successful translocation experiments as reported in Table 5.2. A good agreement between the size distributions obtained from the two methods was observed. The mean value of the beads size along with the measured zeta potential have been summarized in Table 5.3. The silica beads have quite wider size distributions and lower zeta potentials compared with polystyrene beads. The wide distribution of these beads does not allow us to perfectly discriminate the two bead size. In addition, the zeta potentials of these beads (-20 mV) is close to the zeta potential of the silicon nitride pore which may hamper the translocation. It's important to note that the silicon nitride zeta potential has been shown to be not very stable and may slowly change (Firnkes *et al.* 2010).

This has been observed in our experiments, too, where the absolute value of the pore zeta potential keeps increasing. As a result in some cases the silica beads don't translocate, or even translocate electro-osmotically in a direction opposite to the expected electrophoretic direction. Therefore, the polystyrene nanobeads with a narrow size distribution and a zeta potential quite different from the pore zeta potential have been used for the experiments.

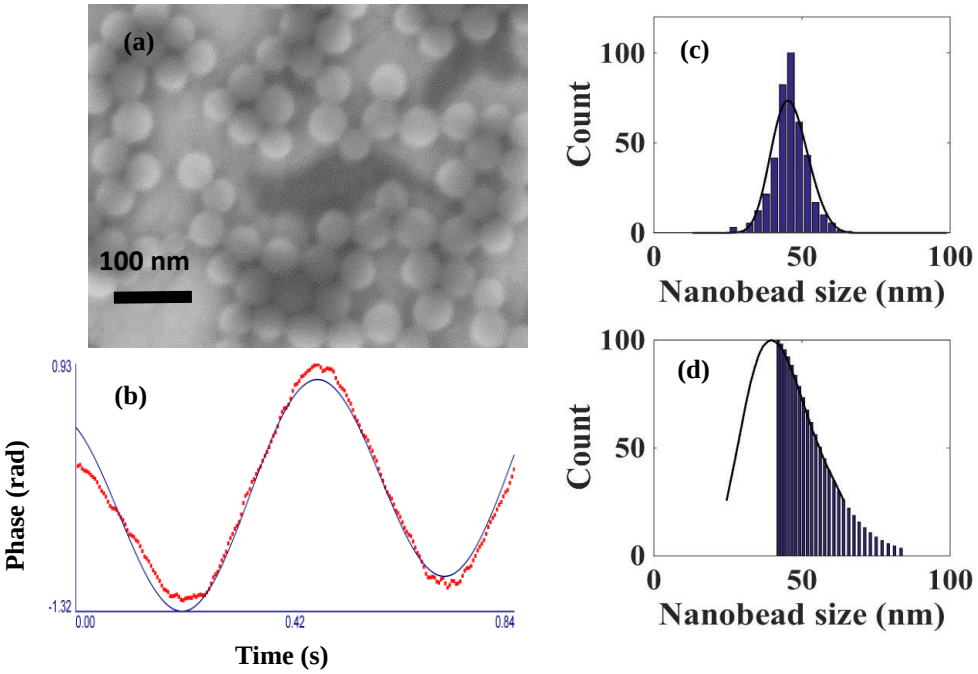

Figure 5.7: (a) SEM image of 50 nm polystyrene beads (with carboxyl group). (b) Light scattering phase diagram recorded in zeta potential measurement. (c) Size distribution of the beads based on image processing of the SEM images. (d) Size distribution of the beads measured by DLS. The solid line is the lognormal size distribution and the bars are based on multimodal size distribution.

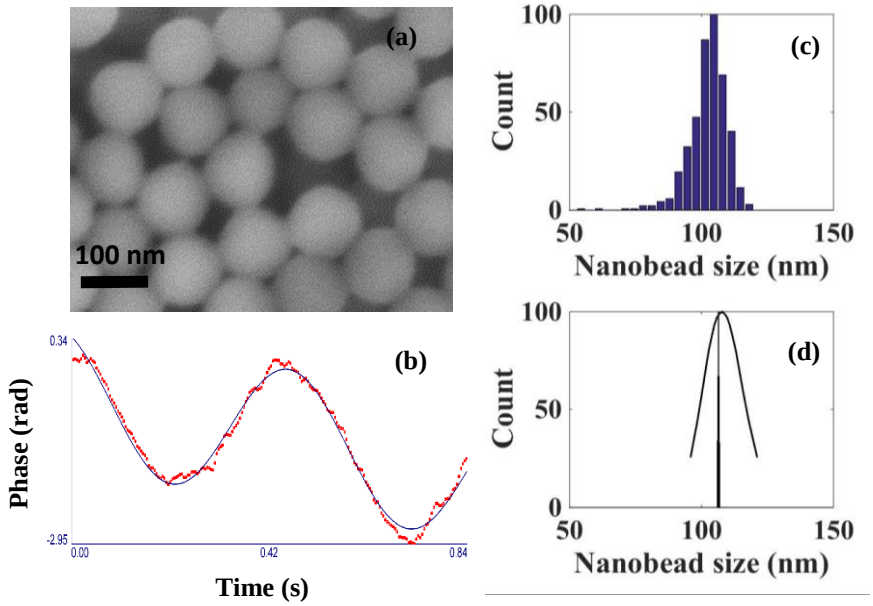

Figure 5.8: (a) SEM image of 100 nm polystyrene beads (with carboxyl group). (b) Light scattering phase diagram recorded in zeta potential measurement. (c) Size distribution of the beads based on image processing of the SEM images. (d) Size distribution of the beads measured by DLS. The solid line is the lognormal size distribution and the bars are based on multimodal size distribution.

Table 5.3: Summary of the beads used for the experiments, their size and zeta potential.

Nanobead	Mean diameter	Zeta potential
50 nm Polystyrene with carboxyl functional group	45 nm	-32.5± 1.4 mV
100 nm Polystyrene with carboxyl functional group	105 nm	-31.9 ± 2 mV

5.5 Pore conductance

All the experiments start by measuring the conductance of the nanopore with the same electrolyte used for the experiments. Here, Phosphate-buffered saline (PBS, Sigma Aldrich), equivalent to 150 mM NaCl at pH 7.4 was used for all the measurements. Conductance of the pores versus pore diameters is shown in Figure 5.9. The conductance is observed to be a linear function of diameter which is the consequence of the aspect ratio

of the pores. The SiN membranes have a thickness of ~40 nm which is quite smaller than the diameter of the pores.

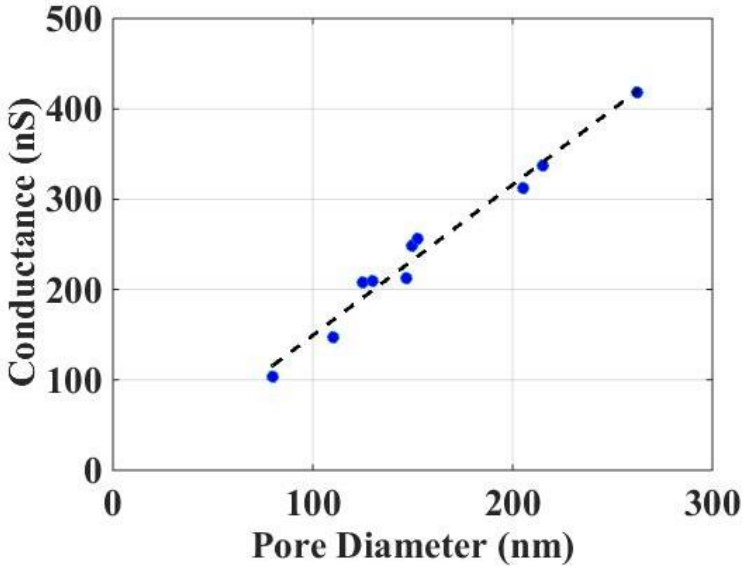

Figure 5.9: Conductance of the nanopores versus pore diameter measured with PBS buffer.

5.6 Experimental Results

5.6.1 Resistive pulse sensing of nanobeads

Upon successful characterization of the nanopore conductance, the suspension of nanobeads was placed in the *cis* chamber. The *cis* chamber was grounded and the *trans* chamber was biased at 150 mV. Upon applying voltage, translocation events appeared in the form of momentary decrease in the ionic current. Figure 5.10.a shows translocation of 6 pM of 100 nm polystyrene beads through a 130 nm pore.

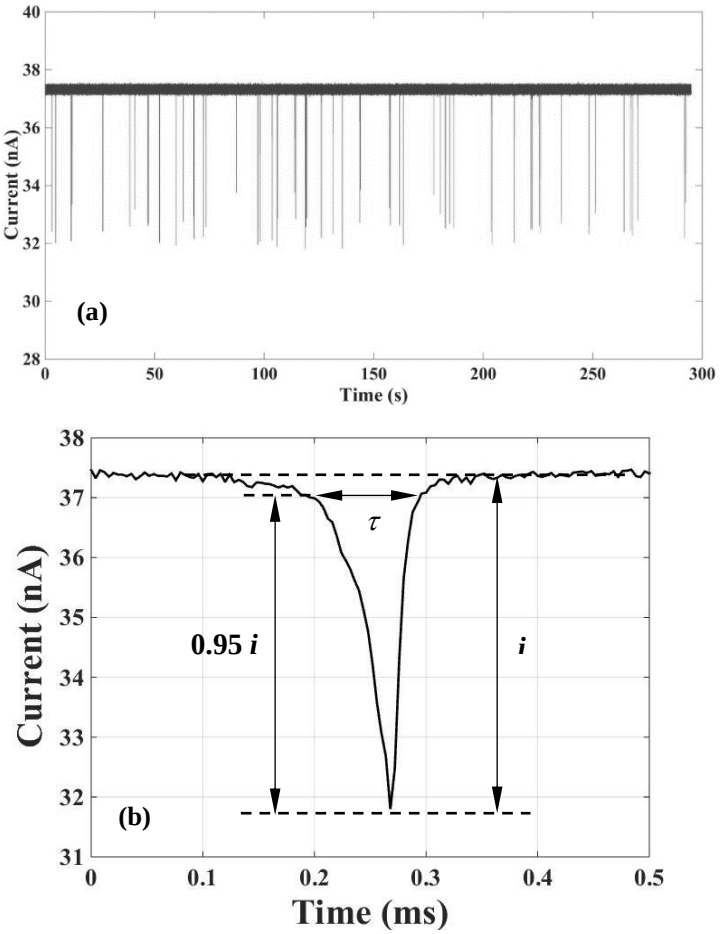

Figure 5.10: (**a**) Translocation of 100 nm PS beads through a 130 nm pore at 6 pM bead concentrations. (**b**) A single nanobead translocation.

Each event can be characterized based on the translocation height (current) and width (time). Here, the translocation time is defined as the time over which the current is at 5% of the maximum current change. (Figure 5.10.b) Figure 5.10.a shows data collected over a 5 minutes period. In case of lower concentration of beads the recording continued for 30 minutes without any blockage. Nevertheless, at some point during the measurement a bead blocks the pore and does not leave the pore by continuing to apply voltage. In such cases the electrolyte in both *cis* and *trans* chambers was replaced with a high salt concentration, in our case 20X PBS, for several minutes and the pore was easily opened. This way we

were always able to open the pores. Throughout our experiments no long translocation event or blockage, or very short ones as a results of collision of the beads with the pore edges was observed (Bacri *et al.* 2011; Davenport *et al.* 2012). Collecting enough numbers of events and extracting their translocation times and currents allows us to find their respective distributions and correlate them with the dimensions of the problem and the surface charge/zeta potential of the beads and the pores. For this purpose, translocation of 60 pM concentration of 100 nm polystyrene beads through different nanopore size ranging from 130 nm to 260 nm was studied. The results are presented in Figure 5.11. By increasing the pore diameter, the base current increases and the translocation current keeps decreasing both in terms of amplitude and ratio. The corresponding translocation current-time can be cast in the form of Figure 5.11.d to compare results of different pores. In case of the 130 nm pore, nanobeads of average 105 nm diameter block 65% of the pore's cross sectional area; however, only 13% decrease in the ionic current occurs. This indicates that access resistance of the pore is not influenced by the nanobead translocation as pointed out by other researchers in the past and only R_{pore} is increasing (Davenport *et al.* 2012; Tsutsui *et al.* 2016; Tsutsui *et al.* 2012). Consistent with our expectations, the translocation current ratio (TCR) decreases as the pore diameter increases. Figures 5.12a thru 5.12.d show the TCR distributions for 4 different pore sizes, i.e., 130 nm, 150 nm, 205 nm, and 260 nm. The *logistic distribution* can be used to best fit the data. The mean current obtained from the fittings is plotted in Figure 5.12.e versus the pore diameter along with the predictions of equations 5.11 and 5.12 to fit the data. The theoretical predictions and the experimental results are in good agreement in particular at larger pores, however they deviate at smaller

pore sizes. Moreover, it can be observed that equation 5.12 can better predict the experimental results compared with equation 5.11 which significantly overestimates the translocation current.

Unlike the translocation current which is only a function of pore geometry and bead size, the translocation time is a function of zeta potential, too. As a results any change in the pore charge manifests itself in the translocation time. For this reason it is hard to find the effect of pore geometry on the translocation time. Nevertheless, our data suggests that translocation occurs slower in the larger pores, consistent with findings in the literature which shows nanobeads' mobility moving in a circular pore monotonically decreases as the ratio of the bead's diameter to pore diameter increases (Hsu *et al.* 2004; Jubery *et al.* 2012; Keh and Chiou 1996).

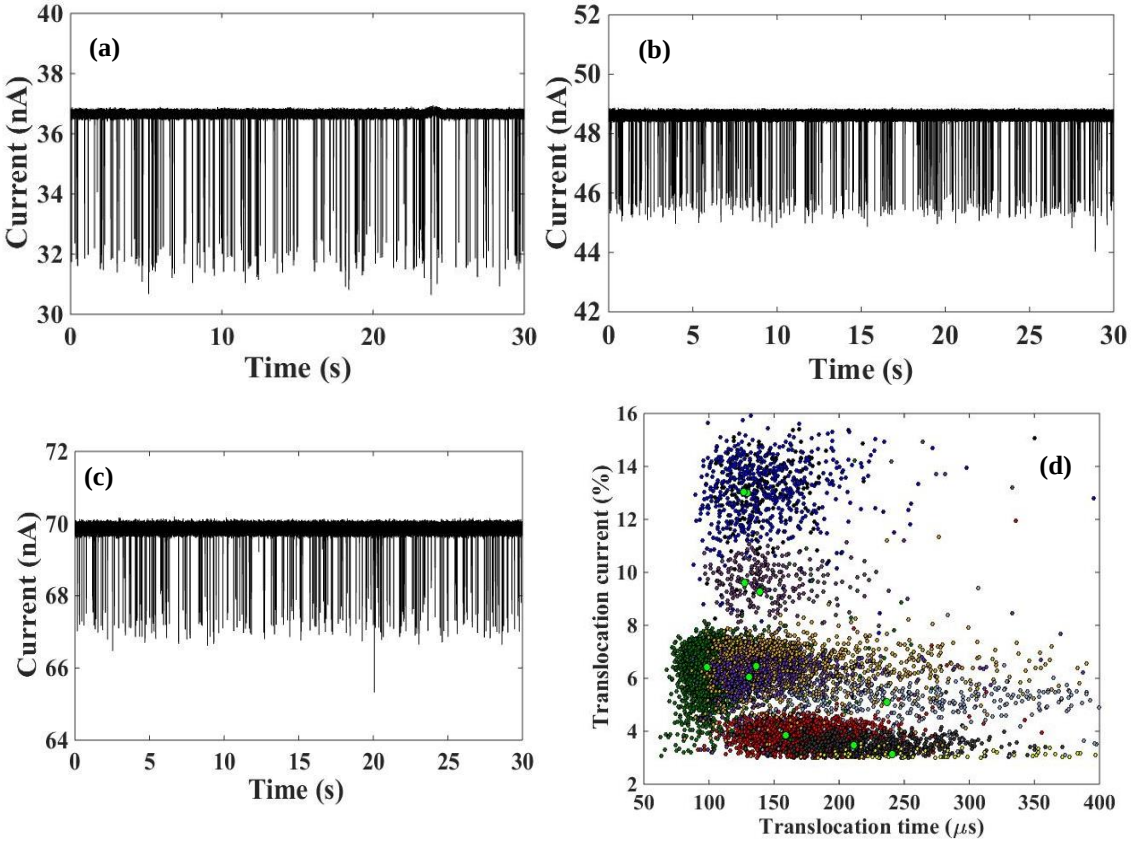

Figure 5.11: Translocation of 60 pM bead concentrations 100 nm PS beads through a (**a**) 130 nm pore (**b**) 200 nm pore, and (**c**) 260 nm pore. (**d**) Translocation results of 100 nm beads through different pore sizes. The large green circles indicate the mean translocation current-time for each distribution.

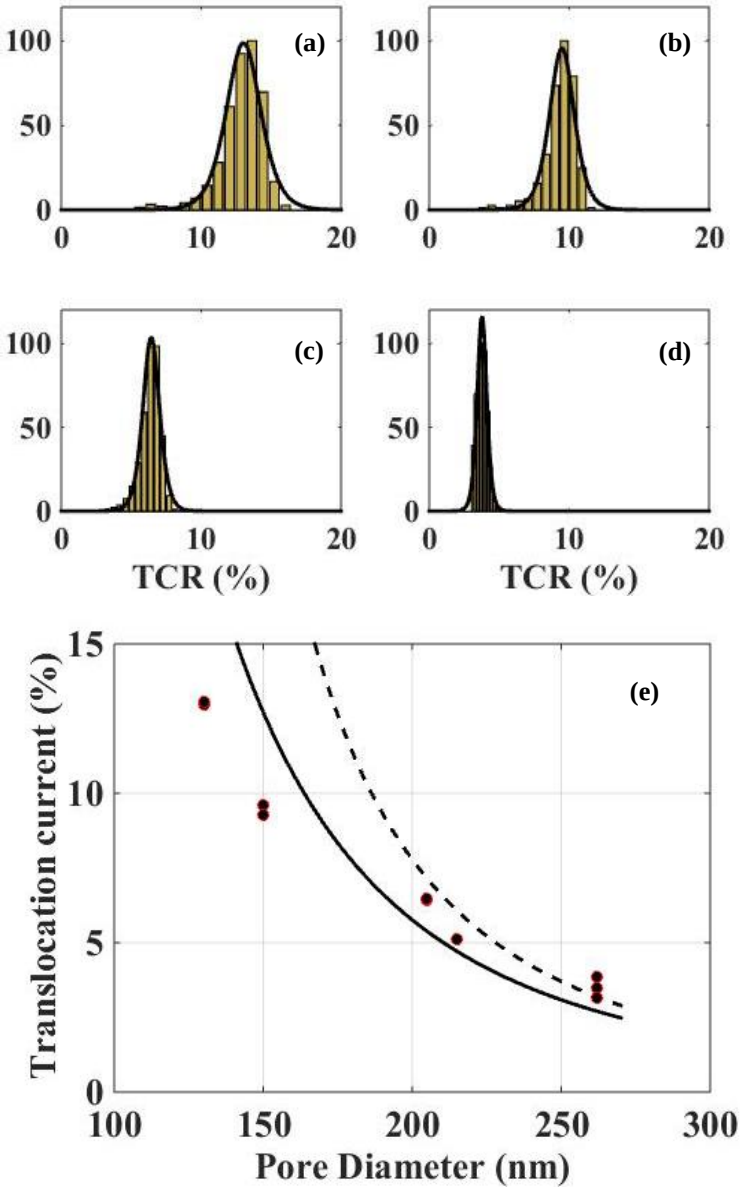

Figure 5.12: Distribution of translocation current ratio (TCR) for 100 nm PS beads thru (**a**) 130 nm, (**b**) 150 nm, (**c**) 205 nm and (**d**) 260 nm pores. (**e**) Translocation current of 100 nm PS beads versus pore diameter; dashed line is based on equation 5.11 and solid line is based on equation 5.12.

5.6.2 Differentiation of the nanobeads

The major goal of this work is to be able to differentiate two different beads based on their translocation signal. Here, two sizes of beads, i.e., 50 nm and 100 nm polystyrene beads both with carboxyl surface group were used for this purpose. The zeta potential of both beads were verified to be the same ($\zeta = -32$ mV). Translocation of a mixture of beads with final concentration of 30 pM each through a 205 nm pore is shown in Figure 5.13. The two bead sizes yield quite different signal heights allowing us to differentiate them. Casting the time trace in the form of scatter plot of translocation time-current indicates that the 3% translocation current can divide the two cloud of data and allows us to separately fit distributions to the translocation times and currents. The mean translocation current ratio for the 50 nm beads is measured to be 1.15% versus the 6.4% for the 100 nm beads. The theoretical predictions for these two values are 0.7% (with 45 nm actual diameter of the beads) and 5.4%. While the theoretical prediction for larger beads is in good agreement with experiment, for smaller beads theory underestimates the experiment. This may be due to the fact that smaller beads have a diameter very close the length of pore. Translocation of bead mixture through a 260 nm pore yields similar results (Figure 5.14) and the two cloud of data can be reliably split by drawing the 1.5% current ratio line. With this pore, the experimental translocation current ratio for the 50 nm bead is 0.58% and for the 100 nm beads is 2.7%. The theoretical predictions of these values are 0.35% and 2.7%, respectively, which similar to the previous experiment shows an underestimation of the experiments by theory for the 50 nm beads.

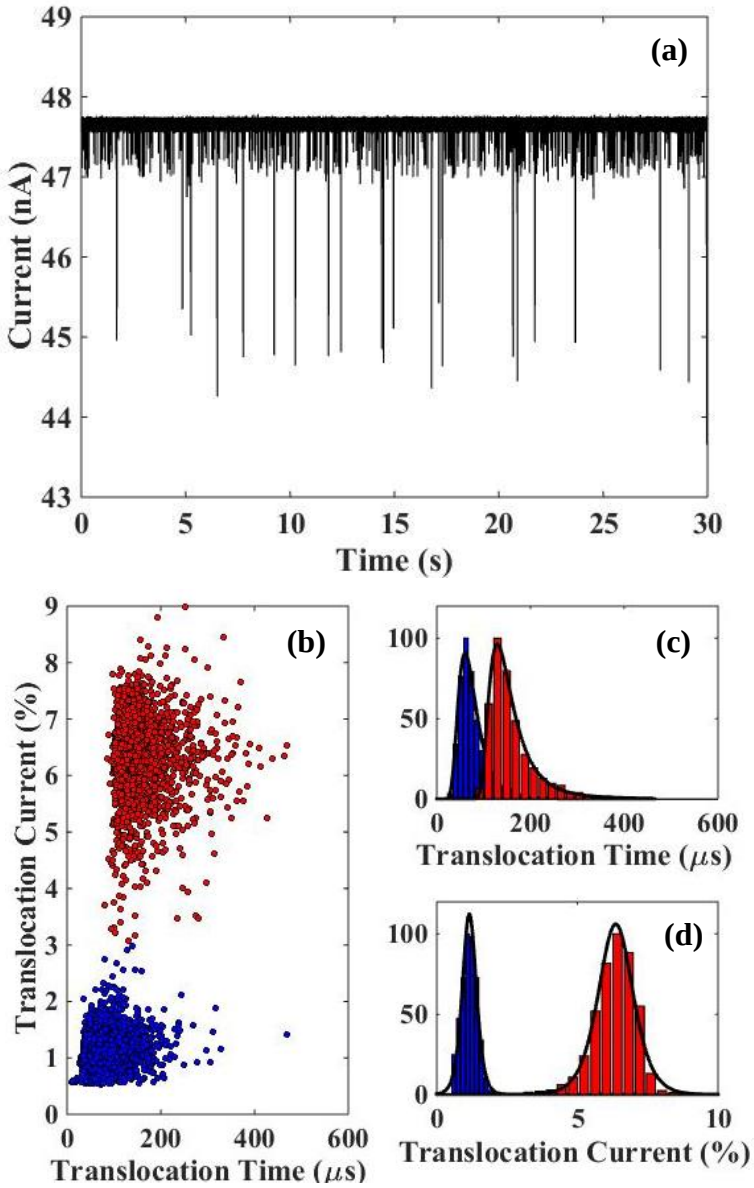

Figure 5.13: (**a**) Time trace of translocation of mixed 50 nm and 100 nm beads passing through a 205 nm pore. The final concentration of both beads is 30 pM (**b**) Scatter plot of the translocation time and current. The 3% current line divides the two distributions. (**c**) Translocation time distribution and (**d**) translocation current distribution for each nanobead size.

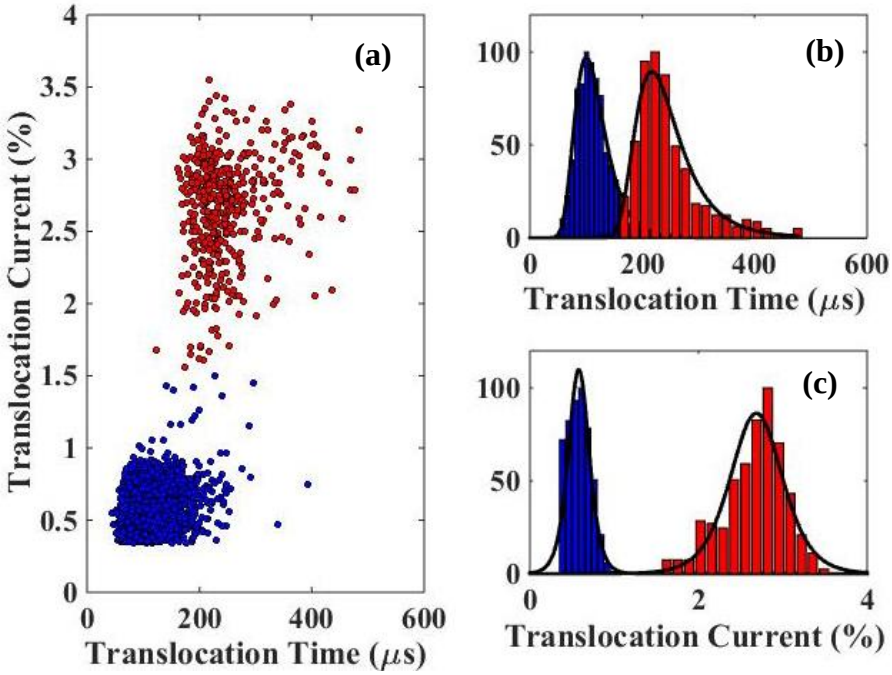

Figure 5.14: (**a**) Scatter plot of translocation time and current for mixed 50 nm and 100 nm beads passing through a 260 nm pore. The final concentration of 50 nm beads is 60 pM and final concentration of 100 nm beads is 15 pM (1.5% current line divides the two distributions) (**b**) Translocation time distribution and (**c**) translocation current distribution for each nanobead size.

Unlike the translocation current ratio, the translocation time distribution has a tail at higher values for which the *generalized extreme value distribution* better fits the experimental data. For the 205 nm pore, the mean translocation time of the 50 nm beads is 60 micro seconds compared with the 130 micro seconds for the 100 nm beads. While the translocation time of the larger beads is double the smaller ones, nevertheless, accurate differentiation of beads based on the translocation time is not possible due to overlap of the two distributions. Similar observation was made in translocation of mixed beads through a 260 nm pore where the translocation time of 50 nm beads was measured to be 100 micro seconds, compared with 215 micro seconds translocation time of the 100 nm beads. (Figure 5.14) In both cases, smaller beads despite having the same zeta potential as

the larger beads translocate faster through the pores. This is consistent with our previous observation that larger the pore, the 100 nm beads translocate slower, and suggest that the ratio of the size of beads to the size of pore determines the translocation time (Hsu *et al.* 2004; Jubery *et al.* 2012; Keh and Chiou 1996). In fact, the study of translocation of mixed beads allows us to eliminate the varying factor in measurement of translocation time, i.e., the pore's zeta potential, and enables accurate evaluation of the effect of pore/bead size on the translocation time.

5.6.3 Capture rate

Upon successful detection of nanobeads in the nanopore and characterization of translocation events, determining the concentration of beads is of interest. The capture rate of beads in the nanopore was discussed earlier in the theoretical background section, and a simple equation was derived that correlated the bead's capture rate to the bead concentration, pore geometry, applied bias and zeta potential on the beads and the pore. Accuracy of this relation was further experimentally examined and most importantly the capture rate of a fixed size pore against the bead concentration was studied. The bead concentration varied between 0.6 pM to 60 pM and the capture rate was measured in a 130 nm pore. (Figure 5.15) At the lowest concentration the recording continued for 30 minutes, unlike the high concentration for which even 1 minutes is enough to yield an accurate capture rate. It can be observed that by increasing bead's concentration the capture rate increases. However, capture rate is not a linear function of the bead concentration. In order to compare the experimental results with theory, the zeta potential on the pore must be

known. For this pore the estimated pore's zeta potential of -18mV was used to calculate the theoretical capture rate.

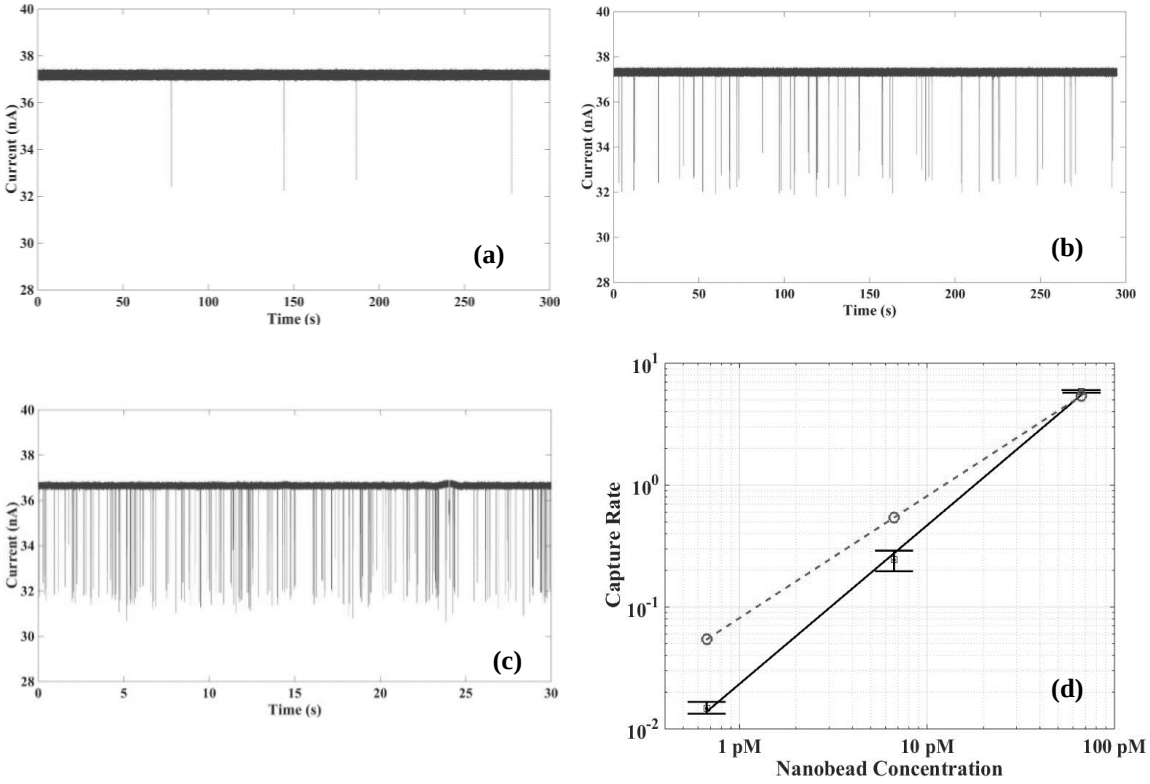

Figure 5.15: Translocation of 100 nm PS beads through a 130 nm pore at (**a**) 600 fM (**b**) 6 pM and (**c**) 60 pM bead concentrations. (**d**) Capture rate of 100 nm PS beads in a 130 nm pore at different bead concentrations and comparison with theory (dashed line). ζ_{pore} =-18 mV predicts the highest concentration value well.

The dashed line in this figure in the theoretical prediction based on equation 5.15 which agrees well with the experimental results at 60 pM bead concentration. At lower concentrations however, the results start to deviate. These results suggest that the range of concentration for reliable detection by nanopores in the current setting is limited to ~1 pM. This detection limit however can be improved by creating a salt concentration gradient along the pore (Wanunu *et al.* 2010). One major challenge for accurate measurement of the capture rate is the knowledge of pore's zeta potential. Any change in the zeta potential

alters the beads' speed and the capture rate, and hence perfect control of the zeta potential is needed to ensure repeatable measurements.

Further the capture rate versus the applied bias was studied in a 260 nm pore. (Figure 5.16) 60 pM bead concentration was placed in the *cis* chamber and the applied bias increased from 50 mV to 400 mV. The capture rate linearly increased with voltage consistent with the predictions. Similar to the previous case the pore zeta potential must be known in order to compare the experiments with theory. In this experiment, $\zeta = -26$ mV can predict the experimental results, and using $\zeta = -18$ mV as in the previous experiment would overestimate the capture rate as shown in this figure with a solid line.

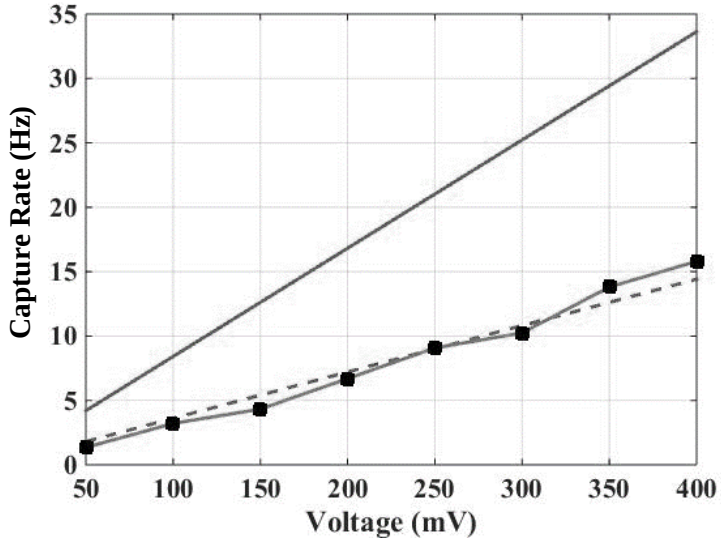

Figure 5.16: Capture rate of 100 nm PS beads in a 260 nm pore at different voltages and comparison with theory: markers are experimental values, the dashed line is calculated with ζ_{pore} =-26 mV and the solid line is for the case of ζ_{pore}=-18 mV. (Nanobead concentration is 60 pM)

5.6.4 Conclusions

In this chapter, translocation of nanobeads through silicon nitride nanopores was experimentally studied. Our results demonstrated that signals of two different bead sizes can be reliably separated based on the translocation current. The nanopore's surface charge seems to increase over time and get closer to the beads surface charge. This causes the capture rate to decrease and translocation time to increase, making comparison between different experiments difficult. The pore's surface charge may also vary from one pore to another and as a result comparison of the capture rate and translocation time between different pores becomes difficult. Therefore, better control of the pore's surface charge is necessary for accurate measurement of the capture rate. On the other hand, unlike translocation time, the translocation current does not appreciably change by change in pore charge. Study of nanobeads of different size translocating through different size of nanopores reveals that smaller beads translocate faster than large beads in the same pore, and for one the same size of beads translocation occurs more slowly in larger pores.

Appendix 1: Error Analysis in Hybrid Nanochannel Scheme

Possible detection range of this method along with the expected error can be understood from a comprehensive error analysis. Without loss of generality let's assume the observation channel is the reference channel. Experimental A can be determined from a set of $(T_i, X_i), i = 1..m$, measured in the reference channel when the water is introduce from the reference channel side (Figure 2.1.b), by minimizing error using the following relations:

$$\epsilon^2 = \sum_{i=1}^{m} (X_i{}^2 - 2AT_i)^2$$

$$\frac{\partial \epsilon^2}{\partial A} = 0$$

$$A = \frac{\sum_{i=1}^{m} X_i{}^2 T_i}{2\sum_{i=1}^{m} T_i{}^2} \tag{A1.1}$$

Similarly, η can be found from a set of $(t_i, x_i), i = 1..n$, measured in the hybrid channel when the water is introduced from the test channel side (Figure 2.1.c):

$$\epsilon^2 = \sum_{i=1}^{n} (\frac{1}{2} x_i{}^2 + \frac{L^*}{\eta} x_i - At_i)^2$$

$$\frac{\partial \epsilon^2}{\partial \eta} = 0$$

$$\frac{1}{\eta} = \frac{A}{L^*} \frac{\sum_{i=1}^{n} x_i t_i}{\sum_{i=1}^{n} x_i{}^2} - \frac{1}{2L^*} \frac{\sum x_i{}^3}{\sum_{i=1}^{n} x_i{}^2} \tag{A1.2}$$

Given $\eta = f(t_i, x_i, A)$, the temporal error (E_t), the spatial error (E_x), and the error associated with A (E_A) determine the total error as:

$$E = \sqrt{{E_A}^2 + {E_x}^2 + {E_t}^2} \tag{A1.3}$$

Calculations showed that the temporal error is insignificant compared to the other terms ($E_t \ll E_A, E_x$), and can be safely ignored. Therefore, for the sake of brevity only derivations of E_A and E_x are presented.

Error associated with A: E_A can be expressed as:

$$E_A = \frac{1}{\eta}\left|\frac{\partial \eta}{\partial A}\delta A\right| \tag{A1.4}$$

In which both $\frac{\partial \eta}{\partial A}$ and δA must be determined. δA can be written as:

$$\delta A = \sqrt{\sum_{i=1}^{m}\left(\frac{\partial A}{\partial X_i}\delta X\right)^2 + \left(\frac{\partial A}{\partial T_i}\delta T\right)^2}$$

From equation (A1.1) we get $\frac{\partial A}{\partial X_i} = \sqrt{2A}\frac{{T_i}^{3/2}}{\sum_{j=1}^{m}{T_j}^2}$. Given the very small contribution of the temporal error ($\left|\frac{\partial A}{\partial T_i}\delta T\right| \ll \left|\frac{\partial A}{\partial X_i}\delta X\right|$), δA can be written as:

$$\delta A = \sqrt{2A}\,\delta X\,\frac{\sqrt{\sum_{i=1}^{m}{T_i}^3}}{\sum_{i=1}^{m}{T_i}^2}$$

Here, δX is the spatial resolution (of the microscope), and τ is the time interval between two consecutive frames. The total number of data points is calculated as: $m = \frac{T_{max}}{\tau} = \frac{L^2}{2A\tau}$, with L being length of the reference channel. Moreover, one can write $T_i = i\tau$, which yields:

$$\delta A \cong \sqrt{2A}\delta X\sqrt{\tau}\frac{\sqrt{\frac{1}{4}m^4}}{\frac{1}{3}m^3} = \frac{3\sqrt{2}\sqrt{A\tau}\,A\delta X}{L^2} \tag{A1.5}$$

Here, for the sake of simplicity we have assumed m>>1. Having found δA, next we need to find a relation for $\frac{\partial \eta}{\partial A}$ to plug into equation (A1.4). Equation (A1.2) for $\frac{\partial \eta}{\partial A}$ yields:

$$\frac{\partial \eta}{\partial A} = -\eta^2 \frac{1}{L^*}\frac{\sum x_i t_i}{\sum_{i=1}^{n} {x_i}^2}$$

Deriving equations for asymptotic cases of $\eta \ll 1$ and $\eta \gg 1$and then combining the equations yields relations that can accurately reproduce the error throughout the entire parametric space. In case of $\eta \ll 1$: $x_i = \frac{A\eta}{L^*}t_i$ and $\frac{\partial \eta}{\partial A} = -\frac{\eta}{A}$. Hence:

$$E_A|_{\eta \ll 1} = \frac{1}{\eta}\left|\frac{\partial \eta}{\partial A}\delta A\right| = \frac{3\sqrt{2}\sqrt{A\tau}\,\delta X}{L^2} \tag{A1.6}$$

In case of $\eta \gg 1$:${x_i}^2 = 2At_i$ and $\frac{\partial \eta}{\partial A} = \frac{2}{5}\frac{L}{A}$, yielding the following relation for E_A:

$$E_A|_{\eta \gg 1} = \frac{1}{\eta}\left|\frac{\partial \eta}{\partial A}\delta A\right| = \frac{6\sqrt{2}}{5}\frac{\sqrt{A\tau}\,\delta X}{LL^*}\eta \tag{A1.7}$$

Combining equations (A1.6) and (A1.7) yields:

$$E_A = \sqrt{A\tau}\delta X\left(\frac{c_1}{L^2} + \frac{c_2}{LL^*}\eta\right) \tag{A1.8}$$

with $c_1 = 3\sqrt{2}, c_2 = \frac{6\sqrt{2}}{5}$.

Spatial Error (E_x): A similar approach is adopted for determining the spatial error.E_x can be expressed as:

$$E_x = \frac{1}{\eta}\left|\frac{\partial \eta}{\partial x}\delta x\right| \tag{A1.9}$$

$\frac{\partial \eta}{\partial x}$ can be found from equation (A1.2):

$$\frac{\partial \eta}{\partial x_j} = -\frac{\eta^2}{L^*}\left\{A\frac{t_j\sum_{i=1}^{n}{x_i}^2 - 2x_j\sum x_i t_i}{(\sum_{i=1}^{n}{x_i}^2)^2} - \frac{1}{2}\frac{3{x_j}^2\sum_{i=1}^{n}{x_i}^2 - 2x_j\sum {x_i}^3}{(\sum_{i=1}^{n}{x_i}^2)^2}\right\}$$

Again, E_x can be analytically found for asymptotic cases of $\eta \ll 1$, and $\eta \gg 1$:

$$E_x|_{\eta\ll 1} = \sqrt{A\zeta}\delta x\frac{\sqrt{3}}{{L^*}^{1/2}L^{3/2}}\sqrt{\eta} \tag{A1.10}$$

$$E_x|_{\eta\gg 1} = \frac{2\sqrt{2}}{\sqrt{3}}\sqrt{A\zeta}\delta x\frac{\eta}{LL^*} \tag{A1.11}$$

with ζ being the time interval between two consecutive frames and δx being the special resolution of the microscope (which may or may not be the same as τ and δX). Combining the two equations above yields:

$$E_x = \sqrt{A\zeta}\delta x\left(\frac{c_3}{{L^*}^{1/2}L^{3/2}}\sqrt{\eta} + \frac{c_4}{LL^*}\eta\right) \tag{A1.12}$$

with $c_3 = \sqrt{3}, c_4 = \frac{2\sqrt{2}}{\sqrt{3}}$.

Our full numerical solution of the error (with no estimation about η) indicated that equations (A1.3), (A1.8) and (A1.12) can very accurately estimate the error. According to these relations, at small values of η, the major source of error is the term associated with c_1, which is proportional to $\frac{\sqrt{A\tau}\delta X}{L^2}$ and is independent of η and L^*. At large values of η, however, the terms associated with c_2 and c_4 are dominant and the error is proportional to $\frac{\sqrt{A\zeta}\delta x}{LL^*}\eta$ which grows large with increasing η, and also may be reduced by choosing a longer

test channel (L^*). Numerical value of the error for $\tau = \zeta = 10$ ms (100 fps), $\delta x = \delta X = 1$ μm, $L = 350$ μm and $L^* = 50$ μm, for water flowing in a reference channel with $h = 30$ nm, suggests that error at low η range is negligible (Figure 2.2). At large values of η, however, error can be large and in order to reduce the error, a higher frame rate as well as a longer test channel must be considered. For example, measuring η up to 10^4 with only 20% error is possible, if the length of test channel is increased up to 2 mm and a high speed camera with a frame rate as high as 10^4 is utilized. It is worth noting that the spatial and temporal resolution can also be further improved by utilizing techniques such as Field Effect Transistors (FET) along the test/reference conduits and cross-channel current measurements using E-beam defined metal electrodes on two sides of the channel.

It is worth noting that both η and A maybe derived from a single experiment without any need to do the reference channel test, i.e., by introducing water from test channel side and using equation (2.8) along with a least square fitting method. However, further error analysis showed that results obtained from this approach are not as accurate as the two-step approach. In particular, at small values of η ($\eta \ll 1$), $x = \frac{A\eta}{L^*}t$, which suggests that in such a case only $A * \eta$ can be found from a single experiment.

Appendix 2: Derivation of a 1-D model based on PNP equation

The Poisson-Nernst-Planck equation relating charge density and electrostatic potential can be employed to solve this problem:

$$\nabla^2\varphi = \frac{-\sum z_i n_i\, e}{\varepsilon\varepsilon_0} \tag{A2.1}$$

$$\frac{\partial n_i}{\partial t} + \mathbf{u}.\nabla n_i = \nabla.\left(D_i\nabla n_i + n_i\,\frac{D_i z_i e}{k_b T}\nabla\varphi\right) \tag{A2.2}$$

where the index i refers to either of cations or anions, n is the concentration of species, D_i is the diffusivity of species, k_b is the Boltzmann constant, T is the temperature, z_i is the valence, e is the elementary charge, φ is the electric potential, and $\mathbf{u}$ is the velocity vector. Assuming the electroosmotic flow is negligible ($\mathbf{u} = \mathbf{0}$) and for steady state condition the Nernst-Planck equation is simplified to:

$$\nabla.J_i = 0 \tag{A2.3}$$

where J_i is the flux of cations and anions, defined by:

$$J_i = -D_i\nabla n_i - n_i\,\frac{D_i z_i e}{k_b T}\nabla\varphi \tag{A2.4}$$

Let's assume the ions are monovalent ($|z_i| = 1$) and the diffusion coefficient D for the cations and anions is the same. Then, for the section of the channel with height h_1 and width w, equation (A2.4) can be written as:

$$Q_i = -h_1 D\,\frac{dn_i}{dx} - h_1 n_i\,\frac{D_i z_i e}{k_b T}\frac{d\varphi}{dx} \tag{A2.5}$$

In addition, according to the electroneutrality principle, with the surface charge σ the cations and anions concentrations in this part of channel must satisfy

$$n_+ + \frac{2\sigma}{eh_1} = n_- \tag{A2.6}$$

Let's define the quantities M and I as:

$$M = Q_+ + Q_- = -h_1 D\frac{dN}{dx} + \frac{2\sigma D}{k_b T}\frac{d\varphi}{dx} \tag{A2.7}$$

$$I = Q_+ - Q_- = -\frac{Nh_1 De}{k_b T}\frac{d\varphi}{dx} \tag{A2.8}$$

with $N = n_+ + n_-$. M and I are proportional the mass flow rate and the current ($i = Iwe$) and hence must be continuous along the entire channel. Integrating equation (A2.7) with respect to x yields:

$$N = N_1 - \frac{M}{Dh_1}(x - x_1) + \frac{2\sigma}{k_b T h_1}(\varphi - \varphi_1) \tag{A2.9}$$

$$x = x_1 + \left(\frac{Dh_1 N_1}{M} + \frac{2\sigma DI}{M^2 e}\right)\left[1 - \exp\left(\frac{Me(\varphi - \varphi_1)}{Ik_b T}\right)\right] + \frac{2\sigma D}{Mk_b T}(\varphi - \varphi_1) \tag{A2.10}$$

Here the index "1" refers to the entrance of the nanochannel shown in Fig. 1. Setting $x = x_2$ in the equations above yields:

$$N_2 = N_1 - \frac{ML_1}{Dh_1} + \frac{2\sigma}{k_b T h_1}(\varphi_2 - \varphi_1) \tag{A2.11}$$

$$L_1 = \left(\frac{Dh_1 N_1}{M} + \frac{2\sigma DI}{M^2 e}\right)\left[1 - \exp\left(\frac{Me(\varphi_2 - \varphi_1)}{Ik_b T}\right)\right] + \frac{2\sigma D}{Mk_b T}(\varphi_2 - \varphi_1) \tag{A2.12}$$

Similarly, for the second part of the channel we can write:

$$N_4 = N_3 - \frac{ML_2}{Dh_2} + \frac{2\sigma}{k_b T h_2}(\varphi_4 - \varphi_3) \tag{A2.13}$$

$$L_2 = \left(\frac{Dh_2N_3}{M} + \frac{2\sigma DI}{M^2 e}\right)\left[1 - \exp\left(\frac{Me(\varphi_4 - \varphi_3)}{Ik_bT}\right)\right] + \frac{2\sigma D}{Mk_bT}(\varphi_4 - \varphi_3) \quad \text{(A2.14)}$$

Equations (A2.11) thru (A2.14) form a system of 4 equations with 6 unknowns $N_2, \varphi_2, N_3, \varphi_4, M$ and I. Two additional equations can be obtained by writing the Boltzmann equilibrium at the discontinuity between points 2 and 3:

$$n_{i,2} = n_{i,3}\ exp\left(\frac{-z_i e(\varphi_2 - \varphi_3)}{k_bT}\right) \quad \text{(A2.15)}$$

Equation (A2.15) combined with electroneutrality relations $n_{+,2} + \frac{2\sigma}{eh_1} = n_{-,2}$ and $n_{+,3} + \frac{2\sigma}{eh_2} = n_{-,3}$ correlate the concentrations and electric potentials across the discontinuity:

$$N_2^2 - (\frac{2\sigma}{eh_1})^2 = N_3^2 - (\frac{2\sigma}{eh_2})^2 \quad \text{(A2.16)}$$

$$\varphi_2 - \varphi_3 = \frac{k_bT}{e} ln \frac{N_2 + \frac{2\sigma}{eh_1}}{N_3 + \frac{2\sigma}{eh_2}} \quad \text{(A2.17)}$$

With these two equations the system of equations is close and can be numerically solved with a nonlinear solver to yield the value of current for any applied voltages. It's important to note that the concentration and the electric potential at the entrance of the nanochannel (points 1 and 4 in Fig. 1) are different from the reservoirs values. However assuming an equilibrium between the reservoir and the nanochannel entrance, one can utilize the Boltzmann distribution to correlate the entrance values to the reservoir values. Assuming the left reservoir is grounded ($\varphi_{left\ res.} = 0$) and the right reservoir is biased at voltage v ($\varphi_{right\ res.} = v$) we can write:

$$N_1 = N_{res}\sqrt{1 + (\frac{2\sigma}{eh_1 N_{res}})^2} \tag{A2.18}$$

$$N_4 = N_{res}\sqrt{1 + (\frac{2\sigma}{eh_2 N_{res}})^2} \tag{A2.19}$$

$$\varphi_1 = \frac{k_b T}{e}\frac{\sigma}{|\sigma|}cosh^{-1}\left(\sqrt{1 + (\frac{2\sigma}{eh_1 N_{res}})^2}\right) \tag{A2.20}$$

$$\varphi_4 = v + \frac{k_b T}{e}\frac{\sigma}{|\sigma|}cosh^{-1}\left(\sqrt{1 + (\frac{2\sigma}{eh_2 N_{res}})^2}\right) \tag{A2.21}$$

Since $N_{left}, N_{right}, \varphi_{right}$ and φ_{left} are known, we can directly find the values for $N_1, N_4, \varphi_1, \varphi_4$. We can use the following quantities to nondimensionalize the system of equation:

$$\bar{x} = \frac{x}{L}, \qquad \bar{\varphi} = \frac{\varphi}{\frac{k_b T}{e}}, \qquad \bar{N} = \frac{N}{\frac{2\sigma}{eh_1}},$$
$$\bar{M} = \frac{M}{2\sigma D/eL}, \qquad \bar{I} = \frac{I}{M}, \;\; \tau = \frac{h_2}{h_1} \tag{A2.22}$$

Then our system of equations becomes:

$$\bar{N_2}^2 - 1 = \bar{N_3}^2 - \frac{1}{\tau^2} \tag{A2.23.1}$$

$$\bar{\varphi}_2 - \bar{\varphi}_3 = ln\frac{\bar{N}_2 + 1}{\bar{N}_3 + \frac{1}{\tau}} \tag{A2.23.2}$$

$$\bar{M}l = -(\bar{N}_2 - \bar{N}_1) + (\bar{\varphi}_2 - \bar{\varphi}_1) \tag{A2.23.3}$$

$$\bar{M}(1 - l) = -(\bar{N}_4 - \bar{N}_3) + (\bar{\varphi}_4 - \bar{\varphi}_3) \tag{A2.23.4}$$

$$l = \left(\frac{\bar{N}_1}{\bar{M}} + \frac{\bar{I}}{\bar{M}}\right)\left[1 - \exp\left(\frac{\bar{\varphi}_2 - \bar{\varphi}_1}{\bar{I}}\right)\right] + \frac{1}{\bar{M}}(\bar{\varphi}_2 - \bar{\varphi}_1) \qquad \text{(A2.23.5)}$$

$$1 - l = \left(\frac{\bar{N}_3}{\bar{M}} + \frac{\bar{I}}{\bar{M}}\right)\left[1 - \exp\left(\frac{\bar{\varphi}_4 - \bar{\varphi}_3}{\bar{I}}\right)\right] + \frac{1}{\bar{M}}(\bar{\varphi}_4 - \bar{\varphi}_3) \qquad \text{(A2.23.6)}$$

with l being the length ratio $l = \frac{L_1}{L}$.

References

Abgrall P. & Nguyen N.T. (2008) Nanofluidic devices and their applications. *Analytical Chemistry* **80**, 2326–2341.

Ai Y. & Qian S. (2011) Electrokinetic particle translocation through a nanopore. *Physical Chemistry Chemical Physics* **13**, 4060–4071.

Alcaraz A., Ramírez P., García-Giménez E., Lopez M.L., Andrio A. & Aguilella V.M. (2006) A pH-tunable nanofluidic diode: electrochemical rectification in a reconstituted single ion channel. *Journal of Physical Chemistry B* **110**, 21205–21209.

Alibakhshi M.A., Xie Q., Li Y. & Duan C. (2016) Accurate measurement of liquid transport through nanoscale conduits. *Scientific Reports* **6**, 24936.

Andersen M.B., Bruus H., Bardhan J.P. & Pennathur S. (2011) Streaming current and wall dissolution over 48h in silica nanochannels. *Journal of Colloid and Interface Science* **360**, 262–271.

Angeli E., Volpe A., Fanzio P., Repetto L., Firpo G., Guida P., Lo Savio R., Wanunu M. & Valbusa U. (2015) Simultaneous Electro-Optical Tracking for Nanoparticle Recognition and Counting. *Nano Letters* **15**, 5696–5701.

Anker J.N., Hall W.P., Lyandres O., Shah N.C., Zhao J. & Van Duyne R.P. (2008) Biosensing with plasmonic nanosensors. *Nature Materials* **7**, 442–453.

Apel P.Y., Blonskaya I., Levkovich N. & Orelovich O. (2011) Asymmetric track membranes: Relationship between nanopore geometry and ionic conductivity. *Petroleum Chemistry* **51**, 555–567.

Apel P.Y., Korchev Y.E., Siwy Z., Spohr R. & Yoshida M. (2001) Diode-like single-ion track membrane prepared by electro-stopping. *Nuclear Instruments and Methods in Physics Research Section B: Beam Interactions with Materials and Atoms* **184**, 337–346.

Asay D.B. & Kim S.H. (2005) Evolution of the adsorbed water layer structure on silicon oxide at room temperature. *Journal of Physical Chemistry B* **109**, 16760–16763.

Bacri L., Oukhaled A., Schiedt B., Patriarche G., Bourhis E., Gierak J., Pelta J. & Auvray L. (2011) Dynamics of colloids in single solid-state nanopores. *Journal of Physical Chemistry B* **115**, 2890–2898.

Baldessari F. (2008) Electrokinetics in nanochannels: Part I. Electric double layer overlap and channel-to-well equilibrium. *Journal of Colloid and Interface Science* **325**, 526–538.

Becker T. & Mugele F. (2003) Nanofluidics: viscous dissipation in layered liquid films. *Physical Review Letters* **91**, 166104.

Behrens S.H. & Grier D.G. (2001) The charge of glass and silica surfaces. *Journal of Chemical Physics* **115**, 6716–6721.

Ben-Sasson S., Patinkin D., Grover N. & Doljanski F. (1974) Electrical sizing of particles in suspensions IV. Lymphocytes. *Journal of Cellular Physiology* **84**, 205–214.

Betancourt T. & Brannon-Peppas L. (2006) Micro-and nanofabrication methods in nanotechnological medical and pharmaceutical devices. *International Journal of Nanomedicine* **1**, 483.

Bi H., Qiao L., Busnel J.-M., Liu B. & Girault H.H. (2009) Kinetics of proteolytic reactions in nanoporous materials. *Journal of Proteome Research* **8**, 4685–4692.

Bocquet L. & Charlaix E. (2010) Nanofluidics, from bulk to interfaces. *Chemical Society Reviews* **39**, 1073–1095.

Cai H., Wang Y., Yu Y., Mirkin M.V., Bhakta S., Bishop G.W., Joshi A.A. & Rusling J.F. (2015) Resistive-Pulse Measurements with Nanopipettes: Detection of Vascular Endothelial Growth Factor C (VEGF-C) Using Antibody-Decorated Nanoparticles. *Analytical Chemistry* **87**, 6403–6410.

Cervera J. & Schiedt B. (2005) A Poisson/Nernst-Planck model for ionic transport through synthetic conical nanopores. *EPL (Europhysics Letters)* **71**, 35.

Chauvet F., Geoffroy S., Hamoumi A., Prat M. & Joseph P. (2012) Roles of gas in capillary filling of nanoslits. *Soft Matter* **8**, 10738–10749.

Cheng L.-J. & Guo L.J. (2007) Rectified ion transport through concentration gradient in homogeneous silica nanochannels. *Nano Letters* **7**, 3165–3171.

Cheng L.-J. & Guo L.J. (2009) Ionic current rectification, breakdown, and switching in heterogeneous oxide nanofluidic devices. *ACS Nano* **3**, 575–584.

Colville K., Tompkins N., Rutenberg A.D. & Jericho M.H. (2009) Effects of poly (L-lysine) substrates on attached Escherichia coli bacteria. *Langmuir* **26**, 2639–2644.

Constantin D. & Siwy Z.S. (2007) Poisson-Nernst-Planck model of ion current rectification through a nanofluidic diode. *Physical Review E* **76**, 041202.

Cosentino C., Amato F., Walczak R., Boiarski A. & Ferrari M. (2005) Dynamic model of biomolecular diffusion through two-dimensional nanochannels. *Journal of Physical Chemistry B* **109**, 7358–7364.

Daiguji H., Oka Y. & Shirono K. (2005) Nanofluidic diode and bipolar transistor. *Nano Letters* **5**, 2274–2280.

Daiguji H., Yang P. & Majumdar A. (2004) Ion transport in nanofluidic channels. *Nano Letters* **4**, 137–142.

Davenport M., Healy K., Pevarnik M., Teslich N., Cabrini S., Morrison A.P., Siwy Z.S. & Létant S.E. (2012) The role of pore geometry in single nanoparticle detection. *ACS nano* **6**, 8366–8380.

DeBlois R. & Bean C. (1970) Counting and sizing of submicron particles by the resistive pulse technique. *Review of Scientific Instruments* **41**, 909–916.

DeBlois R.W. & Wesley R. (1977) Sizes and concentrations of several type C oncornaviruses and bacteriophage T2 by the resistive-pulse technique. *Journal of Virology* **23**, 227–233.

Dong M. & Chatzis I. (1995) The imbibition and flow of a wetting liquid along the corners of a square capillary tube. *Journal of Colloid and Interface Science* **172**, 278–288.

Duan C., Alibakhshi M.A., Kim D.-K., Brown C.M., Craik C.S. & Majumdar A. (2016) Label-Free Electrical Detection of Enzymatic Reactions in Nanochannels. *ACS Nano*. DOI: 10.1021/acsnano.6b02062

Duan C. & Majumdar A. (2010) Anomalous ion transport in 2-nm hydrophilic nanochannels. *Nature Nanotechnology* **5**, 848–852.

Dzyadevych S.V., Soldatkin A.P., Korpan Y.I., Arkhypova V.N., Anna V., Chovelon J.-M., Martelet C. & Jaffrezic-Renault N. (2003) Biosensors based on enzyme field-effect transistors for determination of some substrates and inhibitors. *Analytical and Bioanalytical Chemistry* **377**, 496–506.

Edel J.B. & De Mello A. (2009) *Nanofluidics: nanoscience and nanotechnology*. Royal Society of Chemistry.

Edwards M.A., German S.R., Dick J.E., Bard A.J. & White H.S. (2015) High-Speed Multipass Coulter Counter with Ultrahigh Resolution. *ACS Nano* **9**, 12274–12282.

Eijkel J.C. & Van Den Berg A. (2005) Nanofluidics: what is it and what can we expect from it? *Microfluidics and Nanofluidics* **1**, 249–267.

Fang S., Lee H.J., Wark A.W., Kim H.M. & Corn R.M. (2005) Determination of ribonuclease H surface enzyme kinetics by surface plasmon resonance imaging and surface plasmon fluorescence spectroscopy. *Analytical Chemistry* **77**, 6528–6534.

Firnkes M., Pedone D., Knezevic J., Döblinger M. & Rant U. (2010) Electrically facilitated translocations of proteins through silicon nitride nanopores: conjoint and competitive action of diffusion, electrophoresis, and electroosmosis. *Nano Letters* **10**, 2162–2167.

Gao J., Szoszkiewicz R., Landman U. & Riedo E. (2007) Structured and viscous water in subnanometer gaps. *Physical Review B* **75**, 115415.

García-Giménez E., Alcaraz A., Aguilella V.M. & Ramírez P. (2009) Directional ion selectivity in a biological nanopore with bipolar structure. *Journal of Membrane Science* **331**, 137–142.

German S.R., Luo L., White H.S. & Mega T.L. (2012) Controlling nanoparticle dynamics in conical nanopores. *Journal of Physical Chemistry C* **117**, 703–711.

Gervais T. & Jensen K.F. (2006) Mass transport and surface reactions in microfluidic systems. *Chemical Engineering Science* **61**, 1102–1121.

Ghasemi H., Ni G., Marconnet A.M., Loomis J., Yerci S., Miljkovic N. & Chen G. (2014) Solar steam generation by heat localization. *Nature Communications* **5**, 4449. doi:10.1038/ncomms5449

Giannini E.G., Testa R. & Savarino V. (2005) Liver enzyme alteration: a guide for clinicians. *Canadian Medical Association Journal* **172**, 367–379.

Goertz M.P., Houston J. & Zhu X.-Y. (2007) Hydrophilicity and the viscosity of interfacial water. *Langmuir* **23**, 5491–5497.

Golibersuch D. (1973) Observation of aspherical particle rotation in Poiseuille flow via the resistance pulse technique: I. Application to human erythrocytes. *Biophysical Journal* **13**, 265.

Goyal G., Freedman K.J. & Kim M.J. (2013) Gold nanoparticle translocation dynamics and electrical detection of single particle diffusion using solid-state nanopores. *Analytical Chemistry* **85**, 8180–8187.

Green Y., Edri Y. & Yossifon G. (2015) Asymmetry-induced electric current rectification in permselective systems. *Physical Review E* **92**, 033018.

Gregg E.C. & Steidley K.D. (1965) Electrical counting and sizing of mammalian cells in suspension. *Biophysical Journal* **5**, 393.

Grover N., Naaman J., Ben-Sasson S. & Doljanski F. (1969a) Electrical Sizing of Particles in Suspensions: I. Theory. *Biophysical Journal* **9**, 1398.

Grover N., Naaman J., Ben-Sasson S. & Doljanski F. (1972) Electrical Sizing of Particles in Suspensions: III. Rigid Spheroids and Red Blood Cells. *Biophysical Journal* **12**, 1099.

Grover N., Naaman J., Ben-Sasson S., Doljanski F. & Nadav E. (1969b) Electrical sizing of particles in suspensions: II. Experiments with rigid spheres. *Biophysical Journal* **9**, 1415.

Gruener S., Hofmann T., Wallacher D., Kityk A.V. & Huber P. (2009) Capillary rise of water in hydrophilic nanopores. *Physical Review E* **79**, 067301.

Guan W., Fan R. & Reed M.A. (2011) Field-effect reconfigurable nanofluidic ionic diodes. *Nature Communications* **2**, 506.

Hamblin M.N., Hawkins A.R., Murray D., Maynes D., Lee M.L., Woolley A.T. & Tolley H.D. (2011) Capillary flow in sacrificially etched nanochannels. *Biomicrofluidics* **5**, 021103.

Han A., Mondin G., Hegelbach N.G., de Rooij N.F. & Staufer U. (2006) Filling kinetics of liquids in nanochannels as narrow as 27 nm by capillary force. *Journal of Colloid and Interface Science* **293**, 151–157.

Han J. & Craighead H.G. (2000) Separation of long DNA molecules in a microfabricated entropic trap array. *Science* **288**, 1026–1029.

Haneveld J., Tas N.R., Brunets N., Jansen H.V. & Elwenspoek M. (2008) Capillary filling of sub-10nm nanochannels. *Journal of Applied Physics* **104**, 014309.

Harms Z.D., Mogensen K.B., Nunes P.S., Zhou K., Hildenbrand B.W., Mitra I., Tan Z., Zlotnick A., Kutter J.P. & Jacobson S.C. (2011) Nanofluidic devices with two pores in series for resistive-pulse sensing of single virus capsids. *Analytical Chemistry* **83**, 9573–9578.

Haywood D.G., Harms Z.D. & Jacobson S.C. (2014) Electroosmotic flow in nanofluidic channels. *Analytical Chemistry* **86**, 11174–11180.

Ho T.A., Papavassiliou D.V., Lee L.L. & Striolo A. (2011) Liquid water can slip on a hydrophilic surface. *Proceedings of the National Academy of Sciences of the United States of America* **108**, 16170–16175.

Holden D.A., Hendrickson G., Lyon L.A. & White H.S. (2011) Resistive pulse analysis of microgel deformation during nanopore translocation. *Journal of Physical Chemistry C* **115**, 2999–3004.

Holt J.K., Park H.G., Wang Y., Stadermann M., Artyukhin A.B., Grigoropoulos C.P., Noy A. & Bakajin O. (2006) Fast mass transport through sub-2-nanometer carbon nanotubes. *Science* **312**, 1034–1037.

Hsu J.-P., Ku M.-H. & Kao C.-Y. (2004) Electrophoresis of a spherical particle along the axis of a cylindrical pore: effect of electroosmotic flow. *Journal of Colloid and Interface Science* **276**, 248–254.

Ito T., Sun L. & Crooks R.M. (2003) Simultaneous determination of the size and surface charge of individual nanoparticles using a carbon nanotube-based Coulter counter. *Analytical Chemistry* **75**, 2399–2406.

Joshi R., Carbone P., Wang F., Kravets V., Su Y., Grigorieva I., Wu H., Geim A. & Nair R. (2014) Precise and ultrafast molecular sieving through graphene oxide membranes. *Science* **343**, 752–754.

Jubery T.Z., Prabhu A.S., Kim M.J. & Dutta P. (2012) Modeling and simulation of nanoparticle separation through a solid-state nanopore. *Electrophoresis* **33**, 325–333.

Jung J.-Y., Joshi P., Petrossian L., Thornton T.J. & Posner J.D. (2009) Electromigration current rectification in a cylindrical nanopore due to asymmetric concentration polarization. *Analytical Chemistry* **81**, 3128–3133.

Kalman E.B., Vlassiouk I. & Siwy Z.S. (2008) Nanofluidic bipolar transistors. *Advanced Materials* **20**, 293–297.

Karlsson R., Roos H., Fägerstam L. & Persson B. (1994) Kinetic and concentration analysis using BIA technology. *Methods* **6**, 99–110.

Karnik R., Castelino K., Fan R., Yang P. & Majumdar A. (2005a) Effects of biological reactions and modifications on conductance of nanofluidic channels. *Nano Letters* **5**, 1638–1642.

Karnik R., Castelino K. & Majumdar A. (2006) Field-effect control of protein transport in a nanofluidic transistor circuit. *Applied Physics Letters* **88**, 123114.

Karnik R., Duan C., Castelino K., Daiguji H. & Majumdar A. (2007) Rectification of ionic current in a nanofluidic diode. *Nano Letters* **7**, 547–551.

Karnik R., Fan R., Yue M., Li D., Yang P. & Majumdar A. (2005b) Electrostatic control of ions and molecules in nanofluidic transistors. *Nano Letters* **5**, 943–948.

Keh H.J. & Chiou J.Y. (1996) Electrophoresis of a colloidal sphere in a circular cylindrical pore. *AIChE Journal* **42**, 1397–1406.

Kharitonov A.B., Zayats M., Lichtenstein A., Katz E. & Willner I. (2000) Enzyme monolayer-functionalized field-effect transistors for biosensor applications. *Sensors and Actuators B: Chemical* **70**, 222–231.

Kim S.J., Wang Y.-C., Lee J.H., Jang H. & Han J. (2007) Concentration polarization and nonlinear electrokinetic flow near a nanofluidic channel. *Physical Review Letters* **99**, 044501.

Kovarik M.L. & Jacobson S.C. (2009) Nanofluidics in lab-on-a-chip devices. *Analytical Chemistry* **81**, 7133–7140.

Lan W.-J., Holden D.A., Zhang B. & White H.S. (2011) Nanoparticle transport in conical-shaped nanopores. *Analytical Chemistry* **83**, 3840–3847.

Lan W.-J., Kubeil C., Xiong J.-W., Bund A. & White H.S. (2014) Effect of surface charge on the resistive pulse waveshape during particle translocation through glass nanopores. *Journal of Physical Chemistry C* **118**, 2726–2734.

Lan W.-J. & White H.S. (2012) Diffusional motion of a particle translocating through a nanopore. *ACS Nano* **6**, 1757–1765.

Lee H.J., Wark A.W., Goodrich T.T., Fang S. & Corn R.M. (2005) Surface enzyme kinetics for biopolymer microarrays: a combination of Langmuir and Michaelis-Menten concepts. *Langmuir* **21**, 4050–4057.

Lee K.P., Arnot T.C. & Mattia D. (2011) A review of reverse osmosis membrane materials for desalination—development to date and future potential. *Journal of Membrane Science* **370**, 1–22.

Lee K.P., Leese H. & Mattia D. (2012) Water flow enhancement in hydrophilic nanochannels. *Nanoscale* **4**, 2621–2627.

Lee W.G., Kim Y.-G., Chung B.G., Demirci U. & Khademhosseini A. (2010) Nano/Microfluidics for diagnosis of infectious diseases in developing countries. *Advanced Drug Delivery Reviews* **62**, 449–457.

Leng Y. & Cummings P.T. (2005) Fluidity of hydration layers nanoconfined between mica surfaces. *Physical Review Letters* **94**, 026101.

Li L., Kazoe Y., Mawatari K., Sugii Y. & Kitamori T. (2012) Viscosity and wetting property of water confined in extended nanospace simultaneously measured from highly-pressurized meniscus motion. *Journal of Physical Chemistry Letters* **3**, 2447–2452.

Li L., Mo J. & Li Z. (2015) Nanofluidic diode for simple fluids without moving parts. *Physical Review Letters* **115**, 134503.

Liss M., Petersen B., Wolf H. & Prohaska E. (2002) An aptamer-based quartz crystal protein biosensor. *Analytical Chemistry* **74**, 4488–4495.

Liu G. & Zhang G. (2013) *QCM-D studies on polymer behavior at interfaces*. Springer.

Liu S., Yuzvinsky T.D. & Schmidt H. (2013) Effect of fabrication-dependent shape and composition of solid-state nanopores on single nanoparticle detection. *ACS Nano* **7**, 5621–5627.

Liu Y. & Yobas L. (2013) Label-free electrical quantification of amplified nucleic acids through nanofluidic diodes. *Biosensors and Bioelectronics* **50**, 78–83.

Löfroth G. & Augenstein L. (1967) Effect of adsorption on the radiation sensitivity of trypsin. *Archives of Biochemistry and Biophysics* **118**, 73–81.

Mafe S. & Ramirez P. (1997) Electrochemical characterization of polymer ion-exchange bipolar membranes. *Acta Polymerica* **48**, 234–50.

Majumder M., Chopra N., Andrews R. & Hinds B.J. (2005) Nanoscale hydrodynamics: enhanced flow in carbon nanotubes. *Nature* **438**, 44.

Makowski M.S. & Ivanisevic A. (2011) Molecular Analysis of Blood with Micro-/Nanoscale Field-Effect-Transistor Biosensors. *Small* **7**, 1863–1875.

Malmqvist M. (1993) Biospecific interaction analysis using biosensor technology. *Nature* **361**, 186–187.

Manafi M., Kneifel W. & Bascomb S. (1991) Fluorogenic and chromogenic substrates used in bacterial diagnostics. *Microbiological Reviews* **55**, 335–348.

Mante P.-A., Chen C.-C., Wen Y.-C., Chen H.-Y., Yang S.-C., Huang Y.-R., Chen I.-J., Chen Y.-W., Gusev V. & Chen M.-J. (2014) Probing Hydrophilic Interface of Solid/Liquid-Water by Nanoultrasonics. *Scientific Reports* **4**.

Miedema H., Vrouenraets M., Wierenga J., Meijberg W., Robillard G. & Eisenberg B. (2007) A biological porin engineered into a molecular, nanofluidic diode. *Nano Letters* **7**, 2886–2891.

Mortensen N.A. & Kristensen A. (2008) Electroviscous effects in capillary filling of nanochannels. *Applied Physics Letters* **92**, 063110.

Muratsugu M., Ohta F., Miya Y., Hosokawa T., Kurosawa S., Kamo N. & Ikeda H. (1993) Quartz crystal microbalance for the detection of microgram quantities of human serum albumin: relationship between the frequency change and the mass of protein adsorbed. *Analytical Chemistry* **65**, 2933–2937.

Napoli M., Eijkel J. & Pennathur S. (2010) Nanofluidic technology for biomolecule applications: a critical review. *Lab on a Chip* **10**, 957–985.

Neff P.A., Serr A., Wunderlich B.K. & Bausch A.R. (2007) Label-Free Electrical Determination of Trypsin Activity by a Silicon-on-Insulator Based Thin Film Resistor. *ChemPhysChem* **8**, 2133–2137.

Nelson B.P., Grimsrud T.E., Liles M.R., Goodman R.M. & Corn R.M. (2001) Surface plasmon resonance imaging measurements of DNA and RNA hybridization adsorption onto DNA microarrays. *Analytical Chemistry* **73**, 1–7.

Oh J.M., Faez T., de Beer S. & Mugele F. (2010) Capillarity-driven dynamics of water–alcohol mixtures in nanofluidic channels. *Microfluidics and Nanofluidics* **9**, 123–129.

Ohshima H. (2002) Modified Henry function for the electrophoretic mobility of a charged spherical colloidal particle covered with an ion-penetrable uncharged polymer layer. *Journal of Colloid and Interface Science* **252**, 119–125.

Orosco M.M., Pacholski C. & Sailor M.J. (2009) Real-time monitoring of enzyme activity in a mesoporous silicon double layer. *Nature Nanotechnology* **4**, 255–258.

Ortiz-Young D., Chiu H.-C., Kim S., Voïtchovsky K. & Riedo E. (2013) The interplay between apparent viscosity and wettability in nanoconfined water. *Nature Communications* **4**, 2842. doi:10.1038/ncomms3482

Park H.G. & Jung Y. (2014) Carbon nanofluidics of rapid water transport for energy applications. *Chemical Society Reviews* **43**, 565–576.

Pevarnik M., Healy K., Toimil-Molares M.E., Morrison A., Létant S.E. & Siwy Z.S. (2012) Polystyrene particles reveal pore substructure as they translocate. *ACS Nano* **6**, 7295–7302.

Pevarnik M., Schiel M., Yoshimatsu K., Vlassiouk I.V., Kwon J.S., Shea K.J. & Siwy Z.S. (2013) Particle deformation and concentration polarization in electroosmotic transport of hydrogels through pores. *ACS Nano* **7**, 3720–3728.

Phan V.-N., Yang C. & Nguyen N.-T. (2009) Analysis of capillary filling in nanochannels with electroviscous effects. *Microfluidics and Nanofluidics* **7**, 519–530.

Plawsky J., Fedorov A., Garimella S., Ma H., Maroo S., Chen L. & Nam Y. (2014) Nano- and Microstructures for Thin-Film Evaporation—A Review. *Nanoscale and Microscale Thermophysical Engineering* **18**, 251–269.

Prabhu A.S., Jubery T.Z.N., Freedman K.J., Mulero R., Dutta P. & Kim M.J. (2010) Chemically modified solid state nanopores for high throughput nanoparticle separation. *Journal of Physics: Condensed Matter* **22**, 454107.

Puente X.S., Sánchez L.M., Overall C.M. & López-Otín C. (2003) Human and mouse proteases: a comparative genomic approach. *Nature Reviews: Genetics* **4**, 544–558.

Qin X., Yuan Q., Zhao Y., Xie S. & Liu Z. (2011) Measurement of the rate of water translocation through carbon nanotubes. *Nano Letters* **11**, 2173–2177.

Qiu Y., Vlassiouk I., Hinkle P., Toimil-Molares M.E., Levine A.J. & Siwy Z.S. (2016) Role of Particle Focusing in Resistive-Pulse Technique: Direction-Dependent Velocity in Micropores. *ACS Nano* **10**, 3509–3517.

Raja M., Raja A., Imran M., Santha A. & Devasena K. (2011) Enzymes application in diagnostic prospects. *Biotechnology* **10**, 51–59.

Ralston J., Popescu M. & Sedev R. (2008) Dynamics of wetting from an experimental point of view. *Annual Review of Materials Research* **38**, 23–43.

Ransohoff T. & Radke C. (1988) Laminar flow of a wetting liquid along the corners of a predominantly gas-occupied noncircular pore. *Journal of Colloid and Interface Science* **121**, 392–401.

Raviv U., Laurat P. & Klein J. (2001) Fluidity of water confined to subnanometre films. *Nature* **413**, 51–54.

Rudzevich Y., Lin Y., Wearne A., Ordonez A., Lupan O. & Chow L. (2014) Characterization of liposomes and silica nanoparticles using resistive pulse method. *Colloids and Surfaces A: Physicochemical and Engineering Aspects* **448**, 9–15.

Saleh O. & Sohn L. (2001) Quantitative sensing of nanoscale colloids using a microchip Coulter counter. *Review of Scientific Instruments* **72**, 4449–4451.

Saleh O.A. & Sohn L.L. (2003) Direct detection of antibody–antigen binding using an on-chip artificial pore. *Proceedings of the National Academy of Sciences of the United States of America* **100**, 820–824.

Schoch R.B., Cheow L.F. & Han J. (2007) Electrical detection of fast reaction kinetics in nanochannels with an induced flow. *Nano Letters* **7**, 3895–3900.

Schoch R.B., Han J. & Renaud P. (2008) Transport phenomena in nanofluidics. *Reviews of Modern Physics* **80**, 839.

Schuck P. & Minton A.P. (1996) Analysis of mass transport-limited binding kinetics in evanescent wave biosensors. *Analytical Biochemistry* **240**, 262–272.

Sendner C., Horinek D., Bocquet L. & Netz R.R. (2009) Interfacial water at hydrophobic and hydrophilic surfaces: Slip, viscosity, and diffusion. *Langmuir* **25**, 10768–10781.

Singh K.P., Kumari K. & Kumar M. (2011) Ion current rectification in a fluidic bipolar nanochannel with smooth junction. *Applied Physics Letters* **99**, 113103.

Sinha S., Rossi M.P., Mattia D., Gogotsi Y. & Bau H.H. (2007) Induction and measurement of minute flow rates through nanopipes. *Physics of Fluids* **19**, 013603.

Siwy Z., Apel P., Baur D., Dobrev D.D., Korchev Y.E., Neumann R., Spohr R., Trautmann C. & Voss K.-O. (2003a) Preparation of synthetic nanopores with transport properties analogous to biological channels. *Surface Science* **532**, 1061–1066.

Siwy Z., Apel P., Dobrev D., Neumann R., Spohr R., Trautmann C. & Voss K. (2003b) Ion transport through asymmetric nanopores prepared by ion track etching. *Nuclear Instruments and Methods in Physics Research Section B: Beam Interactions with Materials and Atoms* **208**, 143–148.

Siwy Z., Gu Y., Spohr H., Baur D., Wolf-Reber A., Spohr R., Apel P. & Korchev Y. (2002) Rectification and voltage gating of ion currents in a nanofabricated pore. *EPL (Europhysics Letters)* **60**, 349.

Siwy Z., Heins E., Harrell C.C., Kohli P. & Martin C.R. (2004) Conical-nanotube ion-current rectifiers: the role of surface charge. *Journal of the American Chemical Society* **126**, 10850–10851.

Siwy Z.S. (2006) Ion-Current Rectification in Nanopores and Nanotubes with Broken Symmetry. *Advanced Functional Materials* **16**, 735–746.

Slouka Z., Senapati S. & Chang H.-C. (2014) Microfluidic systems with ion-selective membranes. *Annual Review of Analytical Chemistry* **7**, 317–335.

Smeets R.M., Keyser U.F., Krapf D., Wu M.-Y., Dekker N.H. & Dekker C. (2006) Salt dependence of ion transport and DNA translocation through solid-state nanopores. *Nano Letters* **6**, 89–95.

Sobolev V., Churaev N., Velarde M. & Zorin Z. (2000) Surface tension and dynamic contact angle of water in thin quartz capillaries. *Journal of Colloid and Interface Science* **222**, 51–54.

Sonin A.A. & Grossman G. (1972) Ion transport through layered ion exchange membranes. *Journal of Physical Chemistry* **76**, 3996–4006.

Sparreboom W., Van Den Berg A. & Eijkel J. (2009) Principles and applications of nanofluidic transport. *Nature Nanotechnology* **4**, 713–720.

Srividhya J. & Schnell S. (2006) Why substrate depletion has apparent first-order kinetics in enzymatic digestion. *Computational Biology and Chemistry* **30**, 209–214.

Stefanini M. (1985) Enzymes, isozymes, and enzyme variants in the diagnosis of cancer. A short review. *Cancer* **55**, 1931–1936.

Stein D., Kruithof M. & Dekker C. (2004) Surface-charge-governed ion transport in nanofluidic channels. *Physical Review Letters* **93**, 035901.

Sun G., Senapati S. & Chang H.-C. (2016) High-flux ionic diodes, ionic transistors and ionic amplifiers based on external ion concentration polarization by an ion exchange membrane: a new scalable ionic circuit platform. *Lab on a Chip* **16**, 1171–1177.

Sun L. & Crooks R.M. (2000) Single carbon nanotube membranes: a well-defined model for studying mass transport through nanoporous materials. *Journal of the American Chemical Society* **122**, 12340–12345.

Tas N., Haneveld J., Jansen H., Elwenspoek M. & Van Den Berg A. (2004) Capillary filling speed of water in nanochannels. *Applied Physics Letters* **85**, 3274–3276.

Tas N.R., Mela P., Kramer T., Berenschot J. & van den Berg A. (2003) Capillarity induced negative pressure of water plugs in nanochannels. *Nano Letters* **3**, 1537–1540.

Thamdrup L.H., Persson F., Bruus H., Kristensen A. & Flyvbjerg H. (2007) Experimental investigation of bubble formation during capillary filling of SiO 2 nanoslits. *Applied Physics Letters* **91**, 163505–163513.

Thomas J.A. & McGaughey A.J. (2008) Reassessing fast water transport through carbon nanotubes. *Nano Letters* **8**, 2788–2793.

Tischer W. & Wedekind F. (1999) Immobilized enzymes: methods and applications. In: *Biocatalysis-from discovery to application* (pp. 95–126). Springer.

Travis K.P. & Gubbins K.E. (2000) Poiseuille flow of Lennard-Jones fluids in narrow slit pores. *Journal of Chemical Physics* **112**, 1984–1994.

Tsutsui M., He Y., Yokota K., Arima A., Hongo S., Taniguchi M., Washio T. & Kawai T. (2016) Particle Trajectory-Dependent Ionic Current Blockade in Low-Aspect-Ratio Pores. *ACS Nano* **10**(1), 803–809.

Tsutsui M., Hongo S., He Y., Taniguchi M., Gemma N. & Kawai T. (2012) Single-nanoparticle detection using a low-aspect-ratio pore. *ACS Nano* **6**, 3499–3505.

van Delft K.M., Eijkel J.C., Mijatovic D., Druzhinina T.S., Rathgen H., Tas N.R., van den Berg A. & Mugele F. (2007) Micromachined Fabry-Perot interferometer with embedded nanochannels for nanoscale fluid dynamics. *Nano Letters* **7**, 345–350.

Van Honschoten J., Escalante M., Tas N. & Elwenspoek M. (2009) Formation of liquid menisci in flexible nanochannels. *Journal of Colloid and Interface Science* **329**, 133–139.

Van Honschoten J., Escalante M., Tas N., Jansen H. & Elwenspoek M. (2007) Elastocapillary filling of deformable nanochannels. *Journal of Applied Physics* **101**, 094310.

Van Noorden C.J. (2010) Imaging enzymes at work: metabolic mapping by enzyme histochemistry. *Journal of Histochemistry & Cytochemistry* **58**, 481–497.

Venta K.E., Zanjani M.B., Ye X., Danda G., Murray C.B., Lukes J.R. & Drndić M. (2014) Gold nanorod translocations and charge measurement through solid-state nanopores. *Nano Letters* **14**, 5358–5364.

Vlassiouk I., Kozel T.R. & Siwy Z.S. (2009) Biosensing with nanofluidic diodes. *Journal of the American Chemical Society* **131**, 8211–8220.

Vlassiouk I. & Siwy Z.S. (2007) Nanofluidic diode. *Nano Letters* **7**, 552–556.

Vlassiouk I., Smirnov S. & Siwy Z. (2008) Nanofluidic ionic diodes. Comparison of analytical and numerical solutions. *ACS Nano* **2**, 1589–1602.

Waley S.G. & Watson J. (1953) The action of trypsin on polylysine. *Biochemical Journal* **55**, 328.

Wang M., Chang C.-C. & Yang R.-J. (2010) Electroviscous effects in nanofluidic channels. *Journal of Chemical Physics* **132**, 024701.

Wang Y., Kececi K., Mirkin M.V., Mani V., Sardesai N. & Rusling J.F. (2013) Resistive-pulse measurements with nanopipettes: detection of Au nanoparticles and nanoparticle-bound anti-peanut IgY. *Chemical Science* **4**, 655–663.

Wanunu M., Morrison W., Rabin Y., Grosberg A.Y. & Meller A. (2010) Electrostatic focusing of unlabelled DNA into nanoscale pores using a salt gradient. *Nature Nanotechnology* **5**, 160–165.

Wei C., Bard A.J. & Feldberg S.W. (1997) Current rectification at quartz nanopipet electrodes. *Analytical Chemistry* **69**, 4627–4633.

Weislogel M.M. & Lichter S. (1998) Capillary flow in an interior corner. *Journal of Fluid Mechanics* **373**, 349–378.

Whitby M., Cagnon L., Thanou M. & Quirke N. (2008) Enhanced fluid flow through nanoscale carbon pipes. *Nano Letters* **8**, 2632–2637.

Wu H., Liu H., Tan S., Yu J., Zhao W., Wang L. & Liu Q. (2014) The Estimation of Field-Dependent Conductance Change of Nanopore by Field-Induced Charge in the Translocations of AuNPs-DNA Conjugates. *Journal of Physical Chemistry C* **118**, 26825–26835.

Yan R., Liang W., Fan R. & Yang P. (2009) Nanofluidic diodes based on nanotube heterojunctions. *Nano Letters* **9**, 3820–3825.

Yeh L.-H., Zhang M., Joo S.W., Qian S. & Hsu J.-P. (2012) Controlling pH-regulated bionanoparticles translocation through nanopores with polyelectrolyte brushes. *Analytical Chemistry* **84**, 9615–96122.

Yoon H., Ko S. & Jang J. (2008) Field-effect-transistor sensor based on enzyme-functionalized polypyrrole nanotubes for glucose detection. *Journal of Physical Chemistry B* **112**, 9992–9997.

Yossifon G., Chang Y.-C. & Chang H.-C. (2009a) Rectification, gating voltage, and interchannel communication of nanoslot arrays due to asymmetric entrance space charge polarization. *Physical Review Letters* **103**, 154502.

Yossifon G., Mushenheim P., Chang Y.-C. & Chang H.-C. (2009b) Nonlinear current-voltage characteristics of nanochannels. *Physical Review E* **79**, 046305.

Zhang B., Wood M. & Lee H. (2009) A silica nanochannel and its applications in sensing and molecular transport. *Analytical Chemistry* **81**, 5541–5548.

Zhang Y., Clausmeyer J., Babakinejad B., López Córdoba A., Ali T., Shevchuk A., Takahashi Y., Novak P., Edwards C. & Lab M. (2016) Spearhead Nanometric Field-Effect Transistor Sensors for Single-Cell Analysis. *ACS Nano* **10**(3), 3124–3121.

CURRICULUM VITAE

Mohammad Amin Alibakhshi

Department of Mechanical Engineering, Boston University

110 Cummington Mall, Boston, MA 02215. *E-mail*: amin@bu.edu

EDUCATION

2009–2016

Ph.D. in Mechanical Engineering, Boston University, Boston, MA. Thesis title: *Characterization of Molecule and Particle Transport through Nanoscale Conduits.*

2006–2009

M.Sc. in Mechanical Engineering, Iran University of Science and Technology (IUST), Tehran, Iran. Thesis title: *Noise Prediction of a Subsonic Jet Using Acoustic Analogy*.

2001–2006

B.Sc. in Mechanical Engineering, Iran University of Science and Technology (IUST), Tehran, Iran. Thesis title: *Multi-scattering and Dissipation Effects in Acoustic Diffraction from cylindrical Obstacles*.

HONORABLE MENTIONS

Member of *Iranian Elites Association*, 2009.

Distinguished Masters student at IUST with GPA 18.76/20, 2009.

Distinguished Undergraduate student at IUST due to prolific publication, 2006.

Ranked among top 0.1% attendees in the nationwide college entrance exam, Iran, 2001.

Admitted in *National Organization for Development of Exceptional Talents*, Iran, 1997.

RESEARCH and TEACHING EXPERIENCE

Research Assistant, Boston University, Nanoscale Energy-Fluids Transport Laboratory, Jan 2012 – present.

Research Assistant, Boston University, Nonlinear and Biomedical Acoustic Laboratory, Jan 2010 – Jan 2012.

Teaching Assistant, Boston University, Fall 2009.

Research Assistant, Iran University of Science and Technology, CFD laboratory and CAE center, September 2006 – March 2009.

Research Assistant, Iran University of Science and Technology, Acoustic Research Laboratory, July 2002 – September 2005.

RESEARCH AREAS

Nanofluidics

Nanopore sensing

Development of tools and techniques for Biodetection

Biomedical Ultrasonics and Shockwave Lithotripsy

Sound waves propagation, Scattering of sound, Aeroacoustics

PUBLICATIONS

JOURNAL ARTICLES

[1] Mohammad A. Alibakhshi and C. Duan; **Translocation of Nanobeads through Low Aspect Ratio Nanopores**. Under Prep.

[2] Y. Li, Mohammad A. Alibakhshi, and C. Duan; **Kinetic Limited Water Evaporation in Hydrophilic Nanofluidic Channels**. Under Prep.

[3] Mohammad A. Alibakhshi, B. Liu, and C. Duan; **Geometrical Control of Ionic Current Rectification in a Configurable Nanofluidic Diode**. Under Review.

[4] Mohammad A. Alibakhshi, and C. Duan; **Enzymatic Hydrolysis of Polypeptides in a Nanofluidic Channel**. Under Review.

[5] C. Duan, Mohammad A. Alibakhshi, D-K Kim, C.M. Brown, C.S. Craik, and A. Majumdar; **Label-Fee Electrical Detection of Enzymatic Reactions in Nanochannels**. ACS Nano, DOI: 10.1021/acsnano.6b02062.

[6] Mohammad A. Alibakhshi, Q. Xie, Y. Li, and C. Duan; **Accurate Measurement of Liquid Transport through Nanoscale Conduits**. Scientific Reports, 6, 24936; DOI: 10.1038/srep24936 (2016).

[7] Mohammad A. Alibakhshi, J.M. Kracht, R.O. Cleveland, E. Filoux and J.A. Ketterling; **Single-shot Measurements of the Acoustic Field of an Electrohydraulic Lithotripter Using a Hydrophone Array**. *The Journal of Acoustical Society of America*, 133(5), May 2013.

[8] M. Azarpeyvand, Mohammad A. Alibakhshi, and R. Self; **Effects of Multi-Scattering on the Performance of a Single-Beam Acoustic Manipulation Device**. *IEEE Transactions on Ultrasonics, Ferroelectrics, and Frequency Control*, 59(8), August 2012.

[9] Mohammad A. Alibakhshi and R.G. Holt; **Suppressing shape instabilities to discover the Bjerknes force instability.** *The Journal of Acoustical Society of America,* 130 (5), Pt. 2, November 2011.

[10] S.A. Badsar and Mohammad A. Alibakhshi; **Dynamic response of an underground tunnel to seismic waves**. *Journal of Seismic Explorations*, 18(2), April 2009.

[11] S.M. Hasheminejad and Mohammad A. Alibakhshi; **Eccentricity and thermoviscous effects on ultrasonic scattering from a two-fluids liquid bridge**. *Journal of Zhejiang University Science*, 9(1), 65–78, 2008.

[12] S.M. Hasheminejad and Mohammad A. Alibakhshi; **Diffraction of sound by a poroelastic cylindrical absorber near an impedance plane**. *International Journal of Mechanical Sciences*, 49, 1–12, 2007.

[13] S.M. Hasheminejad and Mohammad A. Alibakhshi; **Dynamic viscoelastic and multiple scattering effects in fiber suspensions**. *Journal of Dispersion Science and Technology*, 27, 219–234, 2006.

[14] S.M. Hasheminejad and Mohammad A. Alibakhshi; **Two-dimensional scattering from an impenetrable cylindrical obstacle in an acoustic quarterspace**. *Forsch Ingenieurwes*, 70, 179–186, 2006.

[15] S.M. Hasheminejad and Mohammad A. Alibakhshi; **Ultrasonic scattering from compressible cylinders including multiple scattering and thermoviscous effects**. *Archives of Acoustics*, 31(2), 1–21, 2006.

CONFERENCE PRESENTATIONS

[16] Mohammad A. Alibakhshi, Q. Xie, Y. Li, and C. Duan; **Experimental Study of Water Transport through Hydrophilic Nanochannels**. *68th Annual Meeting of the APS Division of Fluid Dynamics*, Boston, MA, 22–24 November 2015.

[17] Y. Li, Mohammad A. Alibakhshi, Q. Xie, and C. Duan*; **Kinetic Limited Water Evaporation in Hydrophilic Nanofluidic Channels***. *68th Annual Meeting of the APS Division of Fluid Dynamics*, Boston, MA, 22–24 November 2015.

[18] J.A. Ketterling, E. Filoux, Mohammad A. Alibakhshi, J. M. Kracht and R. O. Cleveland; **Instantaneous Beamwidth Measurements of an Electrohydraulic Lithotripter**. *IEEE Conference,* Bari, Italy, 4–7 July 2010.

[19] S.M. Hosseinalipour, Mohammad A. Alibakhshi, M. Azarpeyvand; **Noise Prediction of an Isothermal Subsonic Jet Using Different Acoustic Time-scales**. *The 7th Iranian Aerospace Society Conference*, Feb. 2008, Sharif University of Technology, Tehran, Iran.

[20] S.M. Hosseinalipour, Mohammad A. Alibakhshi, M. Azarpeyvand; *On the Role of Flow-Acoustic Interaction in Noise Directivity of a Subsonic Isothermal Jet*. *11th Fluid Dynamics Conference*, May 2008, K. N. Toosi University of Technology, Tehran, Iran.

[21] S.M. Hosseini maab, M. Maleki, Mohammad A. Alibakhshi, S.M. Hasheminejad; **Scattering and Active Control of Sound Waves from a Submerged Spherical Steel**

Shell. *16th Annual (International) Conference on Mechanical Engineering*, May 2008, Kerman, Iran.

[22] S.M. Taghavi, M. Shams, A. Amoli, A. Rastgoo and Mohammad A. Alibakhshi; *Effect of Blade Angle on Performance of Axial Turbo-Molecular Pump*. *14th Annual (International) Conference on Mechanical Engineering*, May 2006, Isfahan University of Technology, Isfahan, Iran.

[23] S.M. Hasheminejad and Mohammad A. Alibakhshi; **Acoustic scattering by cylindrical obstacles submerged in ideal fluids**. *8th Fluid Dynamics conference*, September 2003, Tabriz University, Tabriz, Iran.

POSTER PRESENTATIONS

[24] Mohammad A. Alibakhshi and C. Duan; **Modeling Enzymatic Reactions in a Nanofluidic Channel**. *ASME IMECE Micro and Nano Technology Forum*, Houston, Texas, 9–15 November 2012.

[25] Mohammad A. Alibakhshi, J. M. Kracht, J. A. Ketterling, and R. O. Cleveland; **Characterization of the acoustic field of an electrohydraulic lithotripter using a linear hydrophone array,** March 30th 2010, Boston University Science Day.